Grid Inertial Response with Lithium-ion Battery Energy Storage Systems

Master's Thesis

Václav Knap and Rakesh Sinha
Department of Energy Technology
Aalborg University, Denmark

AD NYE VEJE
AALBORG UNIVERSITET

AALBORG UNIVERSITY
DENMARK
STUDENT REPORT

Title:	Grid Inertial Response with Lithium-ion Battery Energy Storage Systems
Semester:	10^{th}
Semester theme:	Master's Thesis
Project period:	1/2– 4/6, 2013
ECTS:	30
Supervisor:	Maciej Swierczynski Daniel Stroe Sanjay Chaudhary
External supervisor:	Philip C. Kjær
Project group:	EPSH4 - 1031

SYNOPSIS:

This report represents the Master's Thesis on project, **"Grid Inertial Response with Lithium-ion Battery Energy Storage Systems"**. Identification of the issue concerning grid inertia has been discussed along with the proposed solution of using the energy storage system (ESS). Model of the battery energy storage system has been developed on MATLAB/Simulink and the wind turbine generator with full scale converter along with converter for the ESS has been developed in RSCAD. The 12-bus grid model has been implemented to investigate the dynamics of inertial response for different wind power penetration levels. RTDS and dSPACE have been used for real time simulation of power system and ESS, respectivelly. Different approaches of providing inertial response, with ESSs, based on derivative control and combination of derivative - droop control have been investigated. Moreover, the effect of the ESS size on the inertial response has been analyzed. The consequence of variable nature of wind power towards system frequency has also been simulated. The results of the simulations have been present through various study cases.

Václav Knap

Rakesh Sinha

Copies:	7
Last page:	76
Last appendix:	C

By signing this document, each member of the group confirms that all group members have participated in the project work, and thereby all members are collectively liable for the contents of the report. Furthermore, all group members confirm that the report does not include plagiarism.

Preface

This project was carried out by Rakesh Sinha and Václav Knap. Both authors are degree students in the 10th semester at Department of Energy Technology, Aalborg University, Denmark.

Since the authors have never worked on RTDS and dSPACE previously, it has been a challenge to learn and perform simulation in the short time interval between February to May 2013. In the end, authors got a very nice experience in working with RTDS, dSPACE and interfacing them together.

The report has been written $\LaTeX\,2_{\varepsilon}$. This report uses SI base units and derived units written as [unit]. Frequently used constants and abbreviations are described in the reports.

We would like to thank our supervisors for the continuous support and help in guiding this project.

Acknowledgements

First of all we would like to express our heartfelt gratitude to our project supervisors; Maciej Swierczynski, Daniel Stroe and Sanjay Chaudhary for providing valuable guidance and support to accomplish the project goal. We would like to also thank to our external supervisor, Philip C. Kjær from Vestas.

This thesis is a part of Vestas A/S scholarship program. Authors would acknowledge Vestas Wind Systems A/S and Aalborg University for supporting this thesis.

Summary

Variable speed wind turbines (VSWT) are widely used to generate electrical power in large scale. They are equipped with back to back power electronic converter when connected to the grid which creates an electrical decoupling between the generator and the grid. Hence, the variation in grid frequency is not seen by the generator and they cannot support the grid inertia by default. The high grid penetration levels of wind farms based on VSWT, which are slowly repacing the conventional power plants based on large synchronous generators, leads to a reduction of the total inertia of the system. As a consequence, large rate of change of frequency(ROCOF) can be observed during sudden large disturbances in the system. Therefore, there is a strong motivation for improving the way in which the power system with low inertia could cope up with the system frequency support.

Energy storage systems (ESSs) can contribute with inertial response to power system with low inertia. RSCAD and dSPACE battery simulator have been used to perform real time simulations. It includes the 12-bus grid model, voltage source converter (VSC) model representing wind power plants and the ESS model. Various study cases are performed and their results are evaluated. Through basic study case simulation, fundamental effects of different level of wind penetration towards the system inertia have been observed. The other study cases are conducted to investigate the effect of the ESS in inertial response along with the settings of derivative control parameters, sizing, combine effect of derivative and droop control, and the longer term ESS operation.

It has been observed that, increasing the size of converter based wind turbines reduces the total grid inertia. This increases the ROCOF as well as larger drop in the grid frequency during large disturbance. Introducing ESS with derivative control improves the inertial response. The size of ESS, parameters of the derivative control such as response time and gain shows significant effect in improving the grid inertia. The controller based on combination of derivative and droop control has advantages over pure derivative or droop control towards ROCOF and minimum frequency drop. Finally, there is a need of further investigation and identification for the use of derivative - droop control in the ESS to improve inertial response as well as support the primary frequency regulation.

Table of contents

1 Introduction

1.1 Background

With a consideration of the future by economic and ecological aspects, there is progress towards the sustainability. This is strongly projected in to the area of energy sources. Evaluating the composition of the energy production by sources, in terms of million tons of oil equivalent (Mtoe) as shown in Fig. 1.1, for the years period from 1971 to 2009, it is visible that the main part of consumption is covered with fossil fuels. Their depletion in the future will become the real threat for the energy independence. Additionally, the fossil fuels are considered as environment unfriendly with CO_2 emissions and further by their impact to the ecosystem.

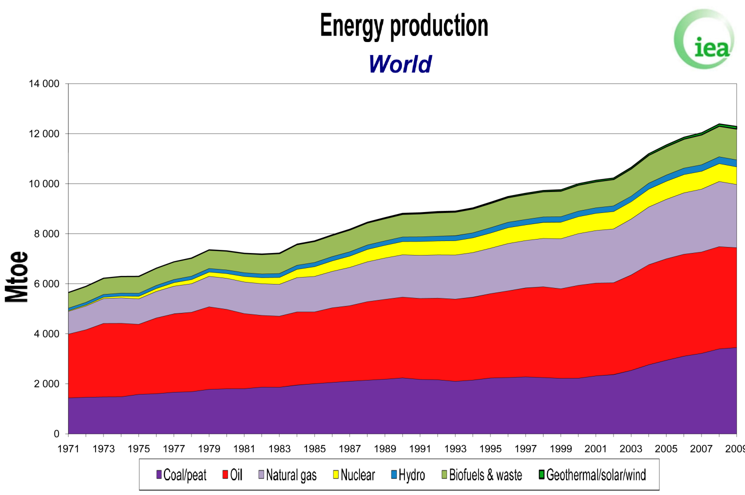

Figure 1.1: Electricity generation by fuel [1].

The investigation of the energy situation in Europe revealed heavy dependency on the import, around 50 % in 2005. Before change of the policy it was estimated to increase close to 70 % in 20 years. This trend together with a combination of the growing prices for the fossil fuels would result into significant higher cost of electricity production in Europe. Therefore, the economic growth needs to secure stable climate of the long-term predictable cost of energy supply. Hence the development of renewable energy sources (RES) seems to be the perspective way, not only for the economic reasons, but moreover for environmental, political and social aspects [2]. Therefore, European Union proclaimed the goal to reach overall share of RES in the energy production of 20 % and over 10 % in transport by 2020 [3]. Some specific countries proceed even more in this context and as the pioneer in the renewable energy field, Denmark is the one. The goal of the Danish policy is to reach more than 35 % of renewable energy in the final energy consumption and approximately 50 % of the electricity consumption should be supplied by wind power. The situation from 2010 and expected in 2020 is shown in Fig. 1.2. This stands only as a milestone for the full exchange to renewable energy in 2050 [4].

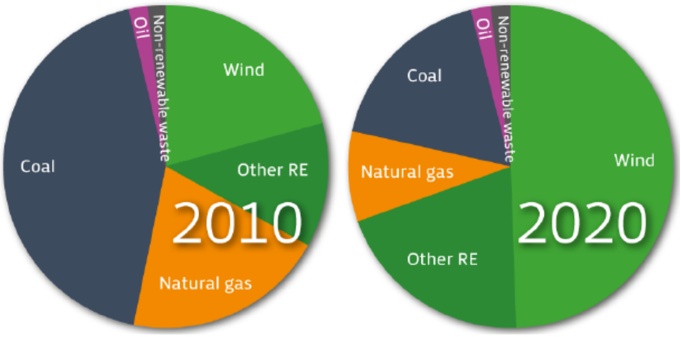

Figure 1.2: Electricity consumption with respect to source of energy [4].

Nowadays, energy production in modern power systems is based mainly on multiple parallel synchronous generators in conventional power plants. The initial energy source (fossil, nuclear and hydro) is transformed by prime mover to mechanical energy. Consequently, it is converted to electrical energy by synchronous generators. These generators are usually connected through transformers directly to the transmission systems [5].

By brief review and comparison of conventional and renewable power plants, elementary differences have been identified. First of all, the fuel for conventional power plants is considered as available at all time and thereby the power output is fully controllable in operating range. The availability of renewable energy sources as wind or sunshine can be only predicted with a certain probability and power output regulation is dependent on the available amount. Secondly, they are different in configuration topology. Fig. 1.3 shows the overview of a conventional, wind and photovoltaic power plant. In the case of conventional power plant, there is a direct coupling between the grid and generator. This provides connection between electrical frequency of the grid and speed of the generator rotor. The rotating mass of the rotor acts as kinetic energy storage and provides inertial response. This is an important attribute, when there is sudden inequality between supply and demand in the grid. The modern wind power plants usually use small scale or full scale power converters that provide partial or full decoupling between the generator and the grid. This prevents to use a rotating mass of generator as energy storage directly and by that there is lack of inertia phenomenon. In the photovoltaic case, there is lack of any rotating part and power electronic converter is always in use, therefore without any extensive modification, the intertial response does not exist [6], [7].

1.2 Motivation

Wind parks are usually equipped with frequency relay which disconnects the generating plants during frequency deviation more than the permissible operating limit. Disconnection of large wind farms not only leads to loss of generation but also leads to power system oscillation [8].

Variable speed wind turbines are widely used to generate electrical power in large scale. This is primarily due to its many advantages in comparison to other generators, where the source of mechanical power transferred to the generator varies rapidly (e.g. wind). Variable speed wind turbines are equipped with back to back power electronic converter when connected to the grid. The DC link capacitor (DC voltage bus) in back-back converter creates an electrical

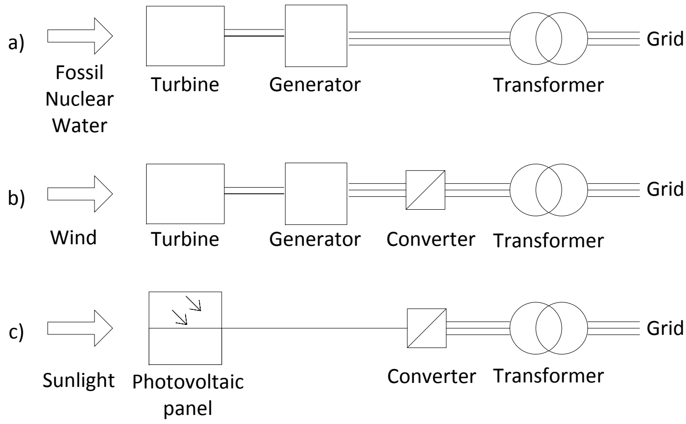

Figure 1.3: The configuration overview of power plant systems: a) Conventional, b) Wind, c) Photovoltaic.

decoupling between the generator and the grid. Because of this, the generator output voltage and frequency is maintained constant even during the fluctuation in the rotor speed due to wind. At the same time variation in grid frequency are also not seen by the generator. Hence, the generator cannot support the grid inertia by default.

Further, the large amount of penetration of wind turbines is replacing the synchronous generators and apparently leads to the reduction of total inertia of the system. As a consequence, large rate of change in frequency will be observed during sudden large disturbances in the system [9] (either due to fault, sudden collapse of large generator or connection / disconnection of large load in the system). Therefore, the motivation for improving the way in which the power system with low inertia could cope up with the system frequency support strongly arises.

Energy storage systems (ESSs) can contribute with inertial response to power system with low inertia. Moreover, ESSs are considered as the perspective elements of the modern power system for integration of RES. They can as well participate at improving power quality and reliability. The ESS can store electric energy for later usage as well.

1.3 Problem description

Today's trends regarding power generation are moving towards renewable energy sources (mostly wind and photovoltaic). However, the grid integration of these renewable energy sources is not a straightforward task and it raises new challenges regarding the power system stability, reliability and power quality. This is especially the case of grids with high wind power penetrations, where maintaining the system inertia becomes an important issue for system operators.

Traditionally, the grid inertia is provided by conventional power plants consisting of large synchronous generators. The replacement of conventional power plants with renewable energy sources such as wind turbines with power electronic converters reduces overall inertia of the grid. Thus, alternative solutions for providing inertial response is necessary.

Energy storage systems (ESSs) based on Lithium-ion (Li-ion) batteries could represent attractive candidates to provide inertial response, because of their operational characteristics in terms of power, energy and durability. Nevertheless, at present, Li-ion batteries are still not a cheap solution; therefore, a proper investigation of the viability of providing this grid support service with Lithium-ion batteries has to be investigated.

1.3.1 Objectives

The main goal of this project is to investigate the feasibility of integrating the ESS based on Lithium-ion batteries for providing inertial response into the grid.

The specific tasks carried out to achieve the objective are:

- Literature review on:
  - Rotating machine inertia
  - Wind turbine inertia
  - Grid frequency response to disturbance
  - Li-ion batteries as an energy storage system and its characteristics
- Creating a real time simulation model of the grid (12-bus grid model), with various levels of wind penetration and interface it with a realistic Li-ion battery model on dSPACE Simulator
- Evaluation of using the ESS based on Li-ion batteries for providing inertial response

1.3.2 Methodology

The first step is to prepare environment for simulations. The 12-bus system, wind power plants and the ESS converter are modeled in RSCAD, which provides prepared enviroment for modeling of grid elements and their real time simulations in RTDS with connection of external hardware. Further it includes modeling of the ESS based on realistic Li-ion battery model and its control in MATLAB/Simulink using the dSPACE Automotive Simulation Models. After modeling, RTDS and dSPACE are connected together to provide the final simulation setup.

In the second step, study cases are performed and their results are evaluated. The basic study case represents a fundamental part for further studies since it is describing the wind penetration effect on the grid inertia, when additional ESSs are not used. The other four case studies, considering the ESSs to provide the inertial response, are performed to investigate the settings of derivative control parameters, sizing of the ESS, effect of derivative and droop control combination and the longer term ESS operation.

Based on the analysed results, the feasibility and its aspects, of intergration ESSs into the grid for providing inertial response are discussed.

1.3.3 Limitations

In order to achieve the goal of this project, several assumptions and limitations taken into account are listed below:

- the observed time frame of the simulation results are limited to 30 s
- the ability of the primary frequency regulation is based on the standard settings of the 12-bus grid model as presented in [10]
- the secondary frequency regulation is not considered
- the effect of the reactive power, damping power oscillations, voltage control, load shedding and faults in the grid (except the introduced event) are out of the project scope

- WPP is modeled as an aggregated wind turbine generator with full scale converter
- the power production from wind turbine is set as constant for the base study case and study cases 1 to 3
- the losses of the converter are not considered
- the ESS is modeled in simplified way as a single line of battery cells based on dSPACE Automotive Simulation Models
- only the $LiFePO_4$ chemistry of Li-ion batteries has been used for the ESS modeling and experiments
- thermal processes and ageing of batteries are neglected
- the economic aspects of the ESS are out of the project scope

1.3.4 Organisation of report

Chapter 1 of this report includes background and motivation along with the problem description, methodology and limitations. A brief description of energy production trends and increment of renewable energy sources are presented. The overview of the configuration of the energy sources integrated into the power system has been mentioned. Identification of the issue concerning grid inertia has been discussed along with the proposed solution of using the ESS.

In Chapter 2, the general overview of the inertial response of rotating machines have been presented. Different stages of the grid frequency response has been briefly described. An overview of the different technologies involved in grid connected wind turbines and their contribution to inertial response during grid disturbances has been presented. It is than followed by the basic battery terminology, brief comparison of the ESS technologies with detailed description of Li-ion batteries and their dynamic.

In Chapter 3, RTDS and dSPACE modeling of wind turbine generator with full scale converter and battery energy storage system respectively has been described. The use of 12-bus system to investigate the dynamics of different levels of wind power penetrations has been briefly presented. Interfacing of the RTDS and dSPACE hardware to create the simulation environment for the study purpose has been explained.

In Chapter 4, the results of different study cases have been analysed and discussed. In the base study case, the effect of increasing wind power penetration levels on the inertial response has been conducted. It is than followed by three study case that investigates the influence of the ESS settings and parameters (derivative control parameters, size of the ESS and effect of combination derivative and droop control) on the inertial response of the system. The consequences of variations in wind power towards system frequency with and without the ESS has been studied in study case 4.

Conclusion and future work have been presented in Chapter 5.

In Chapter 6, bibliography is listed.

Basic terms and abbreviations of batteries are described in Appendix A. In Appendix B the design parameters of voltage source converter, 12-bus systems and extracted data from electrochemical impedance spectroscopy fitting are included. The details of the specific study case scenario results are presented in Appendix C.

2 Literature review

2.1 Rotating machine inertia

Frequency control is very important in the power system network for maintaining the power balance as well as synchronous operation of generators connected [11]. The kinetic energy stored in the rotor of the synchronous machine during synchronous speed is given by the equation 2.1

$$K.E = \frac{1}{2} J \omega_s^2 \times 10^{-6} \qquad [MJ] \tag{2.1}$$

Where,

J = Rotor moment of intertia in [kgm^2]
ω_s = Synchronous speed in mechanical [radian/s]

Assuming windage, friction and iron loss negligible [12], the differential equation for the rotor dynamics is given by equation 2.2

$$J \frac{d^2\theta_m}{dt^2} = T_m - T_e = T_a \qquad [Nm] \tag{2.2}$$

Where,

θ_m = Angular position of rotor in stationary reference frame measured in [rad]
T_m = Mechanical torque supplied by the prime mover in [Nm] (+ve for generating mode)
T_e = Electromagnetic torque output in [Nm] (+ve for generating mode)
T_a = Accelerating torque

Hence, neglecting losses, the difference between the electrical and mechanical torque produces net accelerating torque (T_a). Multiplying both sides of equation 2.2 with ω_m, the differential equation governing the dynamics of rotating machine as per equation 2.2 can be written as equation 2.3

$$J \omega_m \frac{d\omega_m}{dt} \times 10^{-6} = P_m - P_e \qquad [MW] \tag{2.3}$$

Where,

ω_m = Mechanical rotational speed [rad]
P_m = Mechanical Power input in [MW] (+ve for generating mode)
P_e = Electrical power output in [MW] (+ve for generating mode)

For a rotating machine, all the rotating masses attached to the shaft is quantified by the inertia time constant H_{gen} as shown in equation 2.5 [13]. H_{gen} is the measure of time in seconds [s] that it takes to accelerate from zero to its rated speed using full rated power and without any load connected. In other way it is also defined as the time that a generator can provide nominal power by only using the energy that stored in its rotating mass [14].

$$H_{gen} = \frac{W_k}{S_{gen}} \qquad [s] \tag{2.4}$$

$$H_{gen} = \frac{J\omega_s^2}{2S_{gen}} \times 10^{-6} \qquad [s] \tag{2.5}$$

Where,

W_k = Kinetic energy stored in the rotating mass [MJ]
H_{gen} = Inertia constant measured in seconds [s]
S_{gen} = Nominal apparent power of machine measured in [MVA]
ω_s = Synchronous speed of the generator [rad]

from equation 2.5 and equation 2.3 we get equation 2.8

$$2H_{gen}\frac{\omega_m}{\omega_s}\frac{d(\omega_m/\omega_s)}{dt} = \frac{P_m - P_e}{S_{gen}} \qquad [MW] \tag{2.6}$$

$$\frac{2H_{gen}S_{gen}}{S_{sys}}\overline{\omega}\frac{d\overline{\omega}}{dt} = \frac{P_m - P_e}{S_{sys}} \tag{2.7}$$

$$2H_{sys}\overline{\omega}\frac{d\overline{\omega}}{dt} = \overline{P_m} - \overline{P_e} \qquad [pu] \tag{2.8}$$

Where,

S_{sys} = Base power of the system [MVA]
H_{sys} = Inertia constant of the system [s]

Equation 2.8 shows that, the difference between the supply and demand power will result in the change in the rotational speed of generator and hence change in the grid frequency. If there are more than one machine in a common base system, and if the machine swing coherently (in phase with one another) the equation 2.8 can be written as equation 2.10.

$$2\sum_{n=1}^{n} H_n\overline{\omega}\frac{d\overline{\omega}}{dt} = \sum_{n=1}^{n}\overline{P_{mn}} - \sum_{n=1}^{n}\overline{P_{en}} \tag{2.9}$$

$$2H_{eq}\overline{\omega}\frac{d\overline{\omega}}{dt} = \overline{P_{m_{eq}}} - \overline{P_{e_{eq}}} \tag{2.10}$$

Thus the coherent machines are reduced to a single machine equation as shown in equation 2.10. The amount of energy released ($\triangle\overline{E_i}$) by the mass of a single i^{th} generator for a particular frequency deviation ($\triangle\overline{f}$) can be found by integrating the equation 2.8.

$$\triangle\overline{E_i} = \int_0^t (\overline{P_{m_i}} - \overline{P_{e_i}})\,dt = \int_0^t \triangle\overline{P_i}\,dt \qquad [pu] \tag{2.11}$$

$$\Rightarrow \triangle\overline{E_i} = 2H_i\int_{\overline{f_o}}^{\overline{f_t}} \overline{f}\,d\overline{f} \qquad [pu] \tag{2.12}$$

$$\Rightarrow \triangle\overline{E_i} = 2H_i \triangle\overline{f f_o} + H_i \triangle\overline{f^2} \qquad [pu] \tag{2.13}$$

Where,

$\triangle\overline{f}$ = ($\overline{f_t}$ - $\overline{f_o}$) is the change in frequency [pu]

The base frequency $\overline{f_o}$ is equal to 1 pu and since ($\triangle\overline{f}$) is very small, $\triangle\overline{f^2} \approx 0$. Therefore equation 2.13 can be written as

$$\triangle\overline{E_i} = 2H_i \triangle\overline{f} \qquad [pu] \tag{2.14}$$

2.2 Grid frequency response to disturbance

One of the important parameters in the power system operation is the frequency. It is necessary to keep the system frequency within the allowable range to maintain the power system quality. For the system using conventional synchronous machine, response of the grid frequency to the large disturbance undergoes several stages depending upon the duration of the dynamics involved. These stages are divided into different parts [15]

1. Inertial response: provided by the inertia of rotating machine
2. Primary frequency response: governed by the generator governors
3. Secondary frequency response: controlled by automatic generator control (AGC) or manual
4. Tertiary frequency response: controlled manually

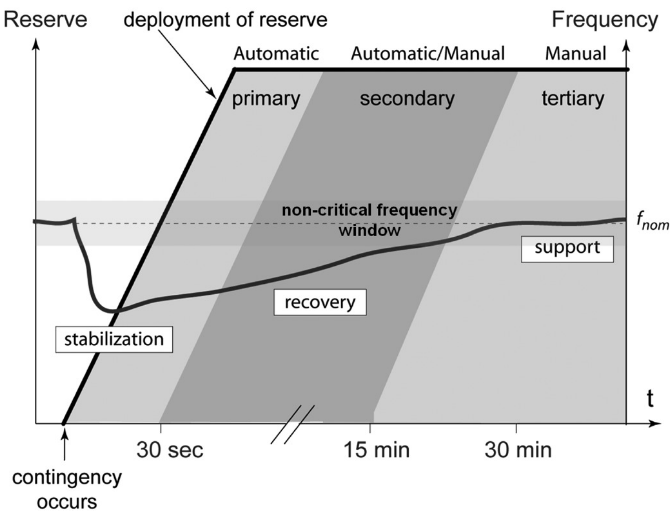

Figure 2.1: Modes of operation of frequency control by Union for the Co-ordination of Transmission of Electricity (UCTE) in central Europe [16].

Fig. 2.1 shows the different modes of operation of frequency control followed by the members of Union for the Co-ordination of Transmission of Electricity (UCTE) in central Europe [16]. Sudden disturbance in the grid regarding power imbalance due to disconnection of large load or large power plants, results in large changes of power flow in the grid. The rotor angle of the synchronous generator cannot change instantaneously due to inertia. Thus the kinetic energy stored in the machine is not released immediately at the moment of disturbance [17]. Hence, at this instant of disturbance, the energy is released from the magnetic field of synchronous generator [17]. This phenomenon lasts for approximately 1/3 of seconds, depending upon the point of disturbance, and is known as “electromagnetic stage” [18]. This frequency event is then immediately followed by “inertial response stage”.

2.2.1 Inertial response stage

The inertial response immediately follows the frequency event after electromagnetic stage. During this stage, the kinetic energy stored in the rotating part of the generator is released [18]. As the stored kinetic energy starts to decrease, the difference between the mechanical power input and electrical power output starts to increase gradually. This change in the active power output primarily depends upon the power system inertia (the total inertia present in the grid) and the rate of change of speed as represented in the equation 2.8. This will result in the decrement of the system frequency, which implies that the system with higher rotating inertia undergoes slower ROCOF (rate of change of frequency) during disturbance. This is the reason for requirement of large inertial effect for the grid frequency stability which will allow sufficient time for the primary frequency controller to act. The load imbalance are shared by all the generators connected to the system instantaneously as represented by equation 2.9. However, machine which are close to the point of impact has to share the greatest part, independent of their inertial size [17].

2.2.2 Primary frequency response

The deviation in the frequency of the power system beyond the dead band (DB), as shown in Fig. 2.2, will cause primary controllers of all generators connected to the system to respond within time frame of 20-30 seconds to stop frequency drop/rise [15]. This is achieved by the quick response of the frequency control feedback circuit to the load fluctuation present in the generating unit that supplies the needed power to maintain power balance [19]. Frequency responsive reserves (also known as regulating reserve) are maintained in the power system generation in order to handle this situation [18]. The governor action helps to generate the deficit in power [20]. The frequency oscillation due to transient disturbance is brought to steady state level (f_{ss}) by the primary frequency controller. However the re-established frequency is usually different from the reference value(f_o) [19] with the steady state error ($\triangle f_{ss}$= f_o - f_{ss}). This is due to the reason that primary frequency control is achieved using droop control, which means they reduce fluctuation but are not able to restore to the original value [21]. To overcome this issue, a secondary frequency response is necessary. Fig. 2.2 shows the ideal steady state characteristic of the governor with speed droop control.

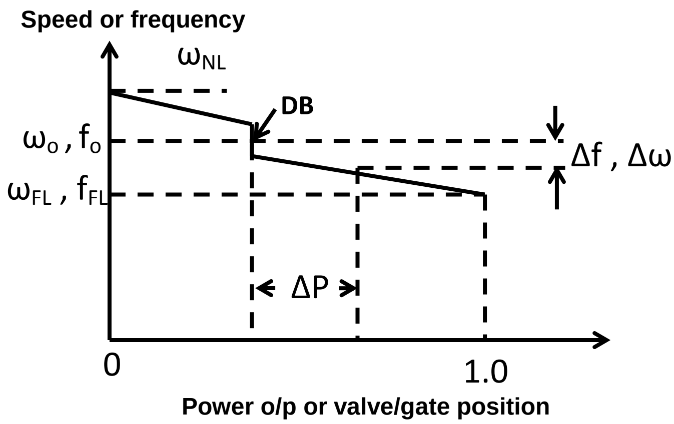

Figure 2.2: Typical steady-state characteristics of a governor with speed droop.

Where,
ω_{NL} = Steady state speed at no load
ω_{FL} = Steady state speed at full load
ω_o = Nominal or rated speed

The ratio of frequency deviation to the output power change is equal to the droop, i.e. ($\frac{\Delta f}{\Delta P} = R$).

2.2.3 Secondary frequency response

In order to reduce the steady state error ($\triangle f_{ss}$) achieved during the primary frequency control, Secondary frequency response is activated. It is also termed as automatic generation control (AGC). Secondary frequency response is provided by the contingency reserve (also known as replacement reserve) [18] and is a centrally coordinated action. In the secondary control, the generators speed droop set-point is varied according to need by the operator (by varying prime movers load reference which is used for compensating load changes [17] manually) or by using the AGC [20]. The secondary frequency response is slower than the primary frequency response, hence the frequency is restored to the reference value within 30 seconds to 30 minutes [16] as shown in Fig. 2.1. The main limitation of the secondary frequency response is the ability of prime movers to change the power production

2.2.4 Tertiary frequency response

It is responsible for balancing load generation, sales and purchase within each balancing interval which varies from 15-30 minutes depending upon the country regulation.

2.2.5 Virtual inertia

Virtual inertia is the concept of mimicking inertia where the grid is decoupled from the generator system [22]. It can be achieved with the use of additional control for power electronic interface connected system or use of energy storage system. This concept is based on the control strategy to maintain inertial behavior of power system to behave as a conventional synchronous generator. Only the behavior of prime mover is emulated to support frequency control [23].

2.3 Wind turbines and inertia

In case of wind turbine system, there are considerable amount of kinetic energy available in the rotating mass (turbine blade and shaft of the generator) [14]. However, in VSC converter based stations, the electrical system is decoupled from the mechanical system and doesn't contribute inertia to the connected system. Such power source system which doesn't contribute to the grid inertia can be defined as $\frac{dP}{d\delta}$ = 0 [13]. This means that the generator cannot support the grid transient and disturbance. In case of a strong grid where the majority of the power is generated by the large synchronous machine such as in hydro, thermal or diesel, the kinetic energy present in the rotating mass can support the system transient during disturbance. This plays major role in establishing the stability of the system during transients. However, at certain point, when the increment of renewable energy sources are replacing the conventional synchronous generators, there is threat in reduction of the system inertia.

2.3.0.1 Topologies of WTG

There are many different technologies in practice to convert available energy in wind to electrical energy that can be supplied to grid. With respect to grid connection of wind turbines, they are basically categorised into two categories: *Fixed speed* and *Variable Speed*. The four different types of wind turbine topologies are shown in Fig. 2.3.

- Type I: Induction generator-fixed speed
- Type II: Wound-rotor induction generator with adjustable external rotor resistance-variable slip
- Type III: Double-fed induction generators (DFIG)-variable speed
- Type IV: Full converter system with permanent magnet synchronous generator-variable speed, direct drive

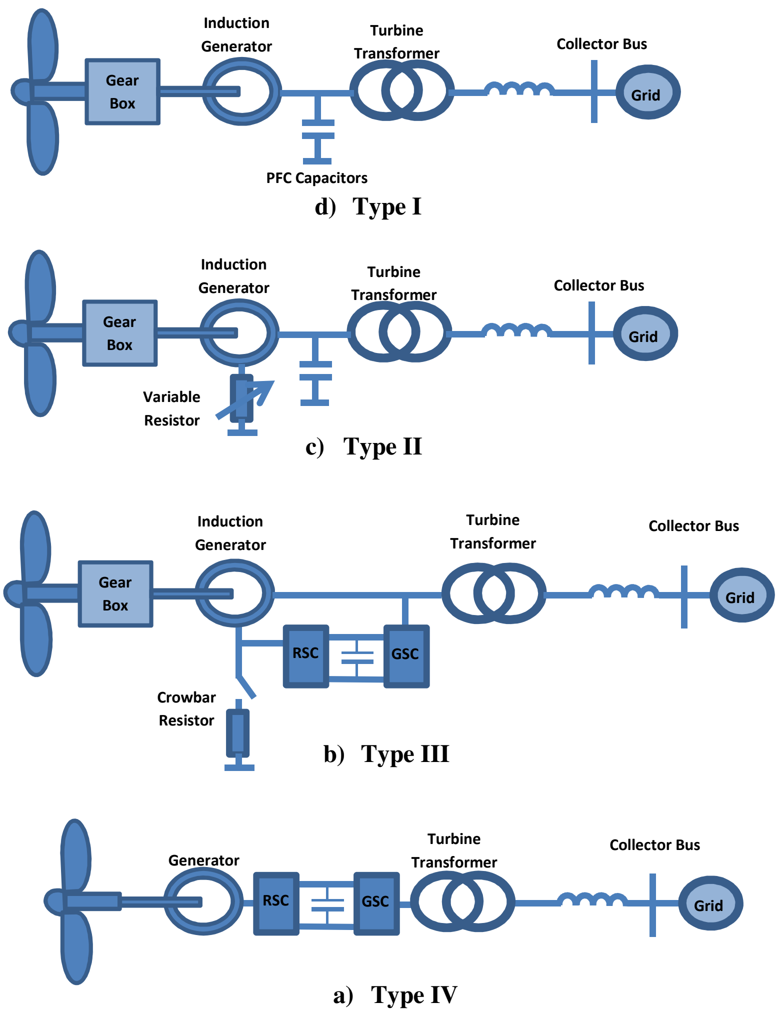

Figure 2.3: Types of WTGs.

The release of the kinetic energy stored in the rotating mass of wind turbines is shown in equation 2.15 and the power released can be calculated as shown in 2.16. Release of power depends upon the initial wind rotor speed (ω_o) and the change in rotor speed ($\triangle\omega$) and duration of drop in rotor speed ($\triangle T$).

$$\triangle E = \frac{1}{2}J(\omega_o^2 - \omega_1^2) \qquad [Joule]$$
$$\Rightarrow \triangle E = \frac{1}{2}J(2\omega_o \triangle \omega - \triangle\omega^2) \qquad [Joule] \tag{2.15}$$

$$\triangle P = \frac{\triangle E}{\triangle T} \qquad [Watt] \tag{2.16}$$

Where,

ω_o = initial speed of the wind turbine rotor[rad/s]
ω_1 = final speed of the wind turbine rotor[rad/s]
$\triangle\omega$ = drop in rotor speed $(\omega_o - \omega_1)$
$\triangle T$ = duration of the drop in rotor speed[s]

Type I WTGs uses SCIG (Squirrel-Case Induction Generator) and type II uses WRIG (Wound Rotor Induction Generator). In both types, wind turbine generators are directly connected to the grid through a transformer and hence, they are capable of contributing inertial response [24]. Type I WTG are termed as fixed speed wind turbines and type II WTG are termed as Limited variable speed concept [25] where the rotor resistance is controlled using a variable external resistance. The rotor power is not fed into the grid unlike in DFIG. Type III and Type IV WTG are converter based wind turbines where partial and full scale converters are used respectively. They are termed as variable speed wind turbines. The use of power electronic converter decouples the generator from grid either partially in case of type III WTGs or fully in type IV WTGs. To better understand the inertial response of type III generators, it is presented in section 2.3.0.2. As the generators in type IV WTG are fully decoupled from the grid, there are no intertial response without the use of additional controller.

2.3.0.2 Doubly-fed induction generator (DFIG) and its inertial response

DFIG is basically a 3-phase wound rotor machine which operates like a synchronous machine. Both, the rotor and stator of the DFIG is connected to electrical sources, hence it is termed as 'doubly-fed' [26]. The rotor is decoupled from the grid, as it is connected through power electronic devices, whereas stator is directly connected to the grid. Hence the rotor mechanical speed is considered to be decoupled from the system frequency. The constant slip (s) with respect to change mechanical speed of the rotor (n_m) is achieved by changing the frequency of the three phase AC current that is fed into the rotor winding with the use of controller [27]. Therefore, total rotational speed of the rotor filed is maintained constant as per equation 2.17.

$$n_r = n_{re} + n_m \tag{2.17}$$

$$s = \frac{n_r - n_s}{n_s} \tag{2.18}$$

$$J\frac{d\omega_r}{dt} = \frac{P_m}{\omega_r} - T_e \qquad [MW] \tag{2.19}$$

Where,

n_r = Total rotational speed of the rotor field [RPM]
n_{re} = Electrical rotational speed of the rotor due to 3-phase AC current [RPM]
n_m = Mechanical rotational speed of rotor[RPM]

s = Slip
T_e = Electromagnetic torque [Nm]

Also, when the grid frequency changes, synchronous speed (n_s) changes and the controller adjust the rotor field speed (n_{re}) to make the slip and electromagnetic torque constant. As seen from equation 2.19, it is obvious that there is no release of kinetic energy in case of grid disturbance, as rotor electrical angular velocity (ω_r) remains constant. Thus there is no inertia response of the machine. But, due to delay in the controlling system to maintain the rotor speed constant as mentioned in [27], inertial response is experienced by the generator for short duration and is insignificant. Modern wind turbine controllers have response time in range of milliseconds. However with the addition of extra controller DFIG can participate in inertial response to the grid [28].

2.4 Energy storage systems and Li-ion batteries

This section provides an overview of different ESS technologies and their comparison by considering different aspects. From this comparison, one technology has been picked for the project application: Li-ion battery. Therefore, there is further description of Li-ion battery characteristics, operating principles and different chemistries. At the end there is a description of battery modeling and battery dynamic. Basic terminology for batteries is given in Appendix A.1.

2.4.1 Classification and comparison of the ESS

The electrical energy can be stored in various ways into the ESS. There are four main types of the ESS: electro-chemical, electromagnetic, mechanical and thermal. The overview of these types and their subtypes is shown in Fig. 2.4. These ESS have different types of characteristics and attributes. Therefore, the choice of an ESS type is further specified by its application. Some technologies of the ESS have additional requirements for geographical conditions (i.e. pumped hydro, compressed air).

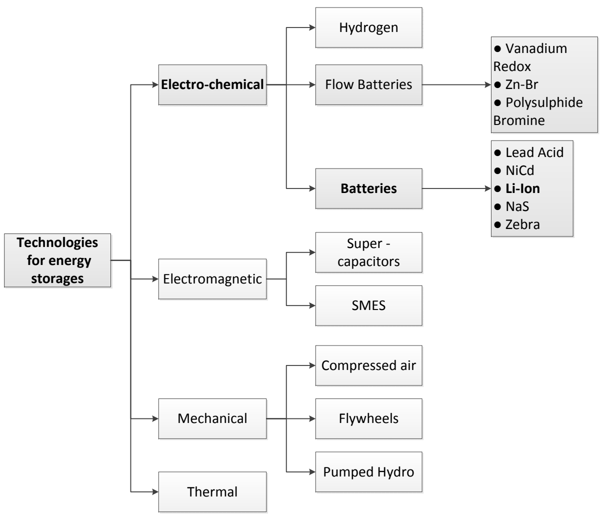

Figure 2.4: Classification of the energy storage technologies.

Fig. 2.5 a) presents a comparison of different ESS technologies according to rated power, energy content and nominal discharge time. It includes present state and the predicted future

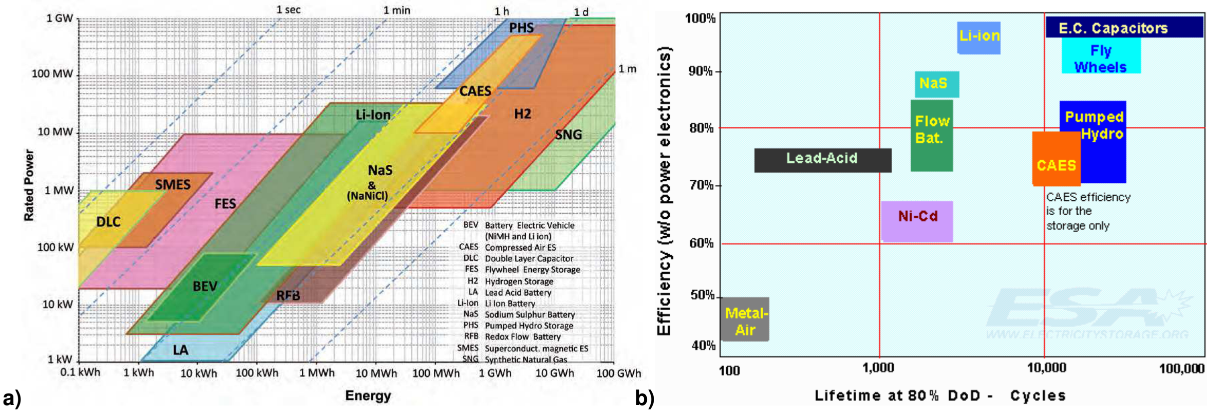

Figure 2.5: ESS technology comparison according to a) rated power, energy content and nominal discharge time [30], b) efficiency and life time [29].

development. It shows that Li-ion batteries can operate in wide range of these quantities. The general comparison of ESS technologies from efficiency and life time perspective is depicted in Fig. 2.5 b) provided by [29] in year 2009 and it shows Li-ion batteries as predominance over the other battery types in terms of efficiency and life time. According to these characteristics of Li-ion batteries, they have been chosen for further studies.

2.4.2 Characteristics and chemistry of Li-ion batteries

The Li-ion battery technology is based on chemical element lithium, which determines the most of its characteristics. Lithium is the lightest metal, which has very high electrochemical potential and consequently very high reactivity. According to these attributes, Li-ion battery has capability to reach high power and energy densities. Table 2.1 presents advantages and disadvantages of Li-ion batteries in relation to the other types of batteries [31].

Table 2.1: The main characteristics of Li-ion batteries compare to the other batteries types [31].

Advantages	**Disadvantages**
High cell voltage	Higher internal impedance
Lack of liquid electrolyte - no leaking	Higher price
High energy and power density	Large safety requirements
Low weight	Need for protective circuits
Low self discharge	Complex measurement of the SOC
Very high coloumbic efficiency	
No memory effect	
Long cycle and calendar life	

Generally a Li-ion battery is composed of an electrolyte and two electrodes. A graphitic carbon creates a base for the negative electrode (anode). A Li-intercalation compound, primarily represented by an oxide, is content of the positive electrode (cathode). Lithium ions are capable of being repeatedly injected and ejected from the electrode structures. During the charging phase, lithium ions are released from cathode and received by anode. During the discharging phase the opposite process takes place. The space between the electrodes is filled by an electrolyte, which carries and transfers Li-ions according to charging-discharging phase. In Fig. 2.6, it is illustrated the structure of this composition [32].

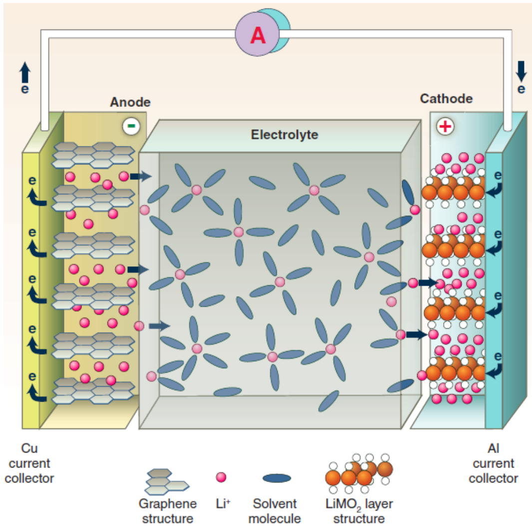

Figure 2.6: Schematic structure of a Li-ion battery [32].

The overall cell reaction of Li-ion battery is expressed in equation 2.20 [33]

$$\begin{gathered} Li_xC + Li_{1-x}MO_2 \leftrightarrow LiMO_2 + C \\ E^0 = 3.3 - 4.2[V] \end{gathered} \tag{2.20}$$

Where,

Li, C, M, O = Lithium, Carbon, metal and Oxygen respectively.
E^0 is cell potential under standard conditions [V]

Li-ion batteries diverge into different types according to their chemical composition. Nowadays, a larger spectrum of materials is used for the cathode. The most common of them are introduced in the upcoming paragraphs. In the case of the anode, there are fewer solutions for modifying or replacing its graphite. In the following summary, there is listed only one anode chemistry, lithium titanate. These different chemical compositions provide variant attributes for batteries. They also vary in the stage of their maturity and the research on them are being carried out [34].

Lithium Cobalt Oxide - $LiCoO_2$: It is considered as a very mature chemistry of Li-ion batteries. Specifically, the voltage of the cell is at 3.7 V. Its main advantage is high energy density. On the other hand, the life time and specific power are referred as moderate or low. Due to the safety, charging and discharging rates are limited by the protective circuits to value around 1C [31], [34].

Lithium Nickel - $LiNiO_2$: The benefits of the lithium nickel battery is high energy density, which is about 30 % more than at cobalt chemistry. However, the cell voltage is lesser at 3.6 V. As the main weakness, there is very high exothermic reaction, which negatively influences safety and increases the demands for cooling [31].

Lithium Manganese Oxide - $LiMn_2O_4$: This chemistry with a three-dimensional lithium manganese spinel structure provides low internal resistance effecting into capability to be (dis)charged by high current. The cell voltage is higher than at cobalt based chemistries at the range from 3.8 to 4.0 V. The other beneficial attribute of this structured chemistry are lower cost, high thermal stability and improved safety. Drawbacks appear in the limited life time and reduced capacity, which is by comparison to $LiCoO_2$ about one third lower. The architecture introduces a range of design variability [31], [34].

Lithium Iron Phosphate - $LiFePO_4$: This chemistry, built up on phosphates, allows to reduce shortcomings of the cobalt chemistry. Mainly it improves thermal and chemical stability, which proceed further into safety. Long cycle life and high current rating belong as well into beneficial attributes of this chemistry. The typical cell voltage is at the level of 3.3 V and furthermore, energy density reaches lower values. From environmental point of view, $LiFePO_4$ stands as very environmentaly friendly in comparison to other chemistries [31], [34].

Lithium Nickel Manganese Cobalt Oxide - $LiNiMnCoO_2$: It is a combination of three metals, where each of them brings in its major attributes. Nickel and cobalt contribute by high specific energy and lower stability, manganese allows creating a spinal structure to reach low internal resistance, however with low specific energy. This chemistry allows to design either high power or high energy cells [34].

Lithium Nickel Cobalt Aluminum Oxide - $LiNiCoAlO_2$: The effect of this chemistry composition results into an increased life time, specific energy and power of the battery. The drawbacks come in safety and high cost [34].

Lithium Titanate - $Li_4Ti_5O_{12}$: Lithium titanate chemistry replaces carbon as the anode material and creates a spinel structure. It provides low internal resistance of the cell and high power stability. This effects into ability to be (dis)charged by high currents around 10 C-rate. Furthermore, $Li_4Ti_5O_{12}$ excels in very long life time of cycles over 10 000. The nominal cell voltage is around 2.4 V. The main drawbacks are lower specific energy and high cost for this cell chemistry [31], [34].

Table 2.2 presents a comparison of the aforementioned Li-ion battery cells' chemistries by summarizing their most important characteristics. Based on the excellent safety and cost characteristic for the $LiFePO_4$ chemistry, this chemistry has been chosen as very suitable solution for the specific parameterization of the ESS application in this work.

Table 2.2: Summary of chemistry characteristics, derived from [31] and [34]. In the scale, "-" represents the worst and "+++" the best.

Chemistry	Specific energy	Specific power	Safety	Life time	Cost	Typical Voltage [V]
$LiCoO_2$	+++	+	+	+	++	3.7
$LiNiO_2$	+++	+	-	+	+	3.6
$LiMn_2O_4$	++	++	++	+	++	3.9
$LiFePO_4$	+	++	+++	+++	++	3.3
$LiNiMnCoO_2$	+++	++	++	++	++	3.6
$LiNiCoAlO_2$	+++	+++	+	+++	+	3.6
$Li_4Ti_5O_{12}$	+	++	+++	+++	-	2.4

2.4.3 Battery dynamic modeling

Applications of batteries require to use an appropriate battery model. Proposed by [35], there can be distinguished three levels of the model scope - market, system and sandwich single-cell level. Structured, they are shown in Table 2.3 together with their main focuses. The market level is typically dedicated to final users, where the main interest is about overall parameters of the battery solution. Research and industry groups operates at the system level to design and produce those solution. As the most detailed, the sandwich level is used, where researchers can study processes between electrodes and an electrolyte and go up to the particle level [35].

Table 2.3: The scope levels of the battery models and their focuses [35].

Market	System	Sandwich
Cost	Underutilization	SEI layer growth
Life	Capacity fade	Side reactions
Safety	Lower energy density	Non uniform current
Performance	Thermal runaway	Loss of particles
		Ohmic resistance
		Mass transfer resistance

Chen and Mora have classified, in [36], the batteries according to their elaboration and complexity in three groups: mathematical, electrochemical and electrical.

Mathematical: These models are constructed by utilization of various mathematical methods (e.g. stochastic, neural networks) and on empirical equations. The disadvantage is that they commonly function only for specific applications, for which they have been designed. Their accuracy is about 5 %-20 %, however often it can be improved in trade off higher computational demands [36].

Electrochemical: It considers electrochemical movements and transport processes. To model them, it is necessary to understand their internal processes and corresponding parameters. They are more complex and provide more precise results. The drawback of this modeling is high computational requirements. Typically they are used to design battery internal attributes, identify elementary processes and provide understanding of interactions [36], [35].

Electrical: They are composed from electrical circuit elements as voltage sources, resistors and capacitors. This structure allows them to be used in a simple way together with other electrical circuits or electrical models in an overall system. Their accuracy puts them in between mathematical and electrochemical models, with an error around 1 %-5 %. The models can vary according to the type of a battery and by that they can have slightly different structure. Based on [36] there are three basic categories of the equivalent electrical models (EEC): Thevenin-, impedance- and runtime-based models. Commonly, the parameters for models are obtained from experimental data and their fitting [35],[36].

2.4.4 Dynamic in charging and discharging of Li-ion battery

Li-ion battery parameters are generally dependent on many factors such as; the SOC, current, temperature and age. By specific assumptions, some of these factors can be neglected since

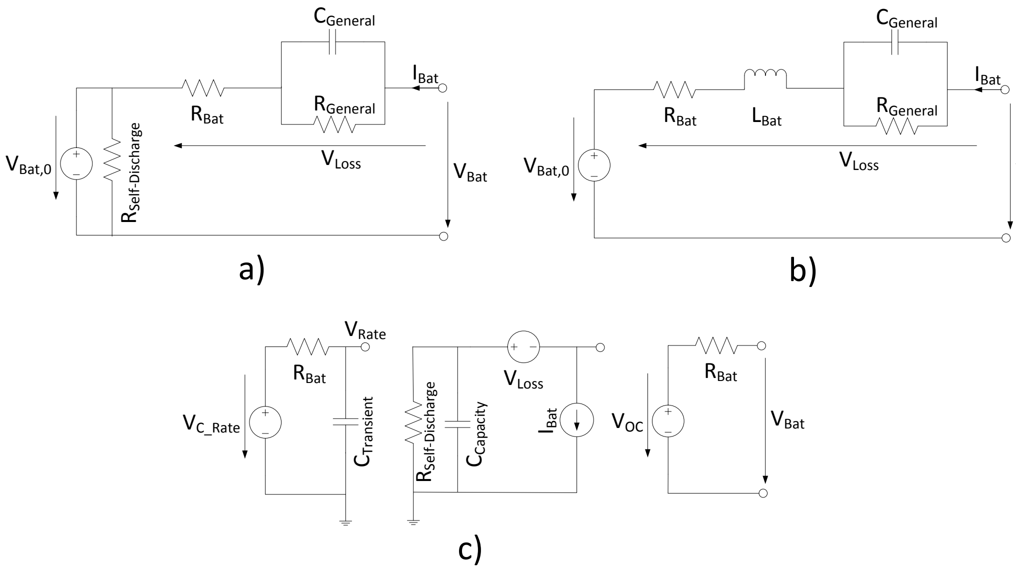

Figure 2.7: Equivalent electrical circuits for: (a) Thevenin-, (b) impedance-, and (c) runtime-based models of a battery.

they are introducing only small error into modeling. For example the assumption of cooling the battery and keeping it at the constant temperature of 25 °C neglects the influence of thermal processes [36].

The cell voltage during the charging and discharging process is determined by the open circuit voltage, cell ohmic resistance, double layer capacity and deficient lithium ion diffusion [37]. With respect to the load sign convention, the voltage of the battery cell is expressed as:

$$V_{Cell} = V_{OCV} + V_{DL} + V_{Diff} + IR_{ohmic} \qquad [V] \tag{2.21}$$

Where,

V_{Cell} = Terminal cell voltage [V]
V_{OCV} = Open circuit voltage (nonlinear dependent on the SOC) [V]
V_{DL} = Double layer capacity voltage [V]
V_{Diff} = Deficient lithium ion diffusion voltage [V]
I = Current applied to the cell [A]
R_{ohmic}= Ohmic resistance [Ω]

There are two approaches, which are used for determining the parameters of the EEC: current pulse method and electrochemical impedance spectroscopy.

Current pulse method: This method is based on applying a charging/discharging current pulse to the battery and observing the voltage response (increase/drop) of the battery. For example, the case of applying a discharging current pulse is considered. The obtained voltage drop is divided into three parts, as it is described in [38]. The first part, an instantaneous drop, is due to the battery ohmic resistance (ohmic voltage loss) and it is described as:

$$R_{ohmic} = \frac{\Delta V_0}{\Delta I} \qquad [\Omega] \tag{2.22}$$

Where,

R_{ohmic} = Ohmic resistance [Ω]
V_0 = Battery voltage - immediately after applying the current pulse [V]
I = Applied current to the battery [A]

The second part occurs in the interval of hundred milliseconds to seconds, after the beginning of the pulse. It is caused by the charge transfer reaction due to the double layer capacity (double layer capacity voltage loss). In the electrodes active material, there appears slow diffusion mechanisms, which determine the third part of the voltage drop (diffusion voltage loss) [38], [39]. Parameter relations of both these parts are generally described by following equation 2.23:

$$\tau = CR \qquad [F] \tag{2.23}$$

Where,

τ = Time constant [s]
C = Double layer/Diffusion capacity [F]
R = Double layer/Diffusion resistance [Ω]

This method is graphically illustrated in Fig. 2.8. There are shown the applied current pulse and voltage response. The described parts of the voltage drop are marked and their corresponding relations to the equivalent electrical circuit are highlighted.

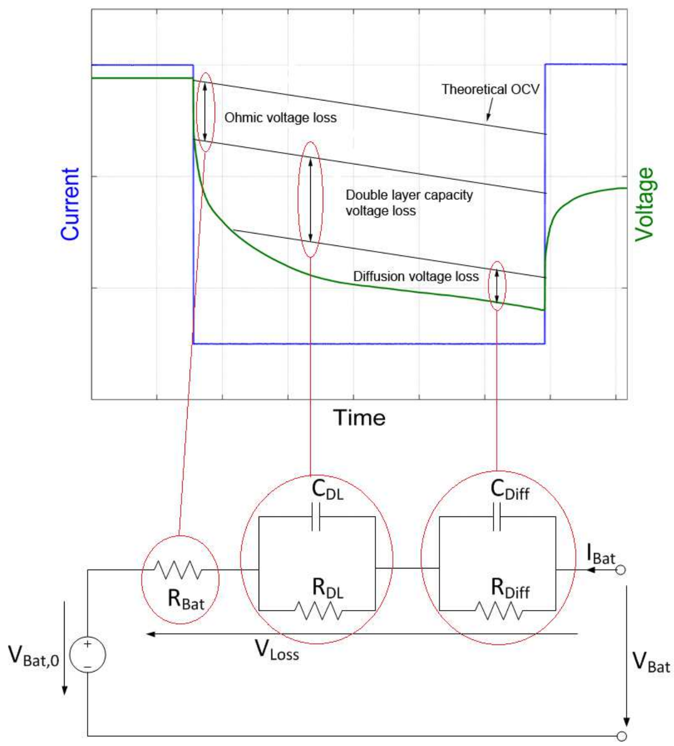

Figure 2.8: Composition of the discharge voltage profile of a lithium-ion battery and its fitting to the equivalent electrical circuit.

Electrochemical impedance spectroscopy (EIS): As a very efficient and precise approach for analyzing a battery, EIS is used for obtaining characteristics and parameters as double layer capacitance, diffusion impedance, the rate of charge transfer and charge transport processes and solution resistance. For performing EIS, a sinusoidal signal is applied to the battery under test. This signal is determined by the used technique. In case of potentiostatic technique, the voltage is applied and the current is observed. In galvanostatic technique it is opposite. The output of this measurement is expressed as a function of the frequency [40], [41].

Furthermore from galvanostatic measurement, the impedance Z can be determined based on the following equations [40]:

$$Z = \frac{u(t)}{i(t)} = \frac{\hat{U} \times sin(\omega t)}{\hat{I} \times cos(\omega t - \phi)} = |Z| \frac{sin(\omega t)}{cos(\omega t - \phi)} \qquad [\Omega] \tag{2.24}$$

$$|Z| = \sqrt{Z_{Re}^2 + Z_{Im}^2} \qquad [\Omega] \tag{2.25}$$

$$Z_{Re} = |Z| \times cos\phi \qquad [\Omega] \tag{2.26}$$

$$Z_{Im} = |Z| \times sin\phi \qquad [\Omega] \tag{2.27}$$

Where,

$\hat{U}$ = Amplitude of the measured voltage signal [V]
$\hat{I}$ = Amplitude of the applied current signal [A]
t= Time [s]
ω = Angular frequency [rad/s]
ϕ = Measured phase shift [rad]
$|Z|$ = Absolute value of the impedance [Ω]
Z_{Re} = Real part of impedance [Ω]
Z_{Im} = Imaginary part of impedance [Ω]

The resulting impedance spectrum is presented in the Nyquist plan, where the imaginary part of the impedance is plotted against its real part. Further, a complex non-linear least squares (CNLS) fitting method [42] is used for processing this EIS curve. By analysing the fitted curve, the EEC parameters are found as described in [43]. This process of deriving parameters is illustrated in Fig. 2.9. Where the resistance R is determined by the diameter of the circle and the capacity C is obtained from the frequency at the position of 90°C corresponding to:

$$\omega = \frac{1}{\tau} = \frac{1}{RC} \qquad [rad/s] \tag{2.28}$$

An example of a typical EIS curve for Li-ion batteries is visualised in Fig. 2.10. The curve is composed of four segments [40], which represent:

1. An inductive behavior (caused by the metallic parts of the cell and wires)
2. Ohmic resistance of the cell
3. Double layer capacity
4. Diffusion mechanisms in the electrode active material

By using the above mentioned method, these segments are fitted and the corresponding parameters for the EEC elements were determined.

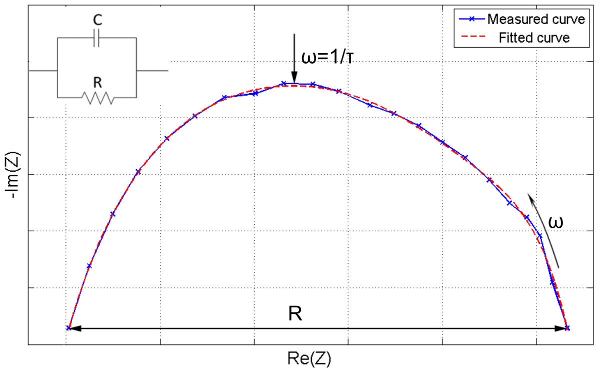

Figure 2.9: Curve fitting and deriving the parameters for parallel RC circuit.

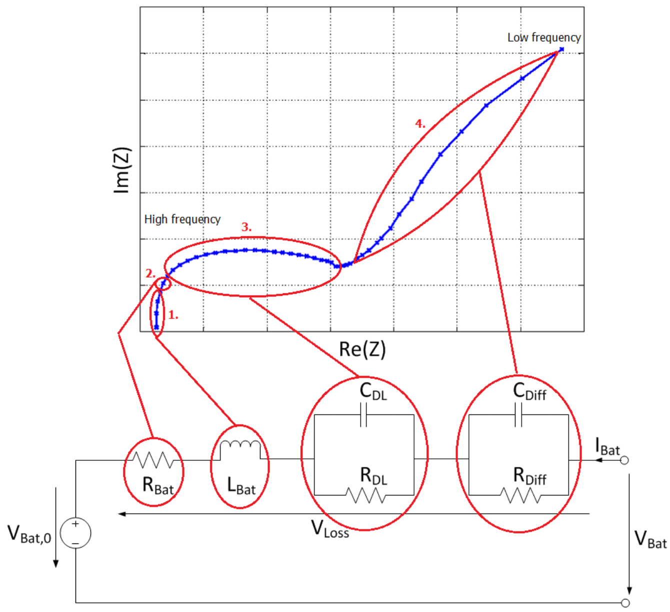

Figure 2.10: Composition of the EIS curve and its fitting to the EEC elements.

2.5 Conclusion

In this chapter, the general concept of rotating machine inertia and the grid frequency responses to the disturbances has been described. Different types of wind turbines and their response to the grid inertia has been presented. Overview of the different ESS technologies have been shown along with the selection criteria of Li-ion batteries. Chemistry, modeling and dynamic involved in Li-ion batteries have been discussed in brief.

3 Modeling and Hardware Interfacing

3.1 System modeling in RSCAD

The typical time step simulations in RTDS are in order of 50 μs, which is not small enough to allow the accurate simulation of high frequency switching circuits such as in PWM. In order to model such system, small time step simulation is used in RSCAD which has time step in order of 1.2 to 2.5 μs. The VSC is modeled in small time step and is interfaced with large time step simulation using appropriate interface transformer available in RSCAD library [44]. System modeled in RSCAD is simulated in RTDS.

3.1.1 12-bus system

The proposed grid model test system consists of the 12-bus system. The generic 12-bus system as presented in [10] has been modified according to the needs, as discussed further, for inertial response studies for WPP. The single line diagram of the generic 12-bus system used for the study purpose is shown in Fig. 3.1. It consists of six 230kV buses including main grid (slack bus), two 345 kV buses and four 13.8-18kV buses.

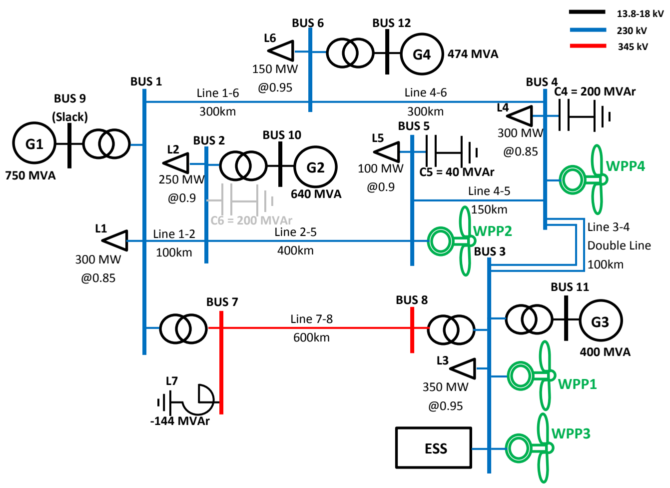

Figure 3.1: 12-bus system.

As for the modification of the 12-bus system, the four 200 MVA wind power plant models as well as battery storage system has been implemented according to the need of study. The generators are equipped with IEEE standard excitation system control and governor control to represent the power system dynamics in order to facilitate the investigation of the impact of WPP inertial response [10]. The modification was done for generator G2 and its associate transformer connected to bus 2 as shown in Fig. 3.1. Generator G2 is scaled and divided into two identical units (G2A and G2B) each of 320 MVA and connected in parallel to represent one bulk unit G2. The necessary parameters of the generator, transformer and loads are provided in Appendix B.1.

3.1.2 Wind turbine generator with full scale converter

The schematic of wind turbine generator(WTG) with full scale converter(FSC) is shown in Fig. 3.2(a). There are two voltage source converter(VSC) and a DC-link capacitor in back to back converter. Both converters are identical and power flow can be bi-directional [45]. For wind turbine application, during power generation mode, the generator side converter acts as rectifier and the grid side converter acts as inverter. The use of back-back converter decouples the generator side from the grid. Hence it is considerable to represent the wind turbine system along with its all mechanical components, aerodynamic and the generator side converter collectively as first order low pass transfer function. The time constant of the transfer function is assumed to be 20ms [46]. The mechanical power from the wind turbine is provided as the input to the transfer function and its output is an equivalent electrical DC power as given in equation 3.1, which on divided by the DC-link voltage gives DC current (I_{DC0}). Hence the norton equivalent circuit can represent the generator side controller as shown in Fig. 3.2(b). The system is further simplified by using ideal voltage source instead of norton equivalent current source as shown in Fig. 3.2(c). Usually a large capacitor is used in the DC side of the VSC.

$$P_m \times \frac{\eta \times 0.01}{1 + sT} = P_{eDC} \tag{3.1}$$

Where,

η = Efficiency of the system [%]
T = Time constant [s]

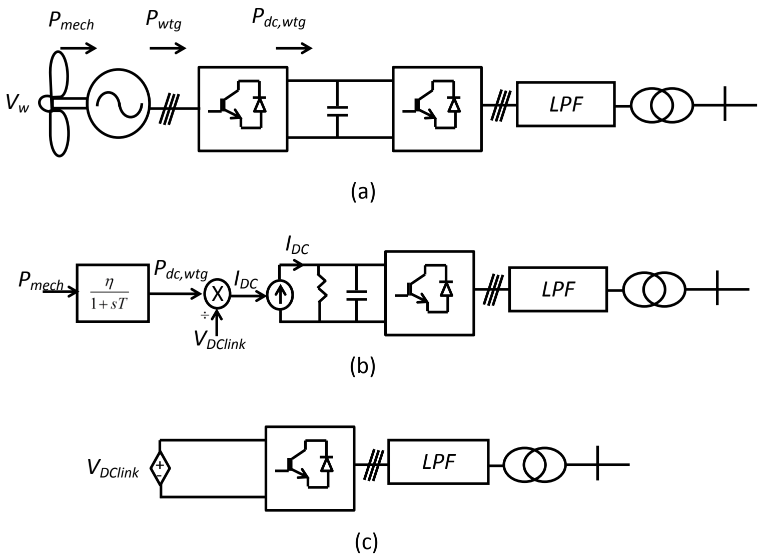

Figure 3.2: Model of WTG-FSC with filter and step-up transformer.

3.1.2.1 Control of grid side voltage source converter

The voltage source converter(VSC) of the grid side is responsible to maintain the voltage across the DC-link capacitor constant regardless of magnitude and direction of the power [45]. In grid side VSC, PWM converter is used with control strategy based on current regulated approach. The basic concept of the vector current control method is to control the instantaneous active and reactive power of the grid, independent to each other [47]. The real component regulates the capacitor voltage and the quadrature component is used to adjust the terminal voltage on the grid side. The vector-control approach provides independent control of active and reactive power between the grid and the converter. For this, the reference frame is oriented along the stator (or supply) voltage vector position. Fig. 3.3 shows the schematic of grid side converter.

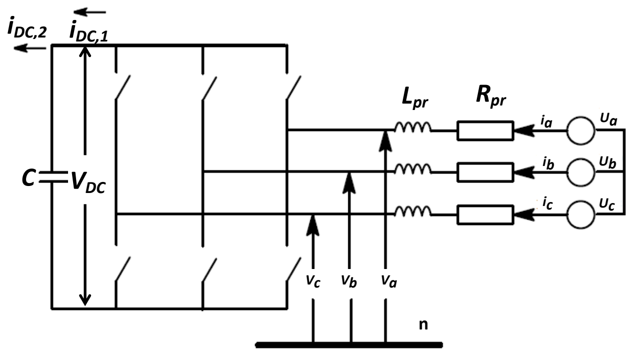

Figure 3.3: Schematic of grid side converter.

The voltage equation across the inductor can be written as 3.2.

$$
\begin{aligned}
v_a &= -R_{pr} i_a - L_{pr}\frac{di_a}{dt} + u_a \\
v_b &= -R_{pr} i_b - L_{pr}\frac{di_b}{dt} + u_b \\
v_c &= -R_{pr} i_c - L_{pr}\frac{di_c}{dt} + u_c
\end{aligned}
\tag{3.2}
$$

Where,

v_a, v_b, v_c = Instantaneous value of converter terminal voltage.
u_a, u_b, u_c = Instantaneous value of grid terminal voltage at the filter bus.
i_a, i_b, i_c = Instantaneous value of phase reactor currents.
R_{pr} and L_{pr} = Resistance and inductance of phase reactor respecively.

Equation 3.2 is transformed into a dq reference frame rotating at ω_e and is represented by equation 3.3

$$
\begin{aligned}
v_d &= -R_{pr} i_d + \omega_e L_{pr} i_q - L_{pr}\frac{di_d}{dt} + u_d \\
v_q &= -R_{pr} i_q - \omega_e L_{pr} i_d - L_{pr}\frac{di_q}{dt} + u_q
\end{aligned}
\tag{3.3}
$$

The active and reactive power flow is given by equation 3.4

$$P = \frac{3}{2}(u_d i_d + u_q i_q)$$
$$Q = \frac{3}{2}(u_q i_d - u_d i_q) \tag{3.4}$$

The angular position of the supply voltage (grid side) is calculated as equation 3.5

$$\theta_e = \frac{d\omega_e}{dt} = \tan^{-1}\frac{u_\alpha}{u_\beta} \tag{3.5}$$

Where, u_α and u_β are the $\alpha\beta$ (stationary 2-axis) grid voltage component. As the converter is controlled in a synchronous reference frame(dq reference frame) that rotates synchronously with the grid voltage vector (u_d and u_q). The d-axis of the reference frame is aligned along the grid voltage position as given by equation 3.5. It can also be extracted using phase lock loop (PLL). The grid flux vector is then aligned along the q-axis. With this alignment, u_q = 0. Thus equation 3.4 can be written as equation 3.6

$$P = \frac{3}{2}u_d i_d$$
$$Q = -\frac{3}{2}u_d i_q \tag{3.6}$$

As the amplitude of the grid voltage is constant, u_d is constant. Hence the instantaneous active and reactive power injected or absorbed from the grid will be proportional to i_d and i_q respectively as given by equation 3.6. The voltage transfer characteristic of the three phase PWM converter is given by equation 3.7.

$$V_{ph,rms} = m_a\frac{V_{DC}}{2\sqrt{2}} \tag{3.7}$$

Where, m_a is the amplitude modulation ratio of the PWM. Neglecting the harmonics due to switching and the losses

$$V_{DC} i_{DC,1} = \frac{3}{2}u_d i_d$$
$$\Rightarrow i_{DC,1} = \frac{3}{4\sqrt{2}}m_a i_d \tag{3.8}$$
$$and,$$
$$C\frac{dV_{DC}}{dt} = i_{DC,1} - i_{DC,2} \tag{3.9}$$

From, equation 3.8 it is clear that the DC link voltage can be controlled by i_d. Hence the current control strategy is based on current control loops for i_d and i_q. The DC link voltage (V_{DC}^*) is compared with the measured DC link voltage (V_{DC}). The error is then fed through the PI controller in order to obtain the reference direct axis current (i_d^*). i_q^* reference determines the displacement factor for the inductors in the grid side [45]. The vector control strategy for the grid side converter is shown in Fig. 3.4. The plant transfer function for the current control loops based on equation 3.3 is given by equation 3.10

$$
\begin{aligned}
F_s = \frac{i_d(s)}{v_d^{'}(s)} = \frac{i_q(s)}{v_q^{'}(s)} \\
= \frac{1}{L_{pr}(s) + R_{pr}}
\end{aligned}
\tag{3.10}
$$

and,

$$
\begin{aligned}
v_d^* = -v_d^{'} + (\omega_e L_{pr} i_q + u_d) \\
v_q^* = -v_q^{'} - (\omega_e L_{pr} i_d)
\end{aligned}
\tag{3.11}
$$

Thus, the controller acts on the current deviated from the reference current signals ($i_d^* + j i_q^*$) to determine the voltage reference signals ($v_d^* + j v_q^*$) for the grid side converter as shown in equation 3.10 and equation 3.11

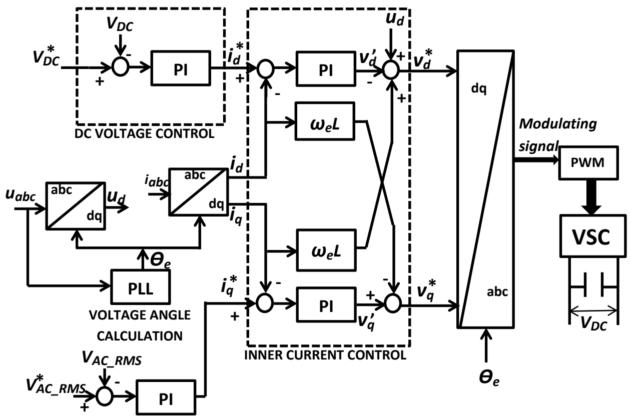

Figure 3.4: The vector control strategy for the grid side converter.

In RTDS library, transformation block for ABC to DQ transformation has the relation as shown in equation 3.12. The phase relation parameter between V_d and V_q is set to "V_q leads V_d", and "θ_e" is fixed at 0.0. For the balance set of positive sequence signals (V_a,V_b and V_c), the output V_q leads V_d by 90 degrees and V_q remains in phase with V_a.

$$
\begin{bmatrix} V_d \\ V_q \\ V_0 \end{bmatrix} = \frac{2}{3} \begin{bmatrix} \cos(\theta_e) & \cos(\theta_e - 120) & \cos(\theta_e + 120) \\ \sin(\theta_e) & \sin(\theta_e - 120) & \sin(\theta_e + 120) \\ \frac{1}{2} & \frac{1}{2} & \frac{1}{2} \end{bmatrix} \begin{bmatrix} V_a \\ V_b \\ V_c \end{bmatrix}
\tag{3.12}
$$

In order to ease the scaling of the system, the control scheme of VSC is per unitized in dq reference frame in RTDS. The per unit value of ac quantities are based on their peak values. The output current from the grid side VSC are electrically noisy. Most of the noises are filtered through high pass filter. In addition, low pass filter is used at the input of the measure of the grid phase currents. The phase currents are scaled in the low pass filter and converted to dq using ABC/DQ block available in RTDS library. Fig. 3.5 shows the implementation of ABC to DQ in converter in RTDS. Due to the use of filter, there are attenuation and phase shift in current whose effects can be seen at the output DQ values. Hence it is compensated with the desired value.

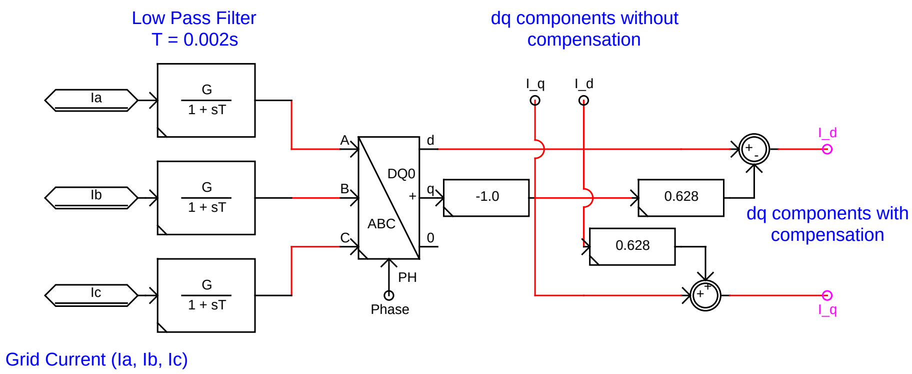

Figure 3.5: Implementaion of DQ transformation in RTDS with Low pass filter and compensation.

The effect of the low pass filter in steady state can be represented as equation 3.13 and is shown in Fig. 3.6

$$G(j\omega_o) = \frac{1}{1 + j\omega_o\tau} = Me^{j\phi} \tag{3.13}$$

Where, M and ϕ and τ are the magnitude, phase shift and the filter time constant respectively. To cancel this effect, a space vector is defined as ($\vec{I_{\alpha\beta}}$).

$$\vec{I_{dq}} = I_d + jI_q \tag{3.14}$$

After filtering, it becomes

$$\vec{I_{Fdq}} = Me^{j\phi}\vec{I_{dq}} = \mathbf{M_1}\vec{I_{dq}}$$
$$\begin{bmatrix} I_{Fd} \\ I_{Fq} \end{bmatrix} = \begin{bmatrix} M\cos\phi & -M\sin\phi \\ M\sin\phi & M\cos\phi \end{bmatrix} \begin{bmatrix} I_d \\ I_q \end{bmatrix} \tag{3.15}$$

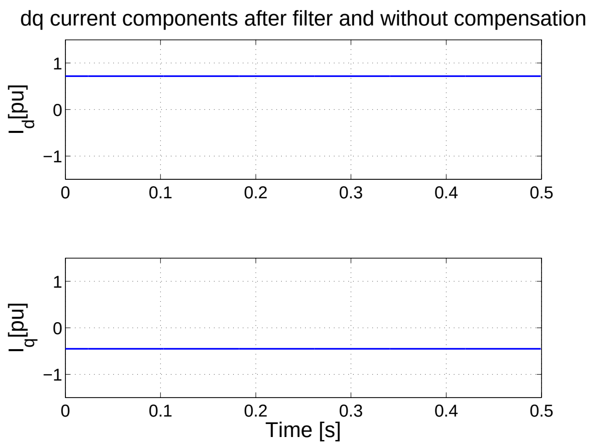

Figure 3.6: DQ current components after use of low pass filter.

Taking the inverse of the above expression as in equation 3.20 and multiplying its result to the output of ABC to DQ transformation block removes the steady state effect of filter [44]. For the base frequency of 50Hz and filter time constant of 0.002, from equation 3.13, the following transform function is obtained.

$$G = \frac{1}{1 + j2\pi \times 50 \times 0.002} = 0.7170 - 0.4505i \tag{3.16}$$

$$\mathbf{M_1} = \begin{bmatrix} Re(G) & -Im(G) \\ Im(G) & Re(G) \end{bmatrix} = \begin{bmatrix} 0.7170 & 0.4505 \\ -0.4505 & 0.7170 \end{bmatrix} \tag{3.17}$$

$$\mathbf{M_1^{-1}} = \begin{bmatrix} 1 & -0.6283 \\ 0.6283 & 1 \end{bmatrix} \tag{3.18}$$

$$\begin{bmatrix} I_d \\ I_q \end{bmatrix} = \begin{bmatrix} 1 & -0.6283 \\ 0.6283 & 1 \end{bmatrix} \begin{bmatrix} I_{Fd} \\ I_{Fq} \end{bmatrix} \tag{3.19}$$

Hence, after the use of appropriate compensation the dq-current components are shown in Fig. 3.7.

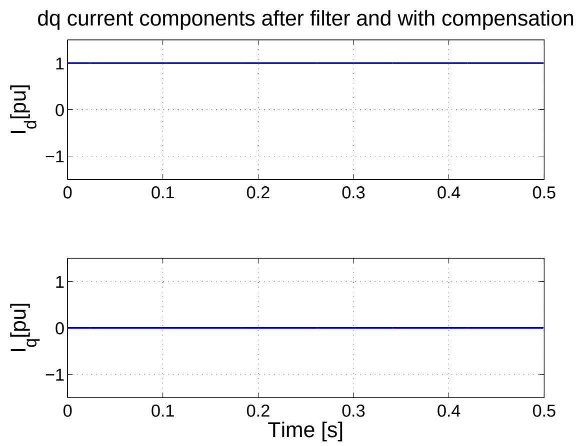

Figure 3.7: DQ current components after use of low pass filter and compensations.

3.1.2.2 High pass filter(RLC)

The use of PWM using power electronic converters with high frequency switching, causes switching ripples and current/voltage harmonics within the vicinity of switching frequency [48]. These ripples and harmonics produced can cause disturbance to other sensitive devices connected to the grid. Apart from disturbances, harmonics also produces extra losses. The shunt filter acts as the short circuit path for the high frequencies and open circuit for the low frequency component. If the filter is not designed properly, there is chances of occurrence of resonances due to the converter current or network voltage harmonics [48]. The factor that effects the design of filter is the amount of reactive power produced by the filter which increases as the filter capacitance increases. The capacitor of the RLC filter can be chosen so that at nominal frequency of 50Hz, the shunt filter behaves as high impedance. The impedance of the capacitor can be selected as certain percentage (e.g, 10%) of the MVAr rating of the generator or certain percentage of the per unit impedance of the system.

After selecting the filter capacitor and neglecting the parallel resistor, a LC circuit is formed. The value of inductance is selected such that resonance occurs at switching frequency. Hence the impedance of capacitor and inductor cancels each other to provide low resistance path to ground.

$$\omega_{res} = 2\pi \times f_{switch} \tag{3.20}$$
$$L_f = \frac{1}{\omega_{res}^2 C_f} \tag{3.21}$$

Where,

ω_{res} = Resonant Frequency [rad/s]
L_f= Filter inductor [H]
f_{switch} = Switching frequency [Hz] C_f= filter capacitance [F]

After selecting L_f and C_f, the value of filter resistance(R_f) is selected equal to the impedance of inductance connected in parallel.

$$R_f = \omega_{res} L_f \tag{3.22}$$

3.1.2.3 Phase reactor

The line reactors are the inductors in series with the line. The function of the phase reactor is to attenuate the converter switching ripple current [48]. The current output from the PWM has high ripples and phase reactor helps in smoothing the current as well.

3.1.2.4 Tuning of PI controller

By applying the Laplace transform in equation 3.3, the following transfer function can be obtained.

$$\begin{aligned} I_d(s) &= G(s)U_d(S) \\ I_q(s) &= G(s)U_q(S) \end{aligned} \tag{3.23}$$

where,

$$G(s) = \frac{1}{L_{pr}s + R_{pr}} \tag{3.24}$$

Grid side converter controller
Considering that the close loop current for i_d and i_q are similar, the open loop($G_o(s)$) and close loop ($G_c(s)$) transfer function for PI controller can be written as 3.25 and 3.26 respectively [49].

$$G_o(s) = \frac{k_p s + k_i}{s(L_{pr}s + R_{pr})} \tag{3.25}$$

$$G_c(s) = \frac{k_p s + k_i}{L_{pr}s^2 + (k_p + R_{pr})s + k_i} \tag{3.26}$$

Where k_p and k_i are the proportional and integral constant. The poles of equation 3.26 can be found by choosing the correct value of k_p and k_i. The characteristic polynomial of the system for close loop poles are given by the denominator of equation 3.26.

$$L_{pr}s^2 + (k_p + R_{pr})s + k_i = 0 \tag{3.27}$$

Comparing equation 3.27 with the second order system characteristic equation 3.28, we get 3.29 and 3.30, where ζ and ω_n defines the damping ratio and the natural frequency of the system oscillation.

$$s^2 + 2\zeta\omega_n s + \omega_n^2 = 0 \tag{3.28}$$

$$\begin{aligned} \omega_n^2 &= \frac{k_i}{L_{pr}} \\ \Rightarrow k_i &= L_{pr}\omega_n^2 \end{aligned} \tag{3.29}$$

$$\begin{aligned} 2\zeta\omega_n &= \frac{k_p + R_{pr}}{L_{pr}} \\ \Rightarrow k_p &= 2\zeta\omega_n L_{pr} - R_{pr} \end{aligned} \tag{3.30}$$

ω_n and ζ are determined by selecting the settling time (t_s) and the maximum overshoot (M_p). (t_s) and (M_p) are defined by equation 3.31 and 3.32 respectively.

$$t_s = \frac{4}{\zeta\omega_n} \tag{3.31}$$

$$M_p = e^{-\frac{\pi\zeta}{\sqrt{1-\zeta^2}}} [\%] \tag{3.32}$$

After substituting the vaule of ω_n and ζ found from equation 3.31 and 3.32 in equation 3.29 and 3.30, k_i and k_p are found.

According to internal model controller concept, to make the close loop transfer function $G_c(s)$ as shown in equation 3.33, the PI transfer function as shown in equation 3.34 can be placed

$$G_c(s) = \frac{1}{\tau s + 1} \tag{3.33}$$

$$G_{PI}(s) = \frac{L_{pr}s - R_{pr}}{\tau s} \tag{3.34}$$

$$\Rightarrow G_{PI} = \frac{L_{pr}}{\tau} + \frac{R_{pr}}{\tau}\frac{1}{s} = k_p + k_i\frac{1}{s} \tag{3.35}$$

Where the rising time (t_r) is taken as 10 times the sampling time (T_s); i.e. $(t_r = 10T_s)$ and $t_r = \tau ln9$.

DC link voltage controller

from equation 3.8, the close loop transfer function of the system for the DC link voltage controller can be written as equation 3.36 and its characteristic equation is represented in equation 3.37

$$G_c(s) = \frac{k_p s + k_i}{Cs^2 + k_p s + k_i} \tag{3.36}$$

$$s^2 + \frac{k_p}{C}s + \frac{k_i}{C} \tag{3.37}$$

Comparing equation 3.37 with 3.28 we get k_p and k_i as

$$k_p = 2\zeta\omega_n C \tag{3.38}$$

$$k_i = C\omega_n^2 \tag{3.39}$$

Also, according to internal model controller concept as discussed earlier, to make the close loop transfer function $G_c(s)$ as shown in equation 3.33, the PI transfer function as shown in equation 3.40 can be placed

$$G_{PI}(s) = \frac{Cs}{\tau s} \tag{3.40}$$

$$\Rightarrow G_{PI} = \frac{C}{\tau} \Rightarrow G_{PI} = k_p \tag{3.41}$$

Ziegler-Nichols tuning rule

Method of the stability margin:

In this method, the controller is switched to only proportional (P) mode. the following action are used.

1. The gain of the P controller is increased continuously starting from the lowest possible value until the closed loop shows permanent oscillations. At this state, the value of the gain is denoted as critical gain (K_{crit}).
2. Measure the period of the oscillations with the critical gain value (T_{crit}).
3. Determine the K_p and K_i value using the following equation 3.42 and 3.43.

$$k_p = 0.45K_{crit} \tag{3.42}$$

$$\begin{aligned} T_i &= 0.8T_{crit} \\ \Rightarrow K_i &= \frac{1}{T_i} \end{aligned} \tag{3.43}$$

3.1.2.5 Phase lock loop(PLL)

Phase-locked-loop (PLL) is used for computing the grid voltage phase displacement and frequency information. Grid voltage displacement is necessary for the system control as well as synchronization of the output from the grid side VSC with the grid. It is an important part of the grid connected VSC. The basic structure of PLL consist of a phase detector (PD), lowpass loop filter(LF) and a voltage controlled oscillator (VCO) as shown in Fig. 3.8.

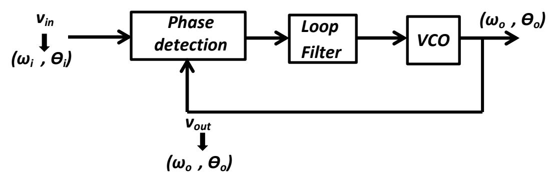

Figure 3.8: Closed-loop synchronization structure.

The phase angle difference between the input and output signal is detected by the PD and is passed through lowpass filter (LF) to smooth the error signal. The output signal from the LF drives the VCO to generate the output signal that can follow the input signal. Voltage controller oscillator (VCO) is a circuit module which oscillates with a controlled frequency (ω = 314.16 rad/s for 50Hz system). The output from the PLL are phase angle and angular frequency of the input variable. The phase angle is used for abc to dq transformation and dq to abc transformation [50].

In order to maintain the synchronization in presence of harmonics and sub-harmonics, PLL based on based on the instantaneous real and imaginary power theory (SRF-PLL) is used [50]. The block diagram of the SRF-PLL available in the RTDS library is shown in Fig. 3.9.

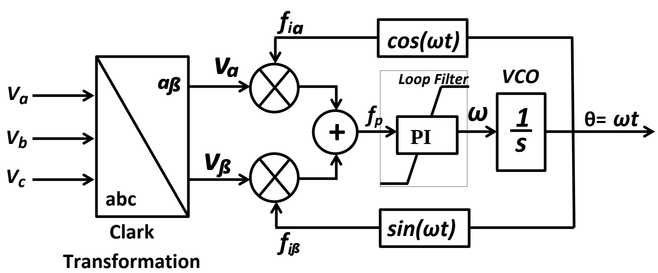

Figure 3.9: Block Diagram of SRF-PLL.

Using Clark transformation, the $\alpha\beta$ components $(V_\alpha + jV_\beta)$ of the input line voltages are obtained from the line voltages (V_a, V_b, V_c) are obtained. The phase error(f_p) between the input signal $(V_\alpha + jV_\beta)$ and the VCO outputs $(f_{i\alpha} + jf_{i\beta})$ is calculated as the sum of the product of the individual components and is the input error signal for the PI controller. In steady state condition, the output from VCO leads the input reference signal by 90^o [50].

3.1.3 Energy storage system (ESS) with converter

The similar converter as presented for wind turbine grid side VSC is scaled down to 25 MW system for the ESS. However, the power provided by the converter depends upon the size of the ESS. The control scheme of the ESS is modified in order to follow the power command from the controller designed in dSPACE. The schematic of the ESS controller is presented in Fig. 3.10. The reference direct axis current (i_d^*) regulates the power transfer between the grid and ESS based on the power command P_{BATT} received from ESS controller. i_d^* is generated by diving the power command received for ESS (P_{BATT}) with U_d. The DC link voltage is not regulated as in case of wind turbine VSC and it is determined by the ESS voltage. The operating range of the ESS voltage is limited by safety control.

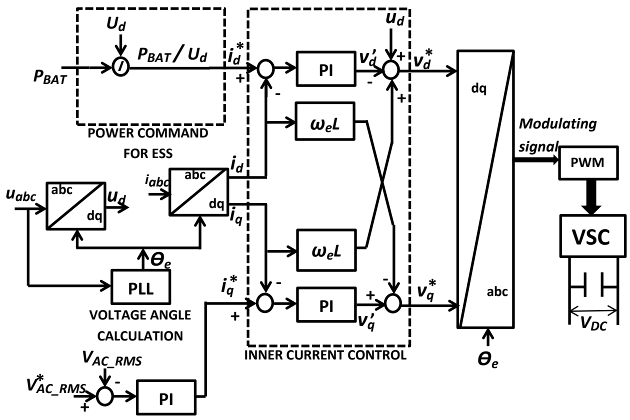

Figure 3.10: Block Diagram of VSC controller for ESS.

3.2 Energy storage system - modeling and simulation

This chapter describes the modeling of the ESS, its control and implementation in dSPACE, which is used as a real time platform, where the ESS model is run.

3.2.1 dSPACE Simulator and its environment

The dSPACE Simulator is a powerful computational system. It is widely used for realtime and hardware-in-the-loop (HIL) simulations. It brings many advantages into developing and integrating processes, because it allows to test direct interactions of connected systems. The dSPACE environment has fully built-in support for MATLAB® and Simulink® software. Therefore, models and scripts are converted to C and run at dSPACE realtime processor via MLIB/MTRACE interface. The scheme of this process is shown in Fig. 3.11. The specific dSPACE processor board used for simulations is DS1006. As an extension for hardware connection of input/output (I/O), the modular boards, DS2002 and DS2103 are added. The Simulink® blocks for I/O hardware communication are available in dSPACE extended library [51].

The step size of the dSPACE Simulator is set as 1 ms.

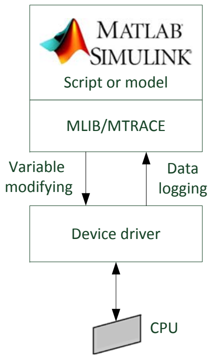

Figure 3.11: The process scheme for accessing dSPACE realtime processor.

Figure 3.12: The picture of the dSPACE Simulator.

3.2.1.1 ModelDesk

ModelDesk is the software used for parameterization and configuration of the Automotive Simulation Models (ASM), which belongs to the dSPACE Model Packages. It provides graphical user interface, see Fig. 3.13, where components are visualized and specific parameters are set [51].

3.2.1.2 ControlDesk

ControlDesk is used as a tool for control and monitoring of experiments. In real time, it allows to observe and save parameters as well as control the running system. The interface example is shown in Fig. 3.14. For saving synchronized data dSPACE-RTDS, the trigger signal from RTDS is implemented.

3.2.2 Overall ESS model

The whole ESS model, except the power electronic interface (*PEI*) and the converter control unit (CCU), is created in Simulink®and run at dSPACE Simulator. It is divided into four main parts. The first part is the input from the RTDS and its conversion, which contains the signal of frequency measurement (f) and power processed (P_p). The second part is the energy management system (EMS), which represents the superior control of the ESS. The third part is the model of the battery. The fourth part is the output to the RTDS with the signals of the power requested (P_r) and the terminal voltage of the battery (V_{Bat}). Schematically, it is shown in Fig. 3.15.

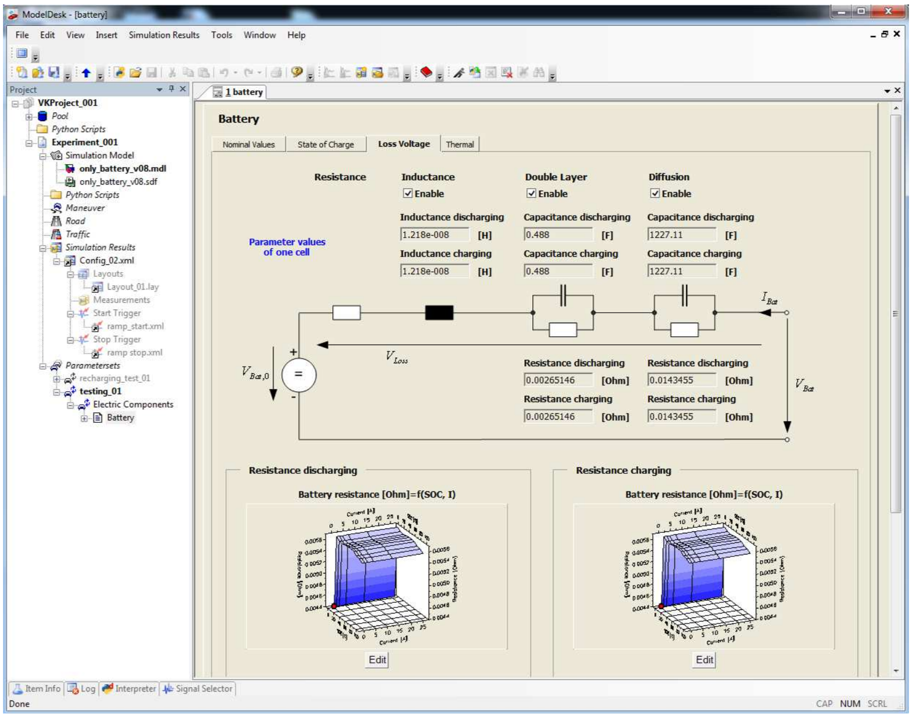

Figure 3.13: An illustration of the ModelDesk screen.

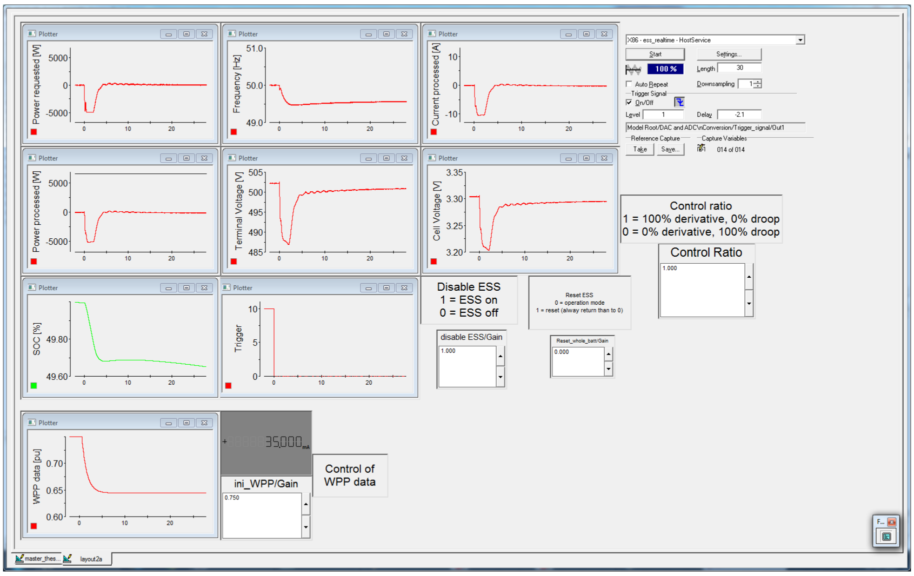

Figure 3.14: An illustration of the ControlDesk screen.

3.2.3 Battery model

The battery model is developed based on the following procedure. At first, the general electric equivalent model of the battery is introduced. Than its specification is done according to the lithium-ion battery based on $LiFePO_4$ chemistry.

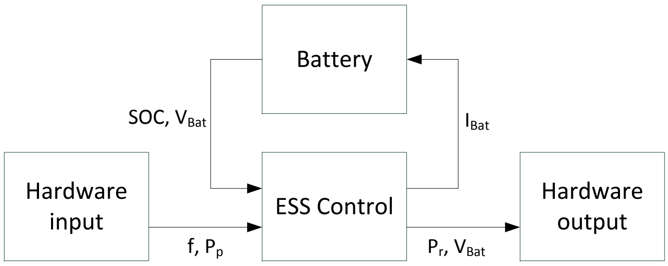

Figure 3.15: The scheme of the battery model in Simulink®.

3.2.3.1 The general electric equivalent model

This dynamic battery model is based on the dSPACE Automotive Simulation Models [52]. It is modeled with respect to load sign convention. As input, variable charging (positive) or discharging (negative) current is used. The temperature of the battery is assumed to keep constant at 25 °C, other thermal influence and thermal losses are neglected. As the output, the terminal voltage, the cell voltage and the SOC are computed. The terminal voltage represents multiplication of the individual cell voltage by the number of cells in series. As the limitation of the ModelDesk for modeling the battery system, it is allowed to connect the cells only in series. Therefore the battery model in Simulink® represents only one series line of cells, which number of cell is constant. The simplifying approach for scaling up the power of the ESS is to connect this series line in parallel with another identical lines. This will result only in multiplying the output power with the considered number of parallel lines; this factor is applied on the RTDS side. The used electric equivalent circuit for modeling the battery is shown in Fig. 3.16.

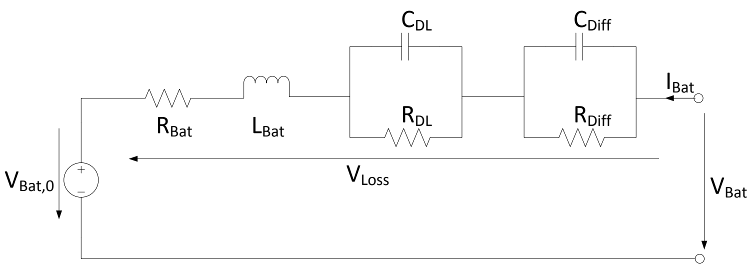

Figure 3.16: The layout of the used impedance-based electric equivalent circuit.

The terminal voltage is obtained from the impedance-based electrical equivalent circuit. It includes internal resistance, inductance, double layer behavior and diffusion behavior, which represents the loss voltage. The loss voltage is calculated as:

$$V_{Loss} = \frac{1}{C_{DL}} \int (I_{Bat} - \frac{V_{CDL}}{R_{DL}}) + \frac{1}{C_{Diff}} \int (I_{Bat} - \frac{V_{CDiff}}{R_{Diff}}) + I_{Bat} R_{Bat}(SOC) + \frac{dI_{Bat}}{dt} L_{Bat} \qquad [V] \quad (3.44)$$

Furthermore, the circuit contains a voltage source, which represents the OCV dependent on SOC over all the cells in the series line. It is expressed in following equation:

$$V_{Bat,0} = n_{Cell} V_{Cell}(SOC) \qquad [V] \quad (3.45)$$

By summing up the loss voltage and the open-circuit voltage over the cells, the terminal voltage is obtained as it is described in Equation 3.46:

$$V_{Bat} = V_{Bat,0} + V_{Loss} \qquad [V] \tag{3.46}$$

Where,

V_{Loss} = Loss voltage [V]
V_{CDL} = Loss voltage double layer capacitance [V]
V_{CDiff} = Loss voltage diffusion capacitance [V]
$V_{Bat,0}$ = Open circuit voltage [V]
V_{Cell} = Cell voltage[V]
V_{Bat} = Battery terminal voltage [V]
I_{Bat} = Battery current [A]
C_{DL} = Double layer capacitance [F]
C_{Diff} = Diffucion capacitance [F]
R_{DL} = Double layer resistance [Ω]
R_{Diff} = Diffusion resistance [Ω]
R_{Bat} = Battery internal resistance [Ω]
L_{Bat} = Battery inductance [H]
t = Time [s]
n_{Cell} = Number of battery cells in series
SOC = State of charge [%]

The SOC determination is based on the coulomb counting, which is expressed as following Equation 3.47:

$$SOC = SOC_0 + \frac{1}{K_N}\int I_{Bat}dt \qquad [\%] \tag{3.47}$$

Where,

SOC = State of charge [%]
SOC_0 = Initial state of charge [%]
K_N = Nominal capacity of the battery [Ah]
I_{Bat} = Battery current [A]
t = Time [s]

3.2.3.2 Parameterizing the battery model

As the battery type and chemistry for this work, the lithium-ion battery based on $LiFePO_4$ have been chosen because of its very good and suitable characteristics and attributes. The parameterizing itself is done through ModelDesk. The specific data are found out and derived from the manufacturer's datasheets, as shown in Table 3.1, and experimental measurements. The battery model contains 152 cells connected in series.

Table 3.1: The technical specification for the Li-ion $LiFePO_4$ battery [53], [54].

Nominal Cell Capacity	2.5 Ah
Nominal Cell Voltage	3.3 V
Maximum continuous charge current	10 A
Maximum continuous discharge current	50 A
Cut-off undervoltage limit	2.0 V
Cut-off overvoltage limit	4.0 V

The open circuit voltage of the cell as a function of SOC was obtained from the experimental measurements and it is presented in Fig. 3.17.

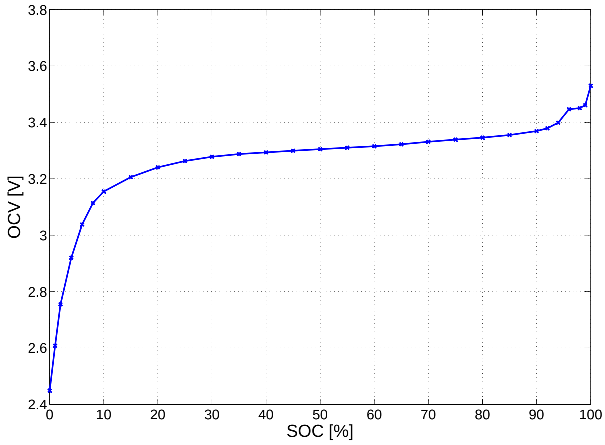

Figure 3.17: The applied profile of open-circuit voltage as a function of the SOC.

For determining the parameters for the impedance-based equivalent electrical circuit of one cell, CurveFitting and Parameter Extraction tools provided from [55] have been used. The overview of MATLAB based graphical user interface (GUI) is presented in Fig. 3.18. The GUI allows to fit input data from EIS measurements and then derives the parameters for the circuit. Before fitting, initial parameters have to be entered. By setting boundaries, the result parameters can be farther adjusted for reducing the final error of the complex nonlinear least squares fitting.

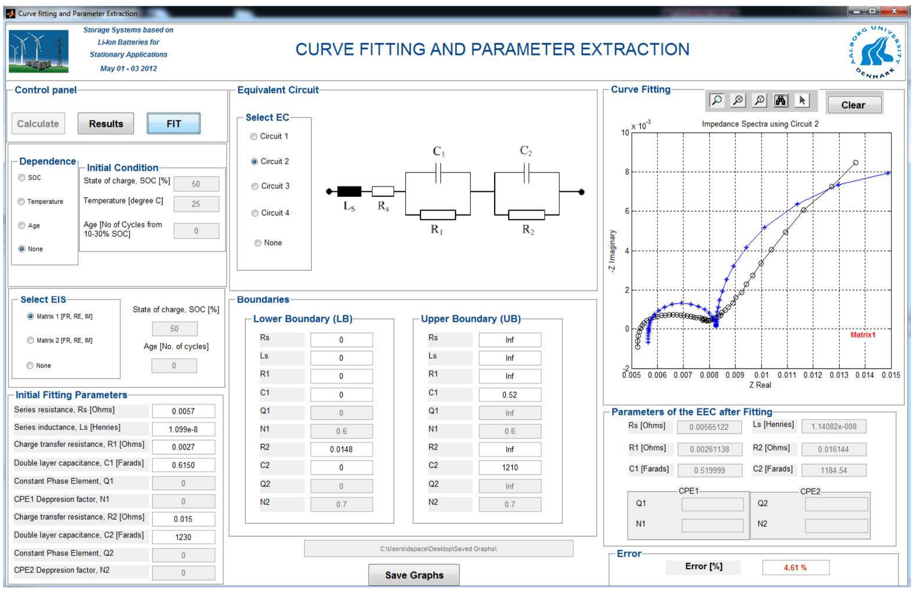

Figure 3.18: Illustration of the CurveFitting and Parameter Extraction tool interface.

The data from EIS measurements for different levels of the SOC with 10 % resolution has been applied to this tool. By their fitting and minimalizing the error, the values for the circuit elements have been found and they are presented in Appendix B.3. Final constant values for the equivalent electrical circuit have been derived as their arithmetic mean for the SOC in the range between 10 % and 90 % and they are shown in Table 3.2.

Table 3.2: The derived parameters for equivalent electrical circuit in the model.

L$_{Bat}$ [nH]	R$_{DL}$ [mΩ]	C$_{DL}$ [mF]	R$_{Diff}$ [mΩ]	C$_{Diff}$ [F]
12.1833	2.6515	488.0000	14.3455	1227.1100

The internal resistance of the battery (R$_{Bat}$) is considered as a function of SOC. It is based on the extracted values, that are summarized in Table B.5 and its SOC dependence is illustrated in Fig. 3.19. The values of R$_{Bat}$ are implemented in the battery model as a look-up table.

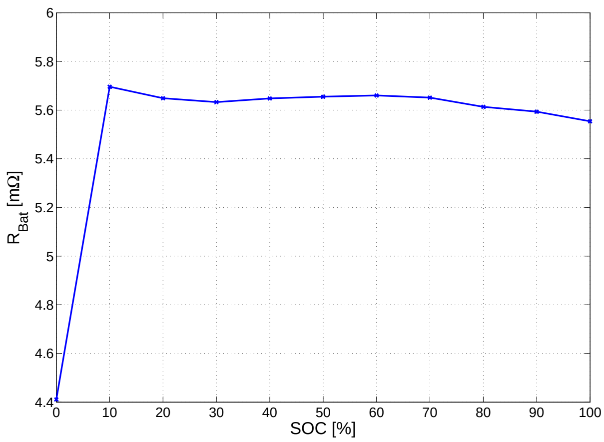

Figure 3.19: The applied profile of battery internal resistance as a function of the SOC.

The influence of temperature and (dis)charging current to the battery parameters is neglected in the model.

3.2.4 Energy management system

The EMS of the ESS is primary designed to provide inertial response and furthermore it includes safety and recharging parts for the batteries. Based on this, it computes demanding current for the battery. From the current and the battery terminal voltage the requested power is computed for transferring to/from the ESS. This power request is sent to the CCU, simulated in RTDS. From RTDS, there is transferred signal with power in real processed to the ESS in RTDS simulation. From this real power is computed current to the battery. The scheme of the control as a flowchart is shown in Fig. 3.20.

3.2.4.1 Inertial response controller

The control for the intertial response integrates derivative and droop control, which has been derived from [14] and [56]. It allows to operate the ESS in three control modes: only derivative, only droop and combination control. The gain, which represents control ratio, is set and controlled from ControlDesk interface. Setting values and their meaning are shown in following Table 3.3.

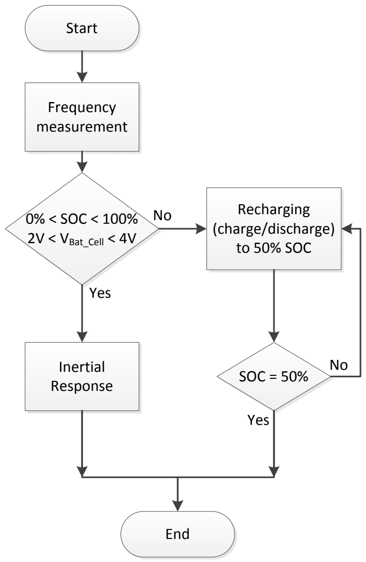

Figure 3.20: The flowchart with the recharging/safety parts and a general inertial response part for the ESS control.

Table 3.3: Representation of control gain values for control modes.

Gain value	Control mode
1	only derivative
between 0 and 1 *e.g. 0.6*	combination *60 % derivative 40 % droop*
0	only droop

The scheme of the inertial response control is illustrated in Fig. 3.21. The input signal is frequency measurement, which continues to the derivative and droop control parts.

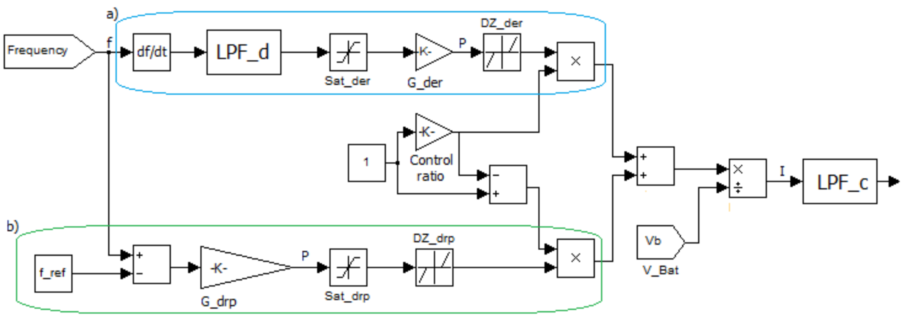

Figure 3.21: The scheme of the inertial response controller, a) derivative control, b) droop control.

Derivative control: Frequency signal is derivated and proceeds to the low-pass filter(*LPF_d*). The filter has been experimentally set to reach desired response and the approach for it is described below. Further, the signal is limited into an interval (*Sat_der*), which determines it's minimum and maximum values. The next step is to multiply the signal by the nominal power of one cell series line (*G_der*). By the dead zone (*DZ_der*) is set the band for no inertial response of the ESS to prevent reaction on too small deviations or noise. As the last step, the control ratio is applied.

LPF_d is set according to the following approach. For visualizing it, Fig. 3.22 is shown as an example. The frequency drops about 1 Hz in time period of 2 s. The derivative of the frequency, which responds to this drop, is 0.5 Hz/s. The initial desired response of the ESS for this case is to react and provide 40 % of its nominal power in 0.25 s after the beginning of falling frequency (values of the response are listed in 5 % resolution). The response continues and in 0.5 s it is 65 %, in 1.0 s it is 85 %, in 1.5 s it is 95 % and in 2.0 s it is full power of the ESS (100 %).

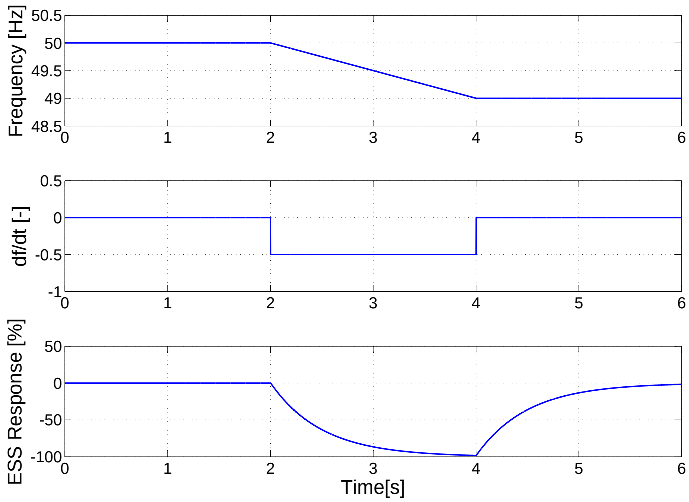

Figure 3.22: Graphs for the approach to derive LPF_d value. There is shown frequency, derivative of frequency and response of the ESS, respectively.

Droop control: It has similar behavior as a control for the primary frequency regulation, however as a part of the EMS, it is designed for the inertial response and it is proposed as time limited service, however due to observation period of 30 s in performed simulations, the time limitations have not been implemented. The measured signal is compared to the reference frequency (*f_ref*) and it is multiplied by gain (*G_drp*), which represents the response of the ESS system for the frequency deviation of 1 Hz from the reference frequency. After that, the maximum allowed demand for power is limited into an interval (*Sat_drp*), typically representing the nominal power of the ESS and the dead zone (*DZ_drp*) for no reaction is set. At the end of the droop control part is applied the control ratio.

Table 3.4: The specific control parameters.

Parameter	Value
LPF_d*	$\frac{K_{ESS}}{T_{ESS}s+1}$
Sat_der	(-1;1)
G_der	5000
DZ_der	(-50;50)
f_ref	50
G_drp	10000
Sat_drp	(-5000;5000)
DZ_drp	(-50;50)
LPF_c	$\frac{1}{0.05s+1}$

At this point, the power demand from both control types is provided and summed. By dividing with the terminal voltage, the demanded current is obtained and further filtered (*LPF_c)* due to possible occurring voltage spikes. The control parameters are specifically set for the parameterized battery model. Their values are summarized in Table 3.4.

3.2.4.2 Recharging and safety control

The control for recharging and safety has been developed in a similar manner for both of them. The only difference is, that for the recharging part, the observing signal is the SOC and for the safety part it is the voltage of the single cell (V$_{Bat_Cell}$). The boundary for activating recharging part is totally empty (SOC = 0 %) and totally full (SOC = 100 %) battery. For the safety part, the boundary is set according to the technical specification [54] (V$_{Bat_Cell}$ = 2.0 V for lower and V$_{Bat_Cell}$ = 4.0 V for upper). After achieving one of these boundaries, the recharging process begins. In the case of SOC = 0 % or V$_{Bat_Cell}$ = 2.0 V, the battery starts to charge by the current of 10 A (4C). In the opposite case of SOC = 100 % or V$_{Bat_Cell}$ = 4.0 V, the battery starts to discharge by the current of 12.5 A (5C). The target value for the re-establishing process is called SOC set-point and originally it is set as SOC = 50 %. When the re-establishing process is closing to the SOC set-point ($t_{req} \leq 1\ s$), charging or discharging current is lowered to the value I_{rech} according to following equations:

$$Q = \frac{\left|(SOC_{set-point}) - SOC\right|}{100} Ah_{cap} \times 3600 \qquad [C] \tag{3.48}$$

$$t_{req} = \left\lceil \frac{Q}{I_m} \right\rceil \qquad [s] \tag{3.49}$$

$$I_{rech} = \frac{Q}{t_{req}} \qquad [A] \tag{3.50}$$

Where,

Q = Charge [C]
$SOC_{set-point}$ = The target value of the SOC for the recharging process [%]
Ah_{cap} = Nominal capacity of the battery [Ah]
t_{req} = Requested time for recharging the battery [t]
I_m = Recharging current, charging - 10 A (4C), discharging - 15 A (5C)
I_{rech} = Actual recomputed charging or discharging current [A]

During the re-establishing SOC process, the output current from the inertial response control is disabled (set to zero). Further, in the main control section, the current from the inertial response and from the recharging and safety control is summed and limited to the values 10 A for charging (4C) and 12.5 A for discharging (5C). The limitation ensures that the current fullfills the technical specifications. Different values for charging and discharging are set for achieving more similar behavior into both directions of this process. This is due to the battery dynamic, when during discharging the voltage drops, that it requires higher current to reach similar power than it is in the charging case.

This final current signal is multiplied by the terminal voltage and the requested power is sent to the CCU in RTDS. From RTDS, the value of real transferred power by the converter is brought back to the control block. There it is divided by the terminal voltage and the processed current is sent as the input to the battery model.

3.3 RTDS and dSPACE interfacing

3.3.1 Model interface

The interfacing of the whole developed model is shown in Fig. 3.23. The 12-bus system, including generators, wind power plants, loads, transmission lines and the ESS converter with converter control unit (CCU), is run in RTDS. The model of the ESS and its energy management system (EMS) is run in dSPACE Simulator.

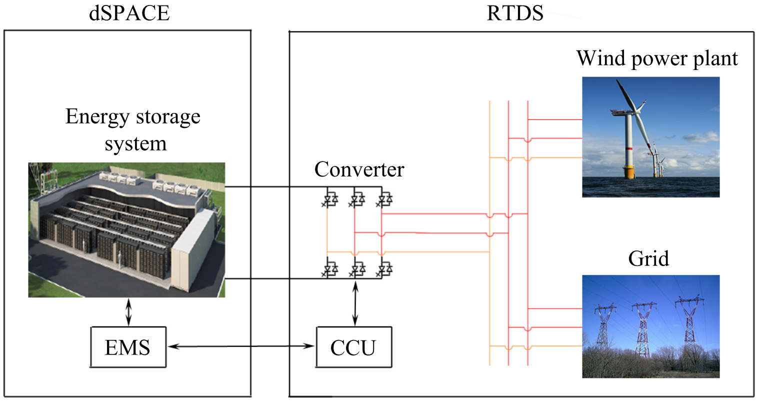

Figure 3.23: Model layout composition.

3.3.2 Hardware interface

Hardware connection of RTDS and dSPACE is done through their digital-analog and analog-digital environment. The interconnection scheme of the complete system is shown in Fig. 3.24. The view of the real workstation is shown in Fig. 3.25. There are six transmitted signals for parameters f, P_r, P_p, V_{Bat}, WPP_{Data} and a trigger signal. The analog communication channel has voltage range ±10 V.

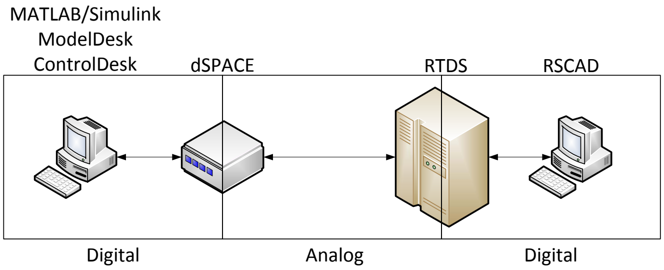

Figure 3.24: Illustration of the laboratory set-up with designation of analog/digital area.

3.3.2.1 dSPACE side

For hardware I/O of dSPACE Simulator there are connected extension modular boards. As a digital-to-analog converter (DAC) DS2103 board is used, as an analog-to-digital converter (ADC) DS2002 board is used. Corresponding DAC/ADC blocks in Simulink® are implemented. In the model, I/O signals of these blocks are in range of value ±1, which matches with ±10 V of the analog channel. The resolution of the ADC is 16 bit and for the DAC it is 14 bit. The routing of the signals with the values for conversion and their attributes in the dSPACE side are shown in Table 3.5.

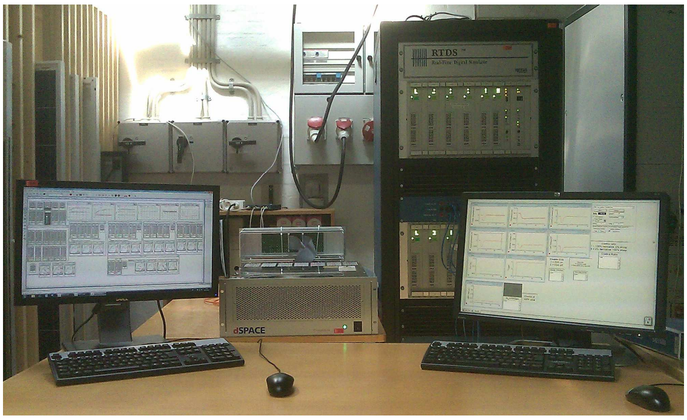

Figure 3.25: The picture of the workstation (RTDS and dSPACE).

Table 3.5: Routing of signals for hardware I/O in dSPACE.

Parameter	Direction	Max range	Offset	Scaling
f	input	45 - 55 Hz	+50	5
P_p	input	±6800 W	-	$-\frac{1}{6800}$
Trigger	input	±10	-	10
P_r	output	±6800 W	-	-6800
V_{Bat}	output	300 - 600 V	-450	$\frac{1}{150}$
WPP_{Data}	output	0 - 1 pu	-0.5	2

3.3.2.2 RTDS side

For the RTDS I/O communication the Gigabit Transceiver Analogue Output Card (GTAO) and the Gigabit Transceiver Analogue Input Card (GTAI) with 16 bit analogue channels of range ±10 V are used. I/O blocks in the model environment are as well available in RTDS, however each of them requires different scaling factor. For the input, the scaling factor represents value of 1 V, for the output, it represents value of 5 V. The values, representing routing of the signals in RTDS, are shown in Table 3.6.

Table 3.6: Routing of signals for hardware I/O in RTDS.

Parameter	Direction	Max range	Offset	Scaling
f	output	45 - 55 Hz	-50	2.5
P_p	output	±6800 W	-	$\frac{3.4}{k}$
Trigger	output	±1	-	0.5
P_r	input	±6.8 MW	-	$k \times 0.68$
V_{Bat}	input	300 - 600 V	+450	15
WPP_{Data}	input	0 - 1 pu	+0.5	$\frac{1}{20}$

4 Study Cases

In order to evaluate the viability of using ESSs to provide inertial response in grids with high wind power penetration, multiple scenarios have been created for the 12-bus system. Scenarios with the increasing level of wind penetration follow trends described in [18]. In the systems with low level of wind penetration (under 20 %), the amount of wind power is increased to supply the growing load demands while the CPPs are intact. In the cases of high wind penetration presented in the grid (over 20 %), load remains constant and the increase of wind power effects into reducing the CPPs.

The generator G2 in the 12-bus system is scaled and divided into two similar units of 320 MVA each. The observing time period is 30 s. In the beginning the system is in steady state. At 2.1 s one of the G2 units (320 MVA generator G2A) is disconnected from the grid to evaluate the intertial response of the system.

The operational metric for evaluating the frequency with consideration of the inertial response is based on the proposed methodology in [18]. The first parameter is the maximal/minimal point of the dynamic frequency deviation. The second parameter is ROCOF, it is df/dt computed in the time period between 2.1 and 2.75 s. The third parameter is the time to reach the first parameter from the beginning of the introduced event. The operational metric is graphically presented in Fig. 4.1. Due to the higher noise in the RTDS measurements, MATLAB smooth function has been applied to the data before processing. For comparison of scenario results in tables, values are rounded to four decimal places.

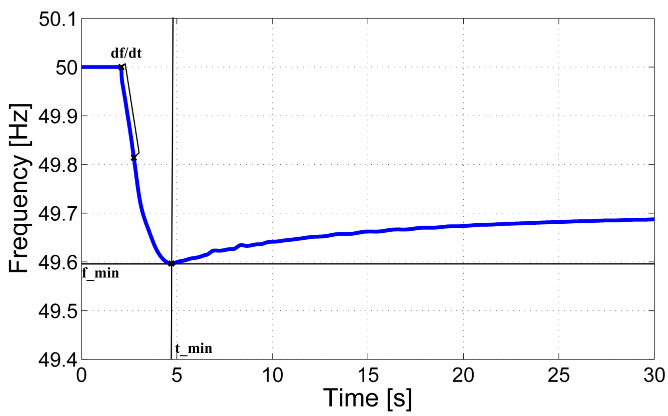

Figure 4.1: Illustration of the used operational metric.

As a part of this project, five study cases have been performed. Their results are presented and discussed in the following sections. The following study cases are performed:

- **Base study case** - provides the basic overview of the system behavior with different wind penetration levels
- **Study case 1** - investigates the effect of the ESS in the grid with different settings of the derivative controller
- **Study case 2** - focuses on the ESS size effect towards the inertial response
- **Study case 3** - evaluates the effect of the ESS with combination of derivative and/or droop control in grid inertia
- **Study case 4** - considers the ESS utilization over a longer time period based on measured WPP data

4.1 Base study case

4.1.1 Case goals

This study case serves as a foundation for further studies. It provides an overview of the 12-bus system behavior with and without wind penetration for the inertial response event. The observed and analyzed quantities are power from generating units (conventional power plant (CPP) and wind power plant (WPP)), power consumption of loads, frequency and voltage at the eight buses. The buses, which are only between generators and their transformers, are not monitored.

4.1.2 Case settings

The base study case contents six scenarios with different settings. Their labels and parameters are shown in Table 4.1. For the BSC1, original 12-bus system is unchanged. For the other scenarios, the 12-bus system is modified and different levels of wind penetration are introduced. BSC2 and BSC3 follow the trend, where by increasing wind penetration, load is increased as well. The total value of increased load is equally spread between the all loads in the 12-bus system. For BSC4 and BSC5, the trend of reducing generator units is considered. In BSC4, the rating of the generator G3 is reduced to 200 MVA from 400 MVA. In BSC5, the generator G3 is permanently disconnected and the generator G4 is reduced to 374 MVA from 474 MVA. BSC6 represents the same wind penetration as BSC5 and its contents. For BSC6, an additional 200 MVAr capacitor C6 for compensation of the reactive power has been introduced at Bus 2.

In Table 4.1, the total inertia constant of the system is represented as H_1. The inertia constant of the system after loss of generator G2A is represented as H_2.

Table 4.1: The setting parameters for the 12-bus system in steady state, including system losses.

Base study case	BSC1	BSC2	BSC3	BSC4	BSC5	BSC6
Wind penetration	0 %	9 %	16 %	24 %	33 %	33 %
CPP [MW]	1478	1473	1468	1265	1060	1059
Load [MW]	1450	1650	1850	1850	1850	1850
WPP [MW]	0	200	400	600	800	800
Total system rating [MVA]	2264	2484	2704	2724	2644	2644
H_1 [MWs/MVA]	8.29	7.56	6.94	6.38	5.80	5.80
H_2 [MWs/MVA]	8.29	7.44	6.76	6.12	5.45	5.45

4.1.3 Case results

In Fig. 4.2 the active power profile for the generation units in BSC1 is shown. One generator unit (320 MVA) of G2 is tripped and the other generators respond according to their characteristics. The tripping of the generator causes temporary oscillations, which are damped and the system reaches slowly to steady state as explained by swing equation.

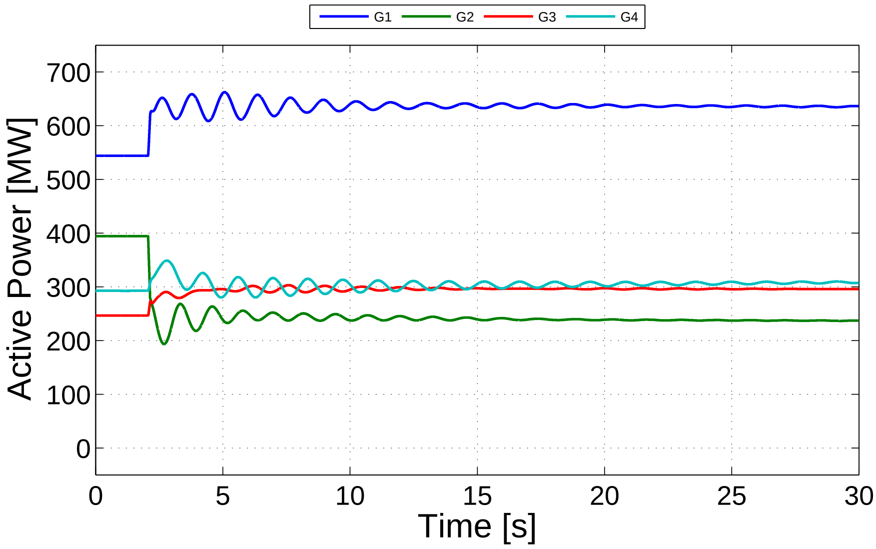

Figure 4.2: Active power profile of the generation units in BSC1.

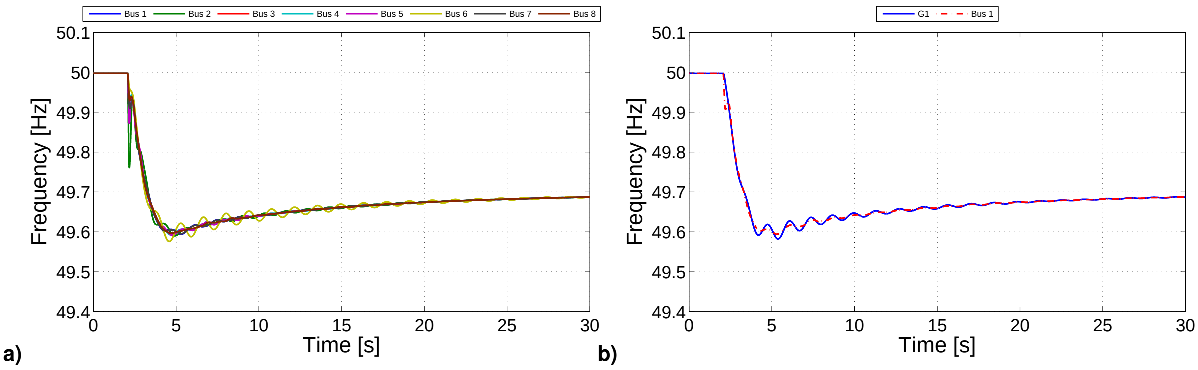

Figure 4.3: a) Frequency profile of eight buses in BSC1 and b) Comparison of the frequency measurements at Bus 1 and the generator G1.

The frequency measurement from Bus 1 is compared in Fig. 4.3 b) to the generator G1 frequency obtained from its speed. The frequency measurements at buses are based on PLL from the voltage. The first negative spike in the bus frequency profile is therefore a measurement error caused by the immediate voltage drop. The frequency obtained directly from the rotation of generators is without this error. Since all the buses are not connected with the rotating machine, PLL has to be used for frequency measurements.

Fig. 4.3 a) shows the frequency of eight observed buses. The frequency at all buses follows the typical trend after the infeed loss. At first, the frequency is falling to its minimum point. This part is dependent on the inertia of the system. The generators react to this change and the before mentioned oscillations appear. The frequency starts to rise and than stabilize at new operating point as determined by the droop control settings of the individual generators.

BSC5 is introduced as the scenario with the highest wind penetration, which represents the scenario with the lowest inertia in the grid. Fig. 4.4 a) and b) illustrate the profiles of generation units for active and reactive power. The infeed loss has the big impact on the reactive power produced by generation units. The results from all base study case scenarios are presented in Appendix C.1.

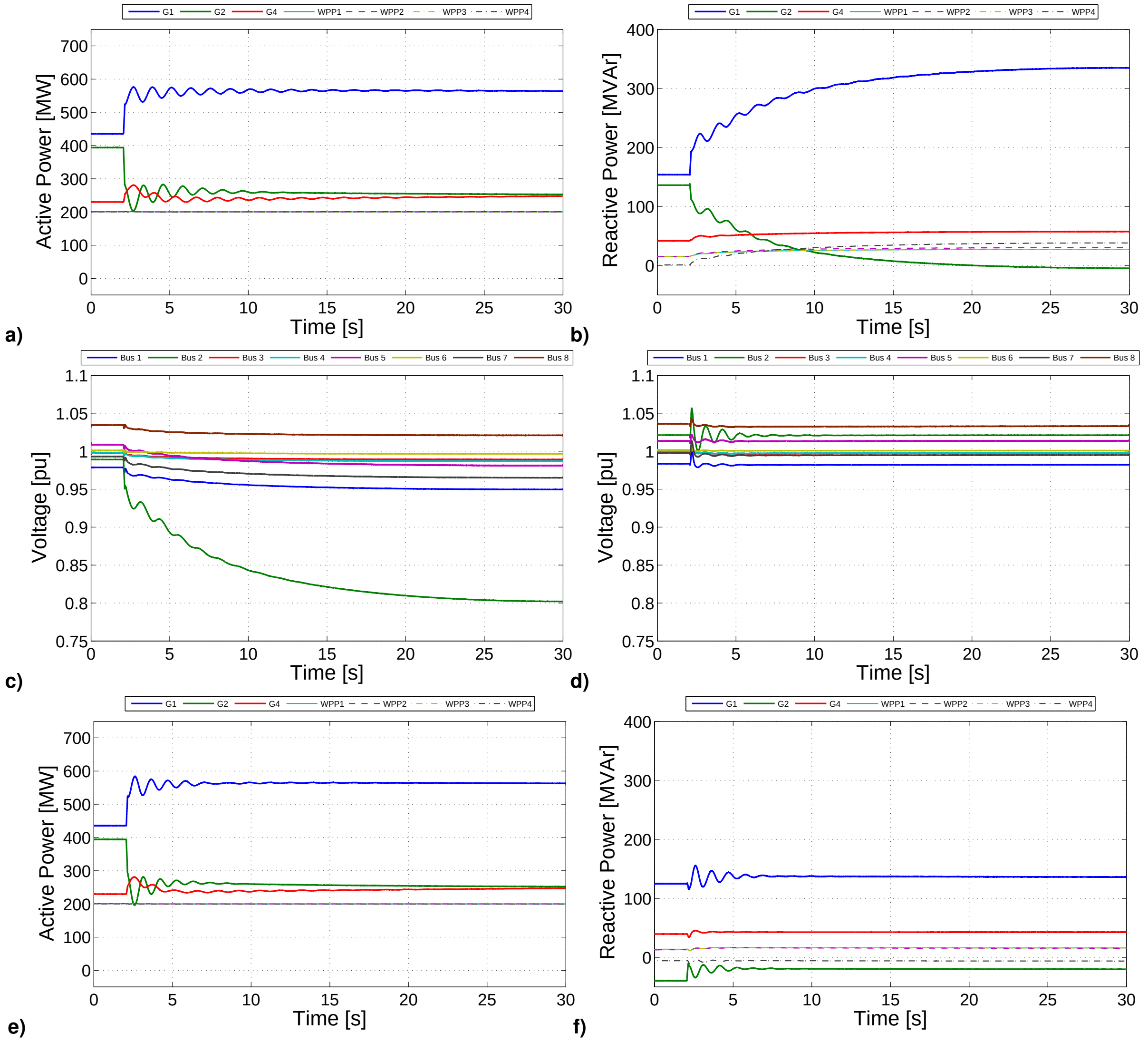

Figure 4.4: a) Active power and b) reactive power profiles of the generation units in BSC5, c) voltage profiles at buses for BSC5, d)voltage profiles at buses for BSC6, e) active power and f) reactive power profiles of the generation units in BSC6.

The voltage drop at Bus 2 is significant due to loss of generation in that bus, as it is shown in Fig. 4.4 c). The reactive power analysis is not the focus of this project, however to minimalize the effect of the voltage outside of the limits, an additional 200 MVAr capacitor C6 has been introduced at Bus 2, to keep voltage in the limits of ±10 %. The voltage profile after adding the capacitor is shown in Fig. 4.4 d).

By this change, the requirements for producing the reactive power has been lowered. It reflects also into the active power generation. The generators have capability to provide more active power and their oscillations have been damped. The active and reactive power generation for BSC6 is shown in Fig. 4.4 e) and f).

For comparison of the frequency profiles of all the base study case scenarios, Bus 3 has been chosen. This is due to the reason that the CPP has been replaced by the WPPs at this bus. Fig. 4.5 shows the comparison of the frequency profiles from all base study case scenarios and the numerical values are presented in Table 4.2. It shows that ROCOF for BSC1 is minimum with the value of 0.26 Hz/s and increases to the maximum value of 0.34 Hz/s in BSC5, where WPP penetration is 33 %. However, the time taken to reach the minimum frequency increases from 4.7 s to 5.8 s when the WPP penetration is increased from 0 % to 33 % respectively. The effect of the increasing wind power penetration, when the system follows trend of the increasing load, is minimal for the inertial response of the grid. In the scenarios, where CPPs have been reduced, the ability of the inertial response has been reduced as well and the frequency drops more.

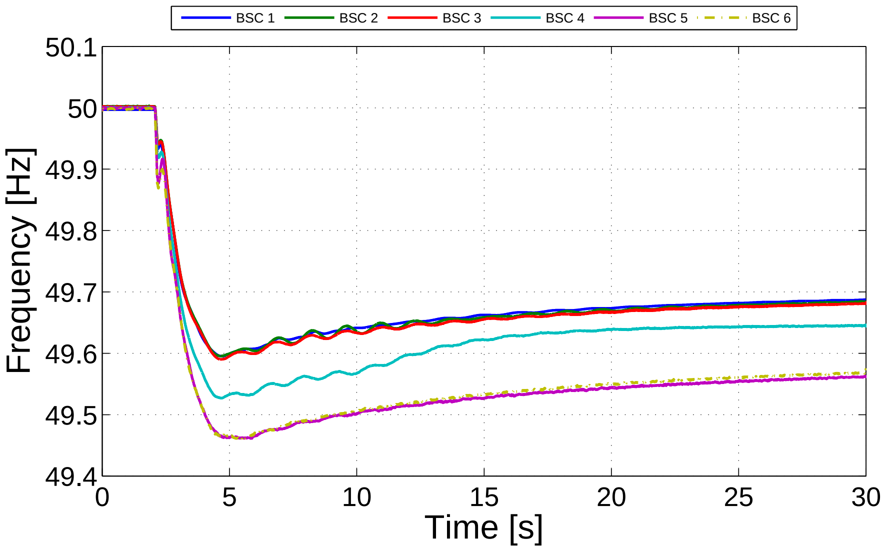

Figure 4.5: Frequency profiles at Bus 3 for all scenarios.

Table 4.2: The results for base study case scenarios.

Base study case	f_{min} [Hz]	df/dt [Hz/s]	t_{min} [s]
BSC1	49.5952	0.2602	4.7032
BSC2	49.5954	0.2712	4.6584
BSC3	49.5900	0.2712	4.7048
BSC4	49.5269	0.3122	4.6816
BSC5	49.4610	0.3422	5.8368
BSC6	49.4588	0.3238	5.4624

4.1.4 Conclusion

Increasing of wind penetration in the grid reduces the total inertia constant. However there are significant differences between trends of increasing load and reducing CPPs. By reducing CPPs the ability of the grid to react against changes decreases. For the following study cases the scenario BSC5 and BSC6 are used as the base. The detailed results and parameters of all scenarios have been presented in Appendix C.1.

4.2 Study case 1

4.2.1 Case goals

The target of study case 1 (SC1) is to evaluate the derivative control for the inertial response of the ESS. The effect of varying the control parameters such as the gain K_{ESS} and the time constant T_{ESS} of derivative control is investigated.

4.2.2 Case settings

SC1 is based on the settings for BSC5. It is further modified by connecting a 10 MW ESS to Bus 3. Values of T_{ESS} are derived from the response of generators. After the infeed loss, time of generators to reach their first response peak has been computed. For G1 and G4 it is approximately 0.6 s and for G2 it is 1.25 s. Therefore, T_{ESS} has been chosen in the way, that the ESS maximal response (considered for settings as 95 % of its nominal power) is reached:

- after all generator units
- between G2 and the group of G1 and G4
- before all generator units
- more than twice faster than previous

The specific values for T_{ESS} and their time to the maximal response are shown in Table 4.3.

Table 4.3: The setting for the time constant T_{ESS}.

Time to 95 % response [s]	1.503	0.903	0.377	0.152
T_{ESS} [-]	0.5	0.3	0.125	0.05

Table 4.4 shows applied values for gain K_{ESS} and corresponding values of df/dt, when the ESS reacts by its nominal power.

Table 4.4: The setting for the gain K_{ESS}.

df/dt for full response [Hz/s]	0.3333	0.2000	0.1429
K_{ESS} [-]	3	5	7

From three options of K_{ESS} and four of T_{ESS}, the scenario matrix has been created. Therefore there are twelve scenarios with unique settings of parameters. This matrix with scenario names is shown in Table 4.5. After evaluating these scenarios, the best one has been picked and performed with the additional 200 MVAr capacitor C6 in Bus 2. In Table 4.5 it is represented by the scenario SC13C.

Table 4.5: The scenario matrix of SC1.

		K_{ESS}		
		3	5	7
T_{ESS}	0.5	SC11	SC12	SC13 / SC13C
	0.3	SC21	SC22	SC23
	0.125	SC31	SC32	SC33
	0.05	SC41	SC42	SC43

4.2.3 Case results

The results for Bus 3 for all scenarios are shown in Table 4.6. Analyzing the values of parameters which are summarized in Table 4.6, it shows that for SC13, the setting of T_{ESS} = 0.5 and K_{ESS} = 7 provides the best results. SC13 has the lowest frequency drop and higher time for reaching its minimum. Therefore the scenario SC13C with the additional capacitor (C6 = 200 MVAr as discussed earlier) has been performed and results were analyzed.

Table 4.6: The results for SC1 scenarios.

Study case 1	f_{min} [Hz]	df/dt [Hz/s]	t_{min} [s]
SC11	49.4664	0.3177	5.7464
SC12	49.4706	0.3141	5.9832
SC13	49.4729	0.3201	5.9496
SC13C	49.4764	0.3086	5.4640
SC21	49.4649	0.3183	5.8312
SC22	49.4674	0.3208	5.7856
SC23	49.4697	0.3163	5.7648
SC31	49.4639	0.3259	5.8240
SC32	49.4669	0.3211	5.7776
SC33	49.4665	0.3275	5.8416
SC41	49.4636	0.3234	5.8096
SC42	49.4649	0.3325	5.8904
SC43	49.4647	0.3240	5.9992

Plots of results for scenarios with T_{ESS} = 0.5 and/or with K_{ESS} = 7 are shown in Fig. 4.6. SC11, SC12 and SC13 shows the effect of varying the values of K_{ESS}. The higher gain is related with providing more power and energy. It is limited by the discharging capability of the batteries, therefore gain higher than 7 would bring only limited increment of the energy.

The scenarios SC13, SC23, SC33 and SC43 have different values for the T_{ESS} parameter. In the observed scenarios, higher time constants effect to more robust control system against the measurement error and oscillations in the system. Scenarios with the higher time constants have been capable to provide more energy to the grid, while ROCOF has been reducing.

Profiles of the single cell voltage and current for the different SC1 scenarios are show in Fig. 4.6 d) and f). The battery dynamic is noticeable on the voltage profile, however its influence on the power output is not significant, because the change of voltage is around 0.3 %.

The time duration of the inertia event is usually in order of seconds. Therefore the total usage of the battery is considered as very small (around 0.3 % of the SOC for the scenario SC13).

Fig. 4.6 shows that SC13 has provided the most energy and caused the lowest frequency drop. Its settings are the highest introduced gain and time constant of the derivative control.

For illustration of the power relations between the energy management system (EMS) of the ESS and converter control unit (CCU), Fig. 4.7 is presented. The EMS of the ESS computes the requested power and sends it to the CCU. Finally the power transfer by the ESS converter has delay with respect to power requested as computed from the EMS, due to use of filter for measuring the power transferred by the ESS converter, which is used as feedback to the EMS.

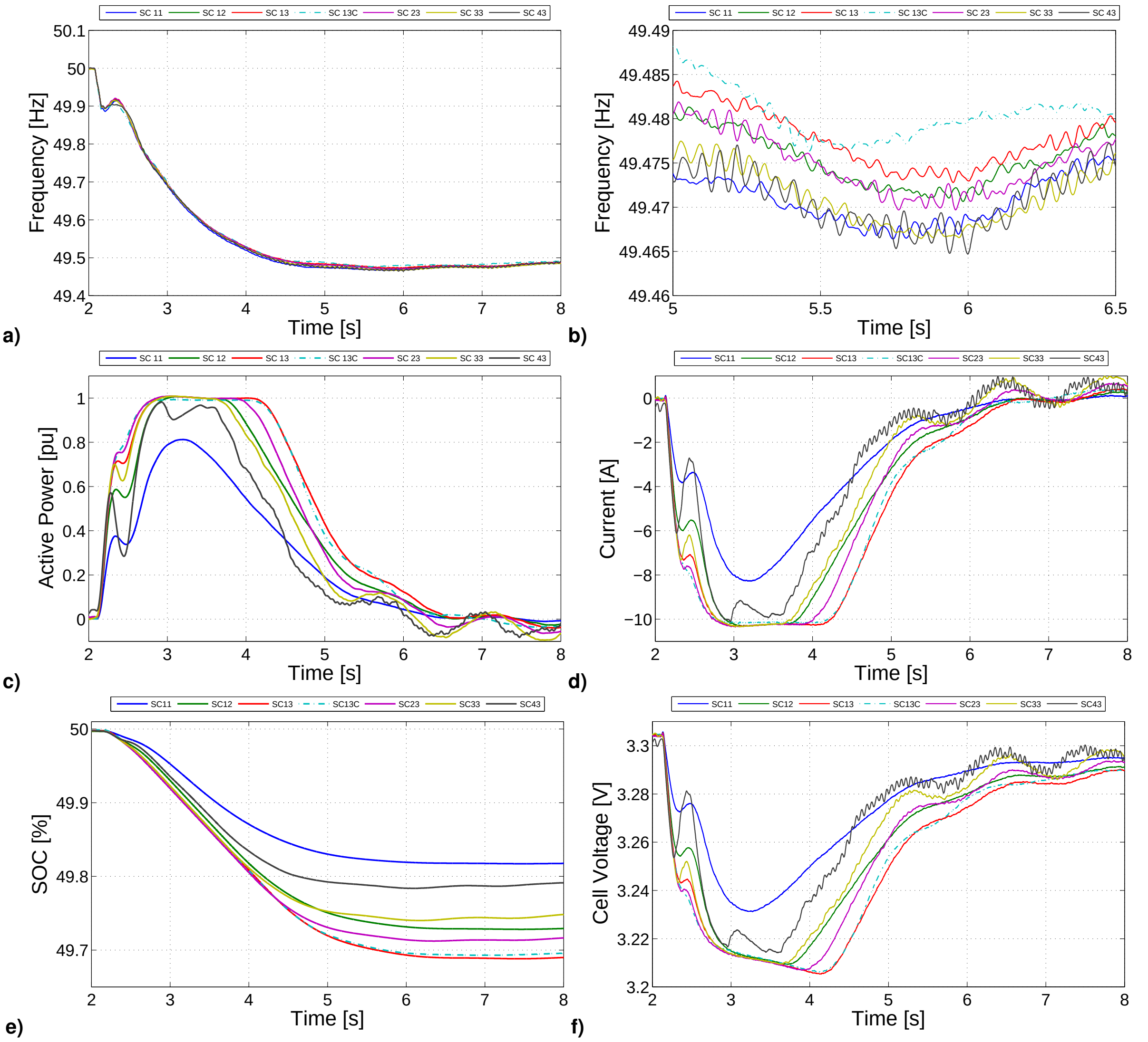

Figure 4.6: Results of SC1: a) frequency, b) detail of the frequency minimal point, c) the ESS power, d) the single cell current, e) SOC of the ESS and f) the single cell voltage.

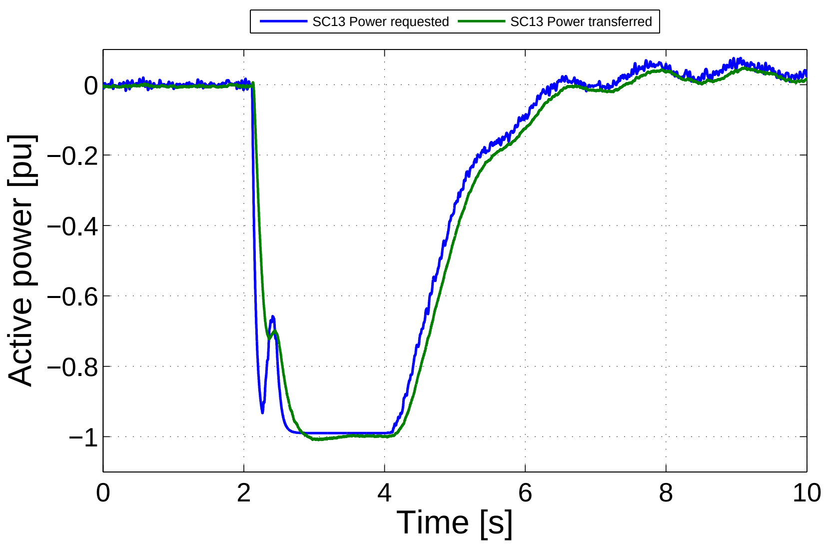

Figure 4.7: Power requested (computed) by the EMS compared to the power transferred by the ESS converter.

4.2.4 Conclusion

In SC1, the effects of the time constant and gain in derivative control for the inertial response have been studied. Specific T_{ESS} values have been selected based on the generators response and values of K_{ESS} has been chosen based on ROCOF with relation to the ESS nominal power. By analyzing different scenarios, the derivative control with a time constant T_{ESS} = 0.5 and a gain K_{ESS} = 7 has provided the best inertial response. Consequently this values were used for the following study cases. The detailed results and parameters of scenarios SC13 and SC13C have been presented in Appendix C.2.

4.3 Study case 2

4.3.1 Case goals

In this study case (SC2), the effect of ESS different sizes (nominal power) is observed and evaluated.

4.3.2 Case settings

Settings for SC2 are based on the scenario SC13 from SC1. The ESS is connected to Bus 3 and the derivative control parameters are K_{ESS} = 7, T_{ESS} = 0.5. Scenarios, with their names and corresponding sizes of the ESS, are listed in Table 4.7. The scenario SC2_6C has been performed with the additional 200 MVAr capacitor C6.

Table 4.7: Scenarios for SC2.

Scenario	ESS nominal power [MW]
SC2_1	2.5
SC2_2	5.0
SC2_3	7.5
SC2_4	10.0
SC2_5	12.5
SC2_6 / SC2_6C	15.0
SC2_7	20.0
SC2_8	25.0

4.3.3 Case results

Fig. 4.8 illustrates Table 4.8. It can be observed that, the lowest point of frequency drop is improved with the increasing size of the ESS and has nearly linear trend. The time to reaching the minimal frequency point is rapidly increased in the step from 12.5 MW to 15 MW. Therefore SC2_6 (15 MW) has been chosen as a base for further study. The numerical values of these results are presented in Table 4.8.

Profiles of the frequency, ESS power and SOC are presented in Fig. 4.9, in the time period from 2 to 8 s. The frequency curve shape is changed with the different ESS size. With increased size of the ESS, the valley with the frequency minimal point is more straightening up. In scenarios with the lower size of the ESS, the ROCOF is higher, therefore the ESS has to provide more percentage of its energy. As derivative control provides energy from the ESS only for the short period (during the frequency drop), there is not significant change in the SOC in the ESS as seen in Fig. 4.9. It is due to the limitation of the charging/discharging current of Li-ion batteries as describeg in section 3.2.4.2 Recharging and safety control.

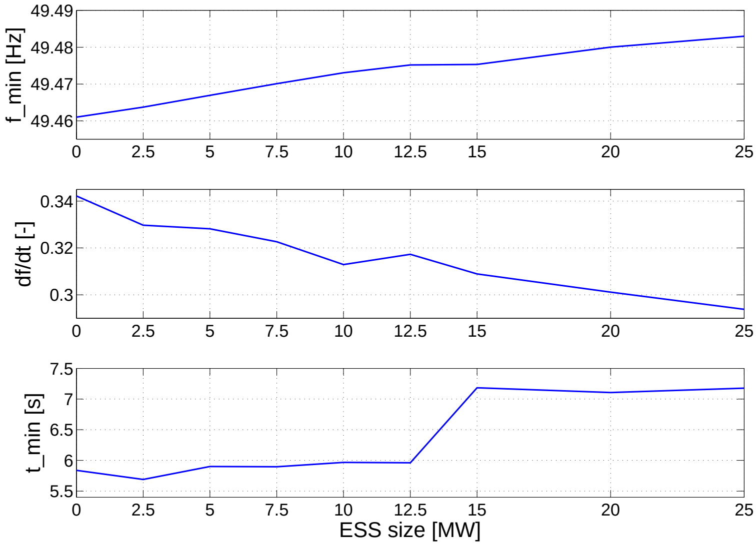

Figure 4.8: Evaluating of scenarios - different sizes.

Table 4.8: The results for SC2 scenarios.

Study case 2	f_{min} [Hz]	df/dt [Hz/s]	t_{min} [s]
SC2_1	49.4637	0.3297	5.6904
SC2_2	49.4669	0.3282	5.9000
SC2_3	49.4701	0.3226	5.8960
SC2_4	49.4731	0.3129	5.9664
SC2_5	49.4752	0.3173	5.9616
SC2_6	49.4753	0.3089	7.1832
SC2_6C	49.4826	0.3027	6.6768
SC2_7	49.4800	0.3011	7.1056
SC2_8	49.4830	0.2938	7.1768

4.3.4 Conclusion

The effect of the ESS size towards the inertial response has been studied. The increased ESS size improves the inertial response, however optimisation on the appropriate size has not been considered. From these scenarios, the ESS size for further studies has been selected as 15 MW. The detailed results and parameters of scenarios SC2_6 and SC2_6C have been presented in Appendix C.3.

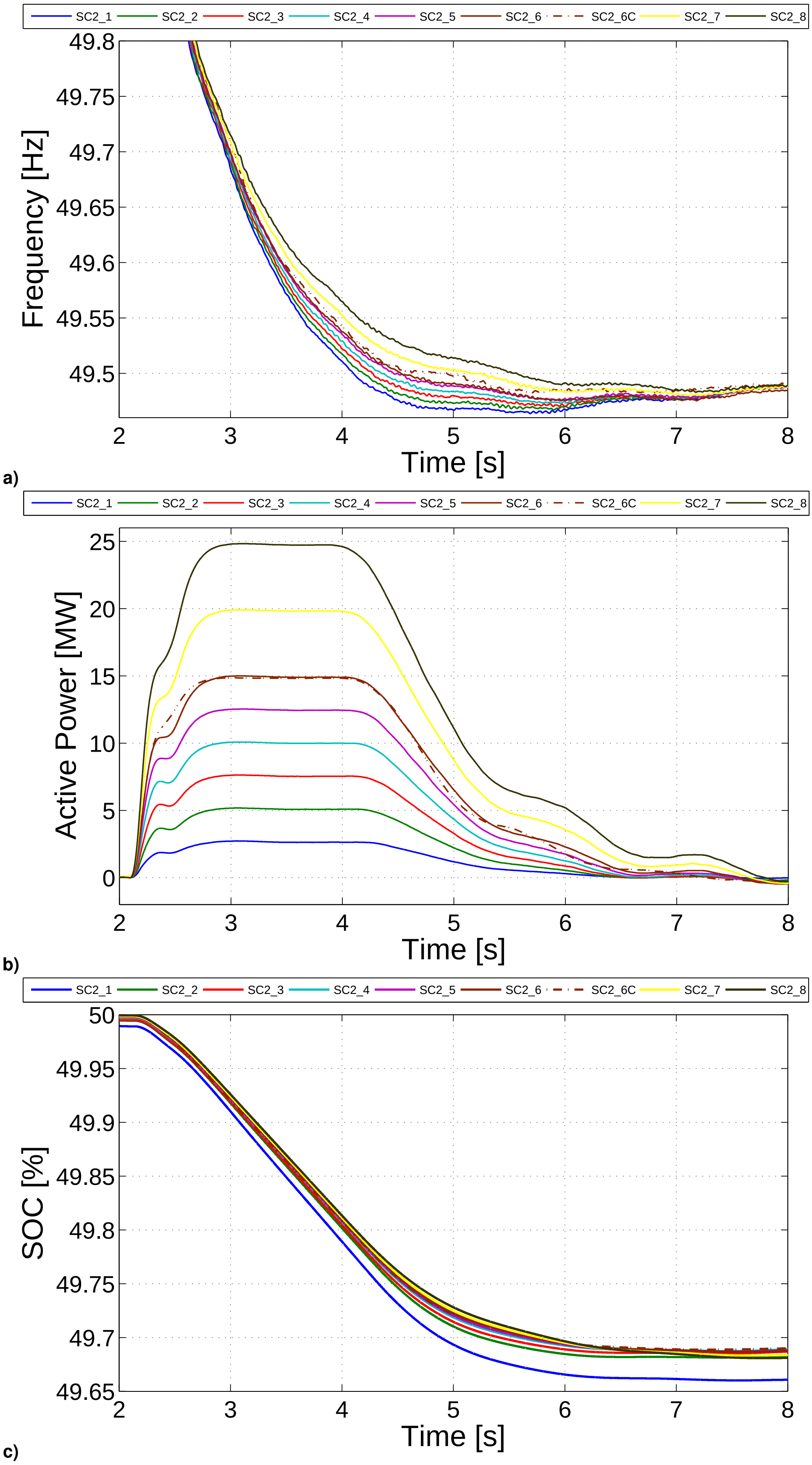

Figure 4.9: Results of SC2: a) frequency, b) the ESS power and c) SOC of the ESS.

4.4 Study case 3

4.4.1 Case goals

The goal of study case 3 (SC3) is to evaluate influence of derivative, droop control and their combination for providing the inertial response in order to estimate which control strategy is better.

4.4.2 Case settings

The ESS size is 15 MW and it is connected to Bus 3. The control parameters for derivative control are based on SC13, K_{ESS} = 7 and T_{ESS} = 0.5. Droop control parameter G_drp is set as 10000, which represents full power provided by the ESS at frequency of 49.5 Hz (50 Hz is set as reference). Modeling of both control strategies are described in section 3.2.4.1. Scenarios and their settings of the control ratio is shown in Table 4.9. Control ratio = 1 represents only derivative control, control ratio = 0 represents only droop control. Scenario SC3_4C is performed with the additional 200 MVAr capacitor C6.

Table 4.9: Scenarios for SC3.

Scenario	Control ratio
SC3_1	1
SC3_2	0.75
SC3_3	0.5
SC3_4 / SC3_4C	0.25
SC3_5	0

4.4.3 Case results

Graphically interpreted results for scenarios with different control ratio are presented in Fig. 4.10. The numerical results are summarized in Table 4.10. It shows that derivative control helps in reducing ROCOF, whereas droop control improves minimum frequency. However, it is worth mentioning that with derivative control the time of reaching minimum frequency is longer than with droop control. Hence, the mixture of derivative and droop control compromises between the minimum frequency and ROCOF.

Table 4.10: The results for SC3 scenarios.

Study case 2	f_{min} [Hz]	df/dt [Hz/s]	t_{min} [s]
SC3_1	49.4782	0.3539	5.8768
SC3_2	49.4839	0.3544	6.0264
SC3_3	49.4896	0.3580	5.7664
SC3_4	49.4952	0.3603	5.7288
SC3_4C	49.4950	0.3625	5.4744
SC3_5	49.4927	0.3756	4.8936

Fig. 4.11 shows scenario comparison of the frequency, ESS power and SOC. Based on the power response from the ESS, according to the different control ratio values, the response time

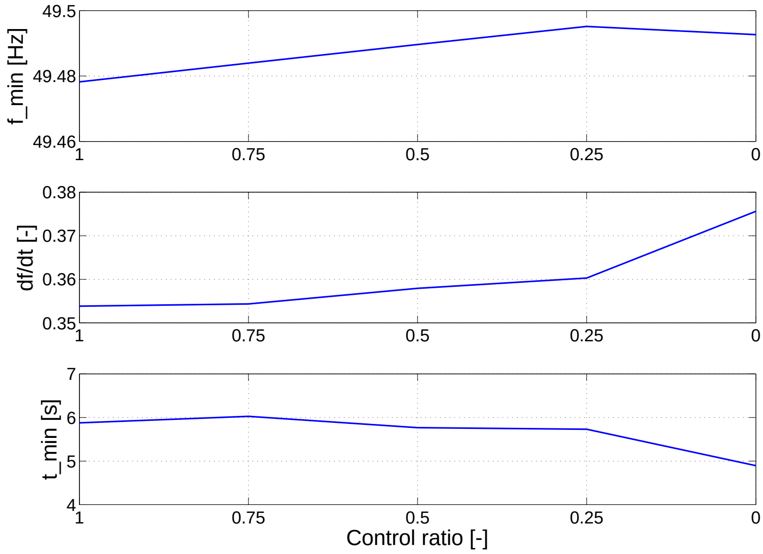

Figure 4.10: Evaluating of scenarios - different sizes.

period is divided into two stages. The first stage is influenced mainly by the derivative control and it is in time from 2.1 to 4.3 s. In the second stage the droop control is dominant and it is from 4.3 s further. In the tested scenarios, the best result has been provided by SC3_4 with the control ratio of 0.25, it has offered the best compromise between the controls. For derivative control the SOC decreases more rapidly than droop control, but it settles down at the steady state value unlike in case of droop control. This is due to derivative control does not provide any energy from the ESS when the frequency is stable, whereas for droop control it continues providing energy from the ESS based on its droop ratio. The results for scenarios SC3_4 and SC3_4C are presented in Appendix C.4.

4.4.4 Conclusion

The results show that not only the amount of released energy influences the frequency drop, but also very important is the time frame. Therefore the improved proposed control would be the dynamic derivative-droop control, where the first response, the ESS output, would completely depend on the derivative control. At the point when the droop control would provide more power than derivative control, the control ratio would be changed from 1 to 0, which implies that control system changes from derivative control to droop control.

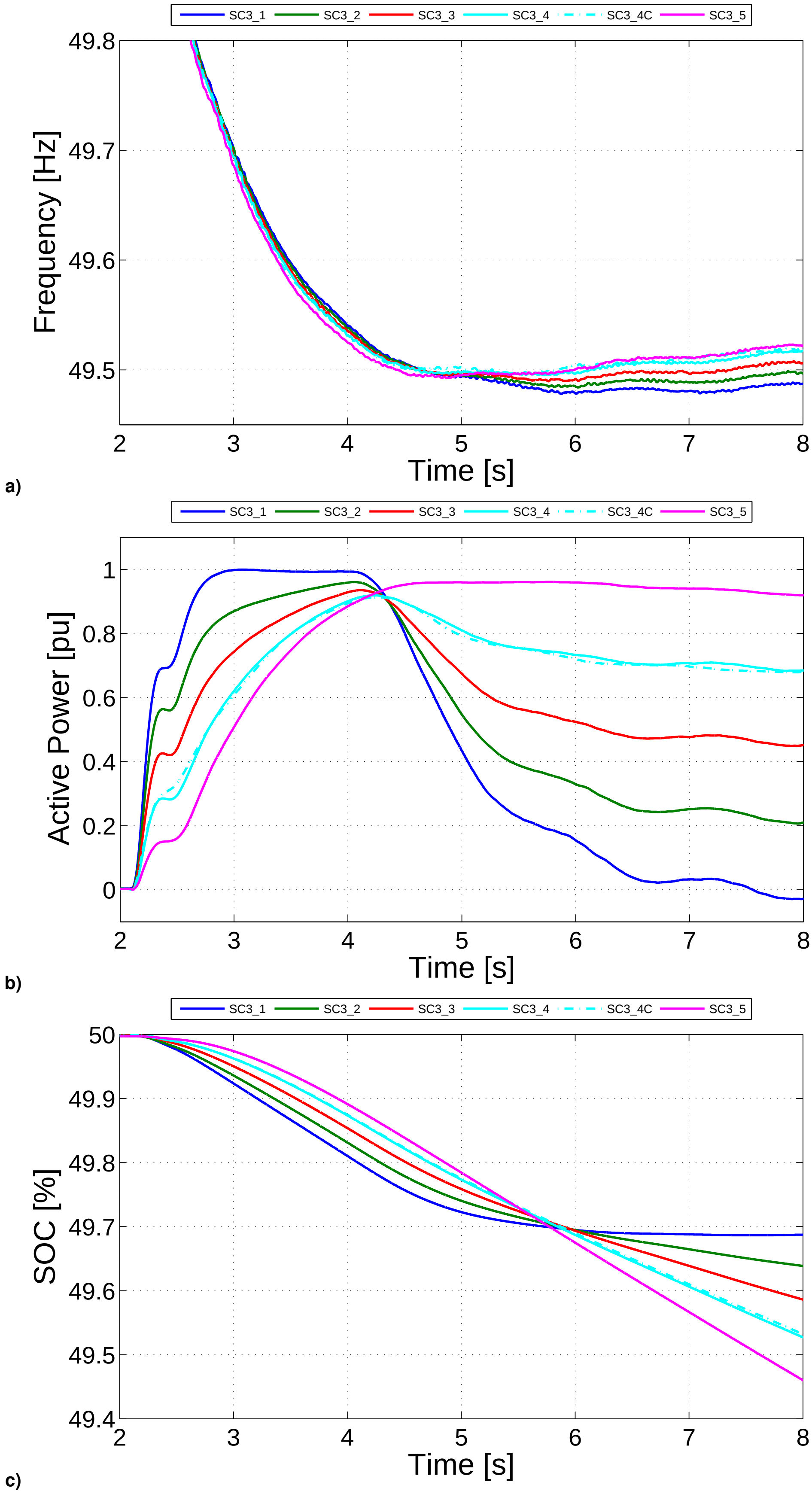

Figure 4.11: Results of SC3: a) frequency, b) the ESS power and c) SOC of the ESS.

4.5 Study case 4

4.5.1 Case goals

The goal of study case 4 (SC4) is to evaluate the influence of change in wind power to the grid frequency. Further, it is to investigate the effect of the inertial response from the ESS.

4.5.2 Case settings

The actual measured data for power production from 2 MW wind turbine has been scaled up to 200 MW and fed into Bus 3 using two wind turbines WPP1 and WPP3, 200 MW each, as shows in Fig. 3.1.

The ESS size and control parameters are based on the results from study case(SC) 1 and 2. The size of the ESS is selected to be 15 MW and it is connected to Bus 3. Control parameters for derivative control are based on SC13 where, K_{ESS} = 7 and T_{ESS} = 0.5. All other parameters of the generators and loads are the same as that of base study case 6 (BSC6). The frequency of the system was balanced at 50 Hz when WPP1 and WPP3 are producing 150 MW each and WPP2 and WPP3 are producing 200 MW each through the simulation.

The original measured data from 2 MW wind turbine had a resolution of 10 minutes. This data has been downscaled to 30 s resolution as shown in Fig. 4.12. Hence the wind power profile of 5 hours has been reduced and simulated in 15 minutes. With this modification, this study case has a limitation that the system doesn't account for secondary frequency response. However, the real time simulation gives some clear idea about the variation of frequency with varying nature of wind power in real life. The power variation from wind turbine is not instantaneous as shown in Fig. 4.12. The demo model in MATLAB for "Wind Farm - Synchronous Generator and Full Scale Converter (Type 4) Detailed Model" has been observed to determine the dynamics of wind turbine. It has been observed that during the rise time of the power production, when wind speed changes from 0 m/s to its rated value of 12 m/s, the model takes 4.5 s to reach 90% of its rated power production. Similarly, when the wind speed drops from 12-0 m/s, the reduction in 90% of power production takes 3.5 s. Thus the measured original data has been modified by using the low pass filter so that the 90% of rise time and fall time is 4.5 s and 3.5s respectively as shown in Fig. 4.12.

Two cases are studied, with and without the ESS as it is shown in Table 4.11.

Table 4.11: Scenarios for SC4.

Scenario	
SC4_1	Without ESS
SC4_2	With ESS

4.5.3 Case results

Fig. 4.13 shows active power production from the generation units (SC4_2) and comparison of the grid frequency with and without the ESS. The variation in WPP power influences the grid

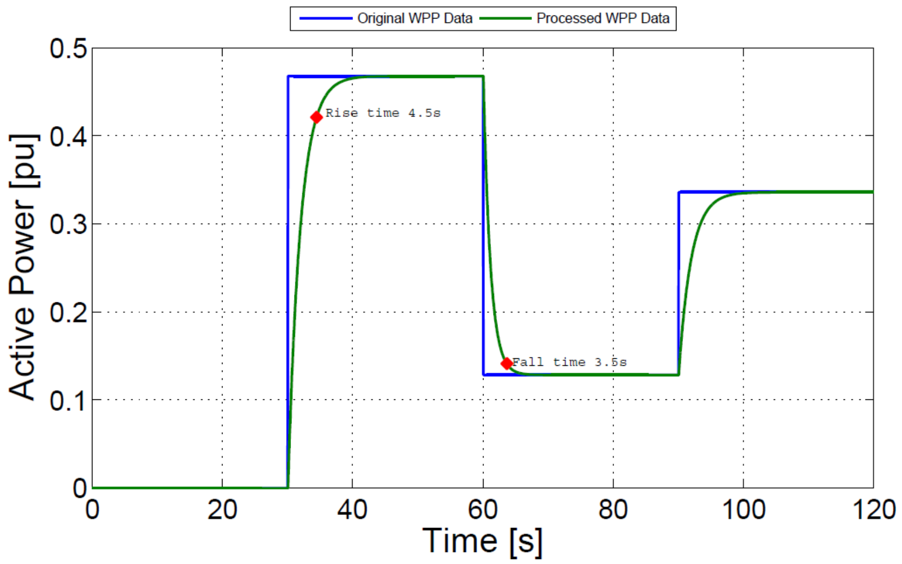

Figure 4.12: Wind turbine power production data in pu, measured and processed.

frequency and it is shown in Fig. 4.13 b. There are no significant differences in frequency profile with the implementation of the ESS with derivative control only as it only provides energy for the inertial response and does not support directly in primary frequency response as seen from study cases 1. The effect of the ESS can be seen in improving the inertial response as shown in Fig. 4.13 c.

4.5.4 Conclusion

The power variation from the wind turbines causes frequency deviations. The ESS improves the inertial response of the grid, however due to its control parameters designed for the instantaneous infeed loss, the ESS has not provided the adequate response. The use of combination of derivative and droop control in the ESS may help to improve inertial response as well as support the primary frequency regulation. However, due to limitations and the aim of this project in order to investigate the intertial response only, no further studies has been made for the primary frequency regulation provided from the ESS.

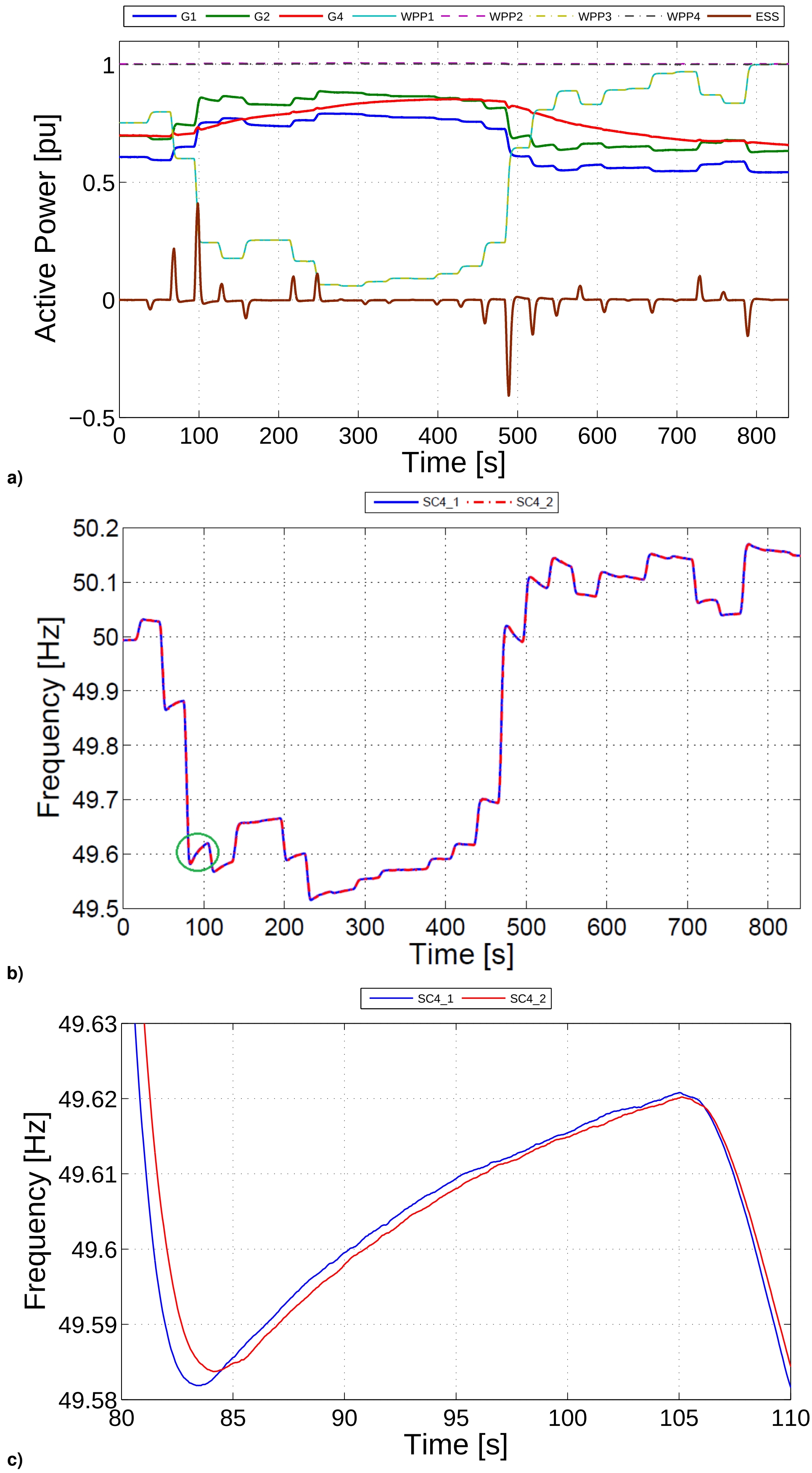

Figure 4.13: a) Active power from the generation units and the ESS, b) frequency at Bus 3 and c) detail in frequency at Bus 3.

5 Conclusions and future work

Nowadays, with the trend of increasing the amount of renewable energy sources in electrical power generation, new challenges are introduced. One effect of this is in the lowering inertia in the grid, which causes higher and faster frequency drop during the power unbalance. Grid intergration of ESSs has been identify as a possible solution for reducing the aforementioned issues since they are able to provide inertial response to the grid. Therefore, the task of this project has been to investigate the feasibility of integrating the ESSs based on Lithium-ion batteries for providing inertial response into the grid.

For a deeper insight into the problematic, a literature review has been performed. Rotating machine inertia is described to provide basic understanding of relation between generators and the changes in the grid frequency. This is followed by a section dedicated to the wind power plants, as they represent a specific group of power plants, where their generators are not always directly coupled with the grid frequency and they are not able to provide inertia response by default. Furthermore, the grid frequency responses to disturbance are elaborated. The overview of the different ESS technologies is as well provided and various aspects of Lithium-ion batteries, as they are focus of this project, are explained.

Real Time Digital Simulator and RSCAD have been used to implement the 12-bus system model, the wind power plant model and the ESS converter model. The 12-bus system has been modifed to versions representing different wind power penetration of the system. The energy storage system, including model of Lithium-ion batteries and control in form of energy management system, has been modeled and implemented in MATLAB/Simulink; the dSPACE battery simulator has been used for real time simulation of the ESS. By interfacing these two real time simulating platforms, the experimental setup and configuration has been created and prepared.

In total, five different study cases have been performed. In the base study case it has been verified that by increasing wind penetration in the system and reducing the number of CPPS, the inertia in the grid is reduced. The scenario with the highest wind penetration has been further used in the other study cases.

Study case 1 focuses on different settings of the inertial derivative control. From the observed control settings, the control with parameter of time constant T_{ESS} = 0.5 and gain K_{ESS} = 7 provides the best results.

The influence of the ESS size on the inertial response has been investigated in study case 2. The relation of the increasing ESS size and the rising minimum point of the frequency during the drop has been found approximately linear. Similarly, a decreasing trend of ROCOF with increasing the ESS size has been observed. As the power through scenarios has grown significantly, the trend of changing characteristic shape of the frequency drop profile has been observed. The ESS size of 15 MW has been evaluated as the most beneficial due to significant increment of the time period to reach the minimal point of the frequency and therefore it has been used for further study cases.

In study case 3, the effects of the inertial derivative and droop control and their combination have been studied. Two stages of the inertial response have been indentified according to two applied control strategies. By comparison the results, it shows that derivative control influences more ROCOF and it is active in the first stage and by that the time to the minimal point of the frequency. The droop control influences more the final minimal point of the frequency. From results it is visible that not only the amount of energy, but also the time frame of the ESS response influences the frequency drop.

Fig. 5.1 shows the summary of frequency profile of Bus 3 and its comparison with different study cases. It is clearly seen that with the reduction in grid inertia due to increment of WPPs and reduction of CPPs, there is increment in ROCOF and the point of minimum frequency is decreased as seen from curves of BSC1, BSC4 and BSC6. By utilization the 10 MW ESS with derivative control in SC13C, the response to grid inertia has been noticeable improved. By increasing the ESS size from 10 MW to 15 MW in SC2_6C, the another improvement of the frequency drop has been achieved, however it has caused smaller effect in this step with comparing the change between BSC6 and SC13C. By applying control of derivative and droop combination with control ratio of 0.25 (25 % derivative and 75 % droop) in SC3_4C, the inertial response has been further improved, together with the result of stabilization the grid frequency at the higher point during the steady state.

Study case 4 investigates the power variation influence caused by variations on the wind turbine production, thus the cause of the frequency drop has different character than at previous cases. Result shows that the ESS improves the inertial response in the grid; however, its control is not sufficiently tuned for the effective utilization of the ESS power capability. Therefore for the optimal application, it is necessary to identified characteristics of the desired events for response.

The grid integration of ESSs based on Lithium-ion batteries has been evaluated in this project for providing the inertial response. It shows that the ESS is an complex system with variable parameters, which affect the final form of the ESS utilization. By a proper selection of these parameters, the ESS effect can be improved and consequently the ESS would become a very beneficial element of the grid in terms of inertial response.

For future work, it is necessary to investigate parameters of derivative and droop control, including the size of ESSs by optimalization process. For improving the inertial control, derivative and droop control should be dynamicly combined to beneficiate from the advantages of both. As results have shown, the ESS energy usage (SOC) is very low, due to short time period of applying the service and the power limitations of the Lithium-ion batteries. By assuming that significant frequency deviations are not so often, more effective usage of the ESSs should be considered, for example by providing several service; inertial response and primary frequency regulation.

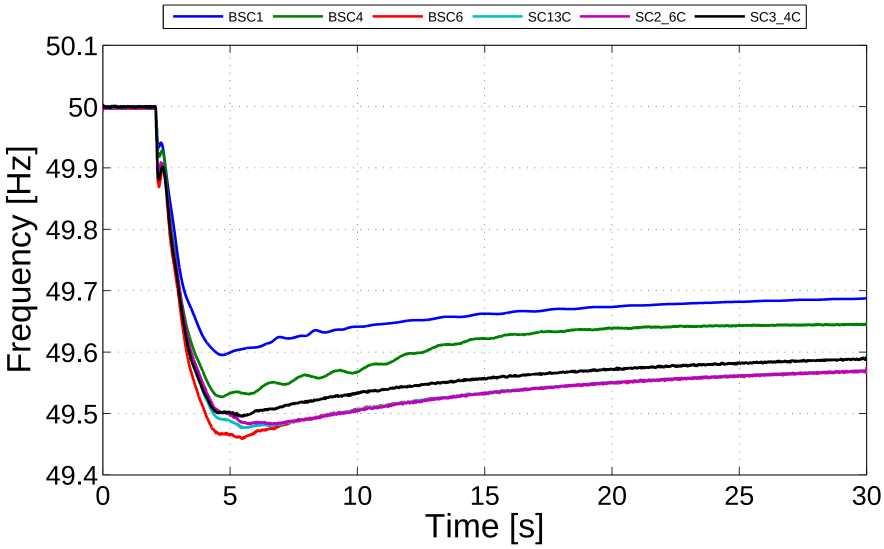

Figure 5.1: Summary of frequency profiles for different study cases
BSC1 - 0 % WPP penetration
BSC4 - 24 % WPP penetration
BSC6 - 33 % WPP penetration, with C6
SC13C - 33 % WPP penetration, 10 MW ESS, derivative control with T_{ESS} = 0.5 and K_{ESS} = 7, with C6
SC2_6C - 33 % WPP penetration, 15 MW ESS, derivative control with T_{ESS} = 0.5 and K_{ESS} = 7, with C6
SC3_4C - 33 % WPP penetration, 15 MW ESS, combination of derivative and droop control, T_{ESS} = 0.5 and K_{ESS} = 7, control ratio = 0.25, with C6.

6 Bibliography

[1] "IEA Energy Statistics." [online], 2013. Available: `http://www.iea.org/stats/index.asp` (Accessed: 20 February 2013).

[2] "Large Scale Integration of Wind Energy in the European Power Supply: analysis, issues and recommendations," report, EWEA, December 2005. The European Wind Energy Association.

[3] "Directive 2009/28/EC of the European Parliament and of the Council of 23 April 2009 on the promotion of the use of energy from renewable sources and amending and subsequently repealing Directives 2001/77/EC and 2003/30/EC (Text with EEA relevance)." Directive, April 2009. European Parliament, Council.

[4] "Energy policy report 2012," May 2012. Ministry of Climate, Energy and Building, Denmark.

[5] P. Kundur, N. Balu, and M. Lauby, *Power System Stability and Control*. The Epri Power System Engineering, McGraw-Hill Education, 1994.

[6] P. W. Christensen and G. C. Tarnowski, "Inertia for Wind Power Plants - state of the art review - year 2011," (Aarhus, Denmark), 10th International Workshop on Large-Scale Integration of Wind Power into Power Systems,, November 2011.

[7] P. Tielens and D. V. Hertem, "Grid Inertia and Frequency Control in Power Systems with High Penetration of Renewables," in *Young Researchers Symposium in Electrical Power Engineering*, vol. 6, (Delft, The Netherlands), April 2012.

[8] A. Causebrook, D. Atkinson, and A. Jack, "Fault Ride-Through of Large Wind Farms Using Series Dynamic Braking Resistors (March 2007)," *Power Systems, IEEE Transactions on*, vol. 22, no. 3, pp. 966–975, 2007.

[9] X. Yingcheng and T. Nengling, "System frequency regulation investigation in doubly fed induction generator (DFIG)," *WSEAS Ttransaction on Power Systems*, vol. 7, January 2012.

[10] A. Adamczyk, M. Altin, Ö. Göksu, R. Teodorescu, and F. Iov, *Generic 12-Bus Test System for Wind Power Integration Studies*. EPE Association, 2012.

[11] J. Enslin, "Interconnection of distributed power to the distribution network," in *Power Systems Conference and Exposition, 2004. IEEE PES*, pp. 726 – 731 vol.2, oct. 2004.

[12] I. J. Nagrath and D. P. Kothari, *Power System Engineering*. Tata *McGraw-Hill Oublishing Company Limited, 10 ed., 2001. ISBN = 0-07-462299-4.

[13] J. Zhu, C. Booth, G. Adam, and A. Roscoe, “Inertia emulation control of VSC-HVDC transmission system,” in *Advanced Power System Automation and Protection (APAP), 2011 International Conference on*, vol. 1, pp. 1 –6, oct. 2011.

[14] J. Morren, J. Pierik, and S. W. de Haan, “Inertial response of variable speed wind turbines,” *Electric Power Systems Research*, vol. 76, no. 11, pp. 980 – 987, 2006.

[15] J. Aho, A. Buckspan, J. Laks, P. Fleming, Y. Jeong, F. Dunne, M. Churchfield, L. Pao, and K. Johnson, “A tutorial of wind turbine control for supporting grid frequency through active power control,” in *American Control Conference (ACC), 2012*, pp. 3120 –3131, june 2012.

[16] A. Oudalov, D. Chartouni, and C. Ohler, “Optimizing a Battery Energy Storage System for Primary Frequency Control,” *Power Systems, IEEE Transactions on*, vol. 22, no. 3, pp. 1259–1266, Aug.

[17] G. C. Tarnowski, *Coordinated Frequency Control of Wind Turbines in Power Systems with High Wind Power Penetration*. PhD thesis, Technical University of Denmark, November 2011.

[18] M. Altin, R. Teodorescu, B. Jensen, U. Annakkage, F. Iov, and P. Kjær, “Methodology for assessment of inertial response from wind power plants,” in *Power and Energy Society General Meeting, 2012 IEEE*, pp. 1 –8, july 2012.

[19] Y. Dai, T. Zhao, Y. Tian, and L. Gao, “Research on the Primary Frequency Control Characteristics of Generators in Power System,” in *Industrial Electronics and Applications, 2007. ICIEA 2007. 2nd IEEE Conference on*, pp. 569 –574, may 2007.

[20] I. Moore and J. Ekanayake, “Frequency response from wind turbines,” in *Universities Power Engineering Conference (UPEC), 2009 Proceedings of the 44th International*, pp. 1 –5, sept. 2009.

[21] P. Braun, M. Swierczynski, F. Blaabjerg, P. Rodriguez, and R. Teodorescu, *Li-Ion Batteries in a Virtual Power Plant (Energy Storage + Wind Power Plant) for Primary Frequency Regulation*. Energynautics GmbH, 2011.

[22] L. Friedrich and M. Gautschi, “Grid Stabilization Control and Frequency Regulation for Inverter-connected Distributed Renewable Energy Sources,” Master’s thesis, University of Wisconsin-Madison, 1415 Engineering Drive Madison, Wisconsin 53706, September 2009.

[23] M. Torres and L. A. Lopes, “An Optimal Virtual Inertia Controller to Support Frequency Regulation in Autonomous Diesel Power Systems with High Penetration of Renewables,” in *Proc. Int. Conf. Renewable Energy & Power Quality (ICREPQ 11)*, (La Palmas de Gran Canaria, Spain), 2001.

[24] E. Muljadi, V. Gevorgian, M. Singh, and S. Santoso, “Understanding inertial and frequency response of wind power plants,” in *Power Electronics and Machines in Wind Applications (PEMWA), 2012 IEEE*, pp. 1–8, 2012.

[25] H. Polinder, D.-J. Bang, H. Li, and Z. Chen, “Concept Report on Generator Topologies, Mechanical & Electromagnetic Optimization,” tech. rep., Delft University of Technology, Aalborg University,, 2007.

[26] J. Fletcher and J. Yang, *Introduction to the Doubly-Fed Induction Generator for Wind Power Applications, Paths to Sustainable Energy*. InTech, December 2010. ISBN 978-953-307-401-6.

[27] R. T. Derazkolaie, H. A. Shayanfar, and B. Mozafari, "Effects of the Controller Performance of DFIG on its Inertia Response," *Global Journal of Research in Engineering*, vol. 11, April 2011. ISSN: 0975-5861.

[28] S. El Itani, U. Annakkage, and G. Joos, "Short-term frequency support utilizing inertial response of DFIG wind turbines," in *Power and Energy Society General Meeting, 2011 IEEE*, pp. 1–8, 2011.

[29] "Electricity Storage." [online], April 2009. Available: http://www.electricitystorage.org (Accessed: 9 March 2013).

[30] "Electrical Energy Storage." White Paper, December 2011. International Electrotechnical Commission Market Strategy Board.

[31] "The Electropaedia." [online]. Available: `http://www.mpoweruk.com/lithiumS.htm` (Accessed: 10 March 2013).

[32] B. Dunn, H. Kamath, and J.-M. Tarascon, "Electrical Energy Storage for the Grid: A Battery of Choices," *Science*, 2011.

[33] G. L. Soloveichik, "Battery technologies for large-scale stationary energy storage," *Annu Rev Chem Biomol Eng*, vol. 2, pp. 503–27, 2011.

[34] I. Buchmann, "Battery University." [online]. Available: `http://batteryuniversity.com/learn/article/types_of_lithium_ion` (Accessed: 3 April 2013).

[35] V. Ramadesigan, P. W. C. Northrop, S. De, S. Santhanagopalan, R. D. Braatz, and V. R. Subramanian, "Modeling and Simulation of Lithium-Ion Batteries from a Systems Engineering Perspective," *Journal of The Electrochemical Society*, vol. 159, no. 3, pp. R31–R45, 2012.

[36] M. Chen and G. Rincon-Mora, "Accurate electrical battery model capable of predicting runtime and I-V performance," *Energy Conversion, IEEE Transactions on*, vol. 21, no. 2, pp. 504–511, 2006.

[37] H.-G. Schweiger, O. Obeidi, O. Komesker, A. Raschke, M. Schiemann, C. Zehner, M. Gehnen, M. Keller, and P. Birke, "Comparison of Several Methods for Determining the Internal Resistance of Lithium Ion Cells," *Sensors*, vol. 10, no. 6, pp. 5604–5625, 2010.

[38] W. Waag, S. Käbitz, and D. U. Sauer, "Experimental investigation of the lithium-ion battery impedance characteristic at various conditions and aging states and its influence on the application," *Applied Energy*, vol. 102, no. C, pp. 885–897, 2013.

[39] L. W. Yao and J. Aziz, "Modeling of Lithium ion battery with nonlinear transfer resistance," in *Applied Power Electronics Colloquium (IAPEC), 2011 IEEE*, pp. 104–109, 2011.

[40] D. Andre, M. Meiler, K. Steiner, C. Wimmer, T. Soczka-Guth, and D. Sauer, "Characterization of high-power lithium-ion batteries by electrochemical impedance spectroscopy. I. Experimental investigation," *Journal of Power Sources*, vol. 196, no. 12, pp. 5334 – 5341, 2011.

[41] M. Ates, "Review study of electrochemical impedance spectroscopy and equivalent electrical circuits of conducting polymers on carbon surfaces," *Progress in Organic Coatings*, vol. 71, no. 1, pp. 1 – 10, 2011.

[42] P. Hansen, V. Pereyra, and G. Scherer, *Least Squares Data Fitting with Applications*. Least Squares Data Fitting with Applications, Johns Hopkins University Press, 2012.

[43] A. Bard and L. Faulkner, *Electrochemical Methods: Fundamentals and Applications*. Wiley, 2001.

[44] *Small time step simulation-An introductory tutorial*. RTDS technologies.

[45] R. Pena, J. Clare, and G. Asher, "Doubly fed induction generator using back-to-back PWM converters and its application to variable-speed wind-energy generation," *Electric Power Applications, IEE Proceedings -*, vol. 143, no. 3, pp. 231–241, 1996.

[46] S. Chaudhary, *Control and Protection of Wind Power Plants with VSC-HVDC Connection*. PhD thesis, 2011.

[47] Y. Ren, L. Cao, J. Zhou, L. Liu, M. Zhang, and H. Li, "The modeling and control of VSCF DFIG wind power generation based on PSCAD," in *Intelligent Control and Information Processing (ICICIP), 2010 International Conference on*, pp. 24–28, 2010.

[48] H. Mäkinen, A.; Tuusa, "Wind turbine and grid interaction studies using integrated real-time simulation environment," (Tampere University of Technology), p. 8, Proceedings of the Nordic Workshop on Power and Industrial Electronics (NORPIE/2008), 2008.

[49] A. Lopes, J. P. A. Vieira, M. V. A. Nunes, U. Bezerra, and A. Nascimento, "Using genetic algorithm to tune PI-controllers for the direct-drive synchronous wind generators," in *Modern Electric Power Systems (MEPS), 2010 Proceedings of the International Symposium*, pp. 1–8, 2010.

[50] L. Rolim, D. da Costa, and M. Aredes, "Analysis and Software Implementation of a Robust Synchronizing PLL Circuit Based on the pq Theory," *Industrial Electronics, IEEE Transactions on*, vol. 53, no. 6, pp. 1919–1926, 2006.

[51] "dSPACE Simulator." [brochure], 2011. dSPACE GmbH.

[52] "dSPACE HelpDesk." [manual], November 2011. dSPACE GmbH.

[53] "Nanophosphate® High Power Lithium Ion Cell ANR26650M1-B." [data sheet], 2012. A123 Systems, Inc.

[54] "A123 ALM12V7 Charging Considerations." [application note], September 2012. A123 Systems, Inc.

[55] R. Teodorescu, D. U. Sauer, P. Rodriguez, and M. Swierczynski, "Storage Systems based on Li-Ion Batteries for Stationary Applications." Industrial/PhD Course, March 2012. Department of Energy Technology, Aalborg University.

[56] J. Morren, S. W. H. de Haan, W. L. Kling, and J. A. Ferreira, "Wind turbines emulating inertia and supporting primary frequency control," *Power Systems, IEEE Transactions on*, vol. 21, no. 1, pp. 433–434, 2006.

[57] "The Electropaedia." [online]. Available: `http://www.mpoweruk.com/beginners.htm` (Accessed: 10 April 2013).

[58] "A Guide to Understanding Battery Specifications." [online]. Available: http://mit.edu/evt/summary_battery_specifications.pdf (Accessed: 14 April 2013).

[59] I. Buchmann, "Battery University." [online]. Available: http://batteryuniversity.com/learn/article/confusion_with_voltages (Accessed: 10 April 2013).

A Appendix: Battery terminology

A.1 Basic terms and abbreviations of batteries

Basic terms and abbreviations of batteries, based on [57], [58] and [59], are stated in this section.

Cells: The smallest elementary unit of a battery is an energy cell. Although, there is a wide selection of available options, the energy cell is based only on one specific chemistry for the anode and the cathode. It determines voltage of the cell, which is usually between 1 - 6 V. Two types of cells are recognized: primary and secondary. The main difference is in their recharging ability. Primary cells get fully discharged only once and they cannot be charged again whereas secondary cells are rechargeable .

Modules and packs: A battery module is a building unit consisting of number of cells. Modules are further sorted together to create a battery pack. Any of battery units can be connected in series, parallel or both. By connecting units in series, the voltage of the group is obtained by summing up the voltages of the individual units and the ampere hour capacity remains constant. When units are connected in parallel, the ampere hour capacity is the summation of the individual unit's capacity and the voltage remains constant. The series, parallel and their combination of sorting is shown in Fig. A.1 [57].

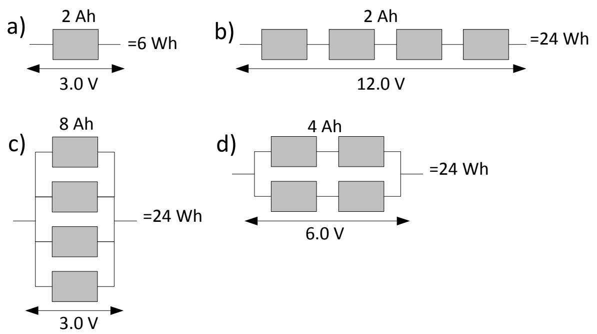

Figure A.1: Connection of battery cells: a) a single cell, b) cells in series, c) cells in parallel, d) cells in series and parallel.

Relations between shown quantities in Fig. A.1 are described by following equations A.1 and A.2

$$Q = It \qquad [Ah] \tag{A.1}$$

$$E = QV \qquad [Wh] \tag{A.2}$$

Where,

Q = Capacity - electric charge [Ah]
I = Current [A]
t = Time [h]
E = Energy [Wh]
V = Voltage [V]

Classification: There are two most commonly used classification properties, such as high power and high energy. Further classification parameters are chemistry, safety, cost and durability based on life time.

C-rate: It serves as a normalized expression for charging and discharging current of batteries in relation to their capacity. The nominal capacity of a battery in ampere hour stands as a base and C-rate is a relative rate of current. 1C means, a battery is charged/discharged by the current at the value of the nominal capacity for the period of one hour. For better understanding and representation of C-rate, Table A.1 is included.

Table A.1: C-rate and corresponding values for charging/discharging for a battery with the capacity of 2.5 Ah.

Nominal capacity of the battery = 2.5 Ah		
C-rate	**Current [A]**	**Time period [h]**
0.5C	1.25	2
1C	2.5	1
2C	5	0.5
4C	10	0.25

Nominal voltage - [V]: It represents the reference voltage of the battery. It is the average value of the voltage when a fully charged battery is completely discharged by the rate of 0.5C. This value is derived from its plotted curve.

Terminal voltage - [V]: It is the value of the voltage on the battery terminal, when a load is applied. It depends on a state of charge, charging/discharging current and its duration.

Open-circuit voltage (OCV) - [V]: It is the value of the voltage on the battery terminal, when a load is not applied. It depends on the state of charge.

Cut-off voltage - [V]: It is the value of the voltage when the discharging process is stopped. By neglecting a battery dynamic and relaxation time, it can represent the voltage of a fully discharged battery.

Capacity and nominal capacity - [Ah]: It represents an actual or a nominal value of the coulometric capacity expressed by ampere hours [Ah]. The nominal value stands for a current which can be dragged out of a battery for one hour or adequate time according the C-rate.

Energy and nominal energy - [Wh]: It stands for actual or nominal watt hours respectively, which can be provided and it is as well related to the C-rate.

Specific energy - [Wh/kg]: It captures chemical aspects of the battery and its packaging. It specifies the battery weight so that a given electric range can be attained.

Specific power - [W/kg]: Another measure that captures chemical aspects of the battery and its packaging. It determines the battery weight needed for a given performance goal.

Energy density - [Wh/l]: The measure determines the final battery size so the required electric range can be achieved.

Power density - [W/l]: It is similar as energy density measure where it determines battery size requirements for a particular performance target or goal.

Internal resistance - [Ω*]*: It is the resistance inside of a battery, which influences losses. It depends highly on temperature and age, further also on the state of charge and charging/discharging process.

State of charge (SOC) - [%]: SOC represents an actual level of battery capacity in relation to its maximum possible state.

Depth of discharge (DOD) - [%]: A measure that reflects the ratio of the amount of battery capacity which has been discharged to the total, maximum possible capacity.

Life time: At batteries, there are distinguished calendar [years] and cycle [cycles] life time. Both interprets an amount of units until the end of battery life, which is determined by the certain amount of capacity degradation. They are dependent on the temperature, humidity, level of the SOC as well as on the rate and depth of cycles.

B Appendix: Modeling

B.1 12-Bus Data

B.1.1 Load parameters

Table B.1: Load parameters of 12-bus system.

Load	P[MW]	Power factor [pf]
L1	300	0.85
L2	250	0.90
L3	350	0.95
L4	300	0.85
L5	100	0.90
L6	150	0.95
Total	**1450**	

B.1.2 Generator parameters

Table B.2: Generator parameters of 12-bus system.

Generator	S[MVA]	Active Power [MW]	Reactive power [MVAr]	H [MWs/MVA]
G1	750	477	144	10.01
G2A	320	200	68	8.32
G2B	640	200	68	8.32
G3	400	270	74	6.93
G4	474	330	59	6.67
Total	**2264**	**1477**	**413**	

B.1.3 Line parameters

Table B.3: Line parameters of 12-bus system.

Line	+ve seq resistance [pu]	+ve seq reactance [pu]	+ve seq cap reactance [pu]
Line 12	0.01131	0.08998	5.4416
Line 16	0.03394	0.26995	1.8139
Line 25	0.04530	0.35990	1.3604
Line 34(1)	0.01140	0.09000	5.4422
Line 34(2)	0.01140	0.09000	5.4422
Line 45	0.01700	0.13500	3.6271
Line 46	0.03394	0.26995	1.81394
Line 78	0.01590	0.17210	0.3044

B.1.4 Transformer

Table B.4: Transformer parameters of 12-bus system.

Transformer	S[MVA]	Primary V [kV]	secondary V [kV]	Leakage inductance [pu]
T9_1	800	15.5	230	0.12
T10_2A	350	15.0	230	0.12
T10_2B	350	15.0	230	0.12
T12_6	500	13.8	230	0.11
T11_1	400	18.0	2304	0.10
T1_7	500	230.0	345	0.13
T7_3	500	230.0	345	0.13

B.2 200 MW VSC design

B.2.1 Base Values

Base MVA (S_b) = 200 MVA
Base voltage at 230 kV bus ($V_{b,ll1}$) = 230 kV
Base voltage at 88 kV bus towards grid side ($V_{b,ll2}$) = 88 kV
Base voltage at 88 kV bus towards VSC ($V_{b,ll3}$) = 88 kV

B.2.2 General parameters

Rated wind power plant(WPP) Power (P_R)= 200 MW
Power Factor (pf) = 0.9
MVA rating of WPP = 220 MVA
Grid Voltage (V_{ll}) = 230 Kv
Fundamental frequency (f) = 50 Hz
Angular Frequency (ω) = $2\pi 50$ = 314.16 rad/s

B.2.3 Converter transformer

The converter transformer are used to step up the AC voltage generated from the PWM to match the system voltage. the ratings of the transformer are as follows
Voltage Ratio = $\frac{88kV}{88kV}$
MVA rating of transformer = 220 MVA
No load losses = 0.005 pu
copper losses = 0.005 pu

B.2.4 VSC parameters

The per unit base of the DC-link Voltage was selected on the basis of dc voltage of the bridge when blocked i.e, (V_{DCb}) = $\frac{3\sqrt{2}\times V_{b,ll3}}{\pi} = \frac{3\sqrt{2}\times 88}{\pi} = 120kV$
The losses in the converter is determined to be 4% per VSC $(= 0.04 \times 200 = 8\ MJ/s)$.
Switching frequency (f_{switch}) = 1050 Hz
Snubber Capacitance ($C_{snubber}$) = 0.00169 μf
Snubber Resistance ($R_{snubber}$) = 2942.35 Ω

B.2.5 Filter

Var Compensation is selected arbitarily to have 10% of MVA rating = 0.01x200 = 20 MVAR).
The filter is tuned to cutoff at the switching frequency of the PWM
Capacitive impedance (X_{cf}) = $\frac{88^2}{20}$ = 387.2 Ω
$C_f = \frac{1}{X_{cf}\times\omega} = \frac{1}{387.2\times 314.15}$ = 8.2210 μf
Neglecting the parallel resistor, a LC circuit is formed. The value of inductance is selected such that resonance occurs at switching frequency. Hence the impedence of capacitor and inductior cancels each other to provide low resistance path to ground.
Resonant Frequency (ω_{res}) = $2\pi \times f_{switch}$ = $2\pi 1050$ = 6597.34 rad/sec
Filter inductor $L_f = \frac{1}{\omega_{res}^2 C_f}$ =0.00279 H

The value of R is selected equal to the impedance of inductance connected in parallel.
Filter resistance $(R_f) = \omega_{res} L_f$ = 0.01843 Ω

B.2.5.1 Phase reactor

The line reactors are selected arbitarily with per unit impedance = (0.0005+j2.05). This gives
Base impedance, $(Z_{b,3}) = \frac{V_{b,ll3}^2}{S_b} = \frac{88^2}{200} = 38.72\Omega$
Reactor resistance (R_{pr}) = 0.0005x38.72 = 0.02 Ω
Reactor inductance (L_{pr}) = $\frac{2.05\times38.72}{314.16}$ = 8.6 mH

B.3 The extracted parameters from EIS fitting

Table B.5: The extracted parameters from fitting, rounded up to four decimal numbers, and their fitting error. The final row represents the values used in equivalent electrical circuit in the model.

SOC [%]	R$_{Bat}$ [mΩ]	L$_{Bat}$ [nH]	R$_{DL}$ [mΩ]	C$_{DL}$ [mF]	R$_{Diff}$ [mΩ]	C$_{Diff}$ [F]	Error [%]
0	4.4111	150.3840	26.4131	499.4260	358.5860	32.8100	6.93
10	5.6959	11.2748	2.7456	550.0000	16.1000	1185.0000	4.41
20	5.6487	11.5385	2.7141	479.9990	14.1001	1224.0000	4.59
30	5.6328	12.8544	2.7270	456.9660	13.2095	1288.9600	4.76
40	5.6479	12.0613	2.6901	472.0850	13.2015	1279.8600	4.79
50	5.6552	11.3612	2.6763	480.0000	13.2001	1230.0000	4.72
60	5.6603	11.5604	2.6533	507.2470	14.9305	1220.0000	4.48
70	5.6512	11.4082	2.6114	519.9990	16.1440	1184.5400	4.61
80	5.6133	13.1070	2.5557	472.2710	14.0045	1237.0000	4.74
90	5.5936	14.4835	2.4898	453.4370	14.2195	1194.6300	4.62
100	5.5542	14.1817	3.1245	473.1070	130.1080	343.7600	4.19
Final	-	12.1833	2.6515	488.0000	14.3455	1227.1100	-

C Appendix: Study cases

The parameters and results for the specific scenarios of study cases are presented in this Appendix. Generally for all scenarios, the first table represents the generation units, their power rating, inertial constant and initial values of active and reactive power production. The second table shows values for loads, inductors and capacitors in the grid. In the third table, there are presented results for all buses in terms of the minimal point of frequency, ROCOF and time to reach the minimal point of frequency.

The graphs illustrated on the other page of scenarios stand for:

a) Active power from generation units
b) Reactive power from generation units
c) Active power consumption of loads
d) Reactive power consumption of loads
e) Frequency profiles of all buses
f) Voltage profiles of all buses

All scenarios, listed in this Appendix, are presented in Table C.1.

Table C.1: List of scenarios presented in Appendix C.

Scenario	Specification
BSC1	0 % WPP penetration
BSC2	9 % WPP penetration
BSC3	16 % WPP penetration
BSC4	24 % WPP penetration
BSC5	33 % WPP penetration
BSC6	33 % WPP penetration, with C6
SC13	33 % WPP penetration, 10 MW ESS, derivative control with T_{ESS} = 0.5 and K_{ESS} = 7
SC13C	33 % WPP penetration, 10 MW ESS, derivative control with T_{ESS} = 0.5 and K_{ESS} = 7, with C6
SC2_6	33 % WPP penetration, 15 MW ESS, derivative control with T_{ESS} = 0.5 and K_{ESS} = 7
SC2_6C	33 % WPP penetration, 15 MW ESS, derivative control with T_{ESS} = 0.5 and K_{ESS} = 7, with C6
SC3_4	33 % WPP penetration, 15 MW ESS, combination of derivative and droop control, T_{ESS} = 0.5 and K_{ESS} = 7, control ratio = 0.25
SC3_4C	33 % WPP penetration, 15 MW ESS, combination of derivative and droop control, T_{ESS} = 0.5 and K_{ESS} = 7, control ratio = 0.25, with C6

C.1 Base study case - results

C.1.1 BSC1

Table C.2: Generation settings.

Generation units	Power rating [MVA]	Active power* [MW]	Reactive power* [MVAr]	Inertia constant* [MWs/MVA]
G1	750	544	157	10.01
G2	640	395	131	8.32
G3	400	247	27	6.93
G4	474	293	43	6.67
WPP1	-	-	-	-
WPP2	-	-	-	-
WPP3	-	-	-	-
WPP4	-	-	-	-
Total	2264	1478	358	8.29

*initial steady state value

Table C.3: Load, inductors and capacitors settings.

Load	Active power [MW]	Reactive power [MVAr]	Power factor [-]	Note
L1	300	186	0.85	
L2	250	121	0.90	
L3	350	116	0.95	
L4	300	186	0.85	
L5	100	48	0.90	
L6	150	49	0.95	
L7	0	144	-	Shunt inductor
C4	0	200	-	Shunt capacitor
C5	0	40	-	Shunt capacitor
C6	-	-	-	Shunt capacitor

Table C.4: BSC1: results for all buses.

	f_{min} [Hz]	df/dt [Hz/s]	t_{min} [s]
Bus 1	49.5940	0.2703	5.3136
Bus 2	49.5900	0.1843	4.9208
Bus 3	49.5952	0.2602	4.7032
Bus 4	49.5924	0.2500	4.6904
Bus 5	49.5917	0.2227	4.7704
Bus 6	49.5758	0.2745	4.5848
Bus 7	49.5951	0.2696	5.3064
Bus 8	49.5965	0.2614	4.7136

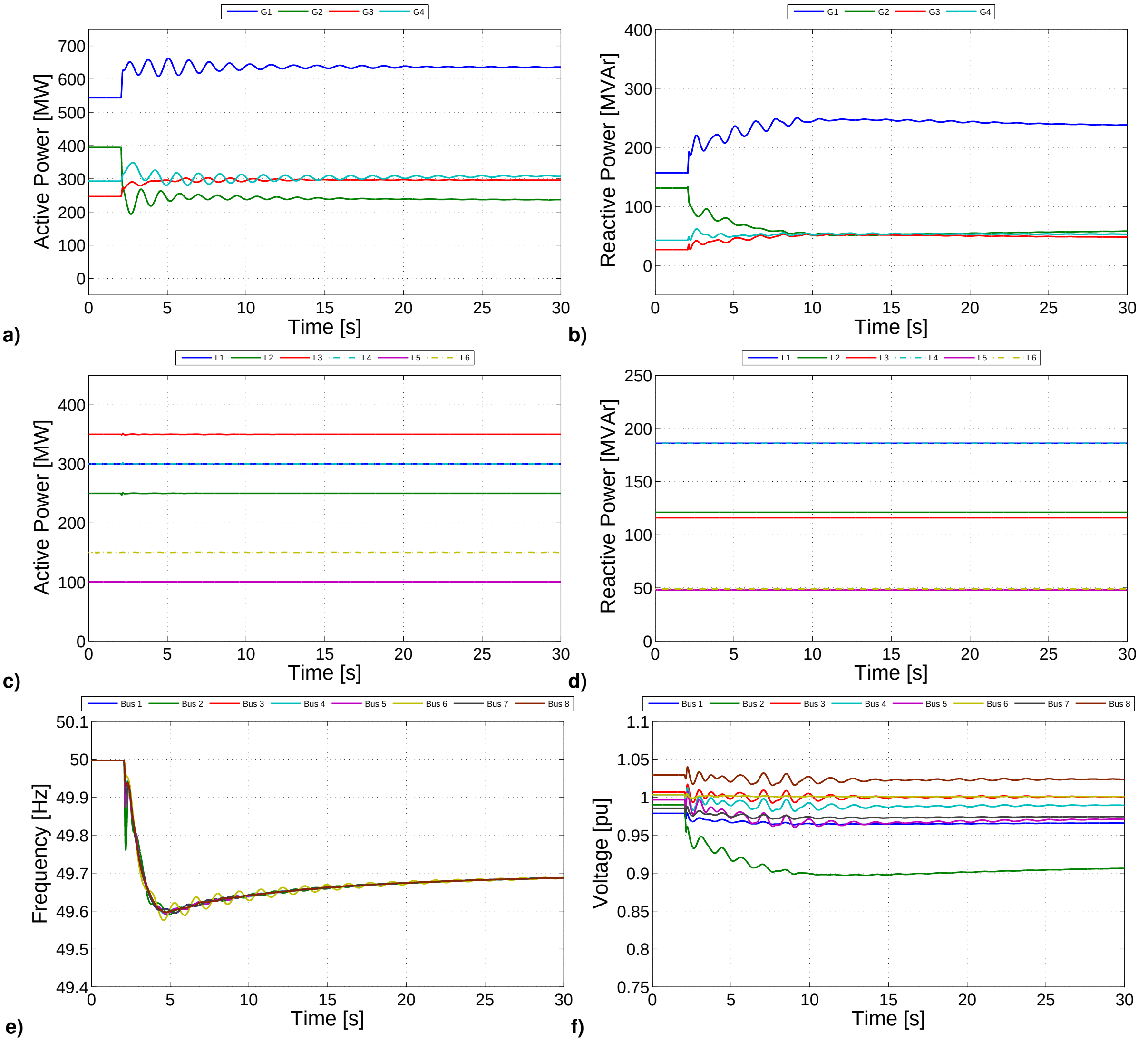

Figure C.1: a) active power from generation units, b) reactive power from generation units, c) active power consumption of loads, d) reactive power consumption of loads, e) frequency at buses, f) voltage at buses.

C.1.2 BSC2

Table C.5: Generation settings.

Generation units	Power rating [MVA]	Active power* [MW]	Reactive power* [MVAr]	Inertia constant* [MWs/MVA]
G1	750	542	162	10.01
G2	640	393	154	8.32
G3	400	246	56	6.93
G4	474	292	53	6.67
WPP1	220	200	15	0
WPP2	-	-	-	-
WPP3	-	-	-	-
WPP4	-	-	-	-
Total	2484	1673	440	7.56

*initial steady state value

Table C.6: Load, inductors and capacitors settings.

Load	Active power [MW]	Reactive power [MVAr]	Power factor [-]	Note
L1	333	207	0.85	
L2	283	137	0.90	
L3	383	127	0.95	
L4	333	207	0.85	
L5	135	65	0.90	
L6	185	60	0.95	
L7	0	144	-	Shunt inductor
C4	0	200	-	Shunt capacitor
C5	0	40	-	Shunt capacitor
C6	-	-	-	Shunt capacitor

Table C.7: BSC2: results for all buses.

	f_{min} [Hz]	df/dt [Hz/s]	t_{min} [s]
Bus 1	49.5942	0.2674	5.3528
Bus 2	49.5897	0.1862	4.9768
Bus 3	49.5954	0.2712	4.6584
Bus 4	49.5925	0.2636	4.6616
Bus 5	49.5921	0.2377	4.7952
Bus 6	49.5740	0.2706	4.6144
Bus 7	49.5956	0.2674	5.3192
Bus 8	49.5967	0.2696	4.4684

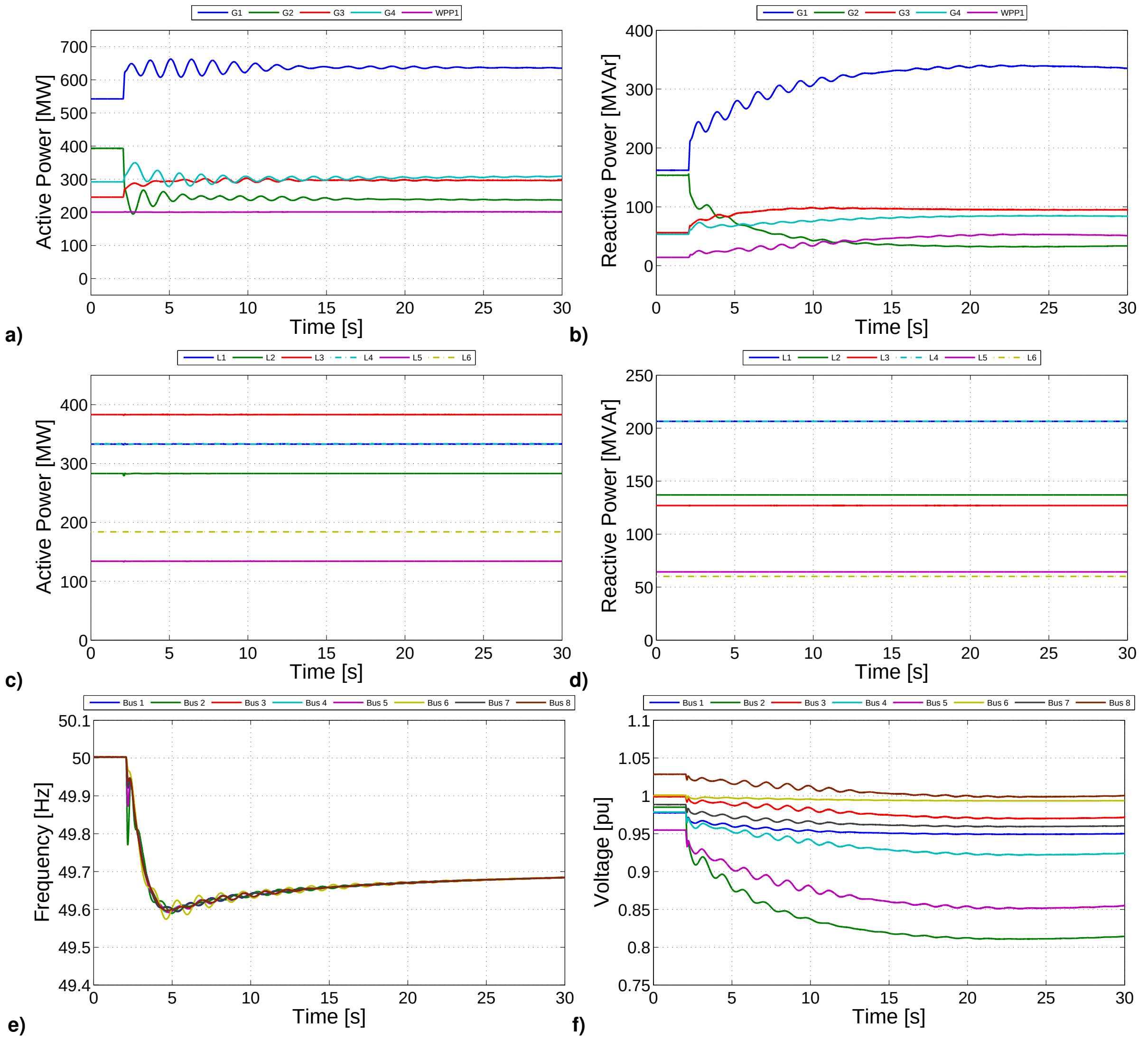

Figure C.2: a) active power from generation units, b) reactive power from generation units, c) active power consumption of loads, d) reactive power consumption of loads, e) frequency at buses, f) voltage at buses.

C.1.3 BSC3

Table C.8: Generation settings.

Generation units	Power rating [MVA]	Active power* [MW]	Reactive power* [MVAr]	Inertia constant* [MWs/MVA]
G1	750	536	165	10.01
G2	640	394	157	8.32
G3	400	246	37	6.93
G4	474	292	50	6.67
WPP1	220	200	7	0
WPP2	220	200	20	0
WPP3	-	-	-	-
WPP4	-	-	-	-
Total	2704	1868	436	6.94

*initial steady state value

Table C.9: Load, inductors and capacitors settings.

Load	Active power [MW]	Reactive power [MVAr]	Power factor [-]	Note
L1	366	227	0.85	
L2	316	153	0.90	
L3	416	138	0.95	
L4	366	227	0.85	
L5	168	50	0.96	
L6	218	71	0.95	
L7	0	144	-	Shunt inductor
C4	0	200	-	Shunt capacitor
C5	0	40	-	Shunt capacitor
C6	-	-	-	Shunt capacitor

Table C.10: BSC3: results for all buses.

	f_{min} [Hz]	df/dt [Hz/s]	t_{min} [s]
Bus 1	49.5903	0.2711	5.3664
Bus 2	49.5842	0.1978	4.9648
Bus 3	49.5900	0.2712	4.7048
Bus 4	49.5875	0.2657	4.7040
Bus 5	49.5869	0.2412	4.8088
Bus 6	49.5705	0.2715	4.6200
Bus 7	49.5918	0.2705	5.3456
Bus 8	49.5914	0.2696	4.7056

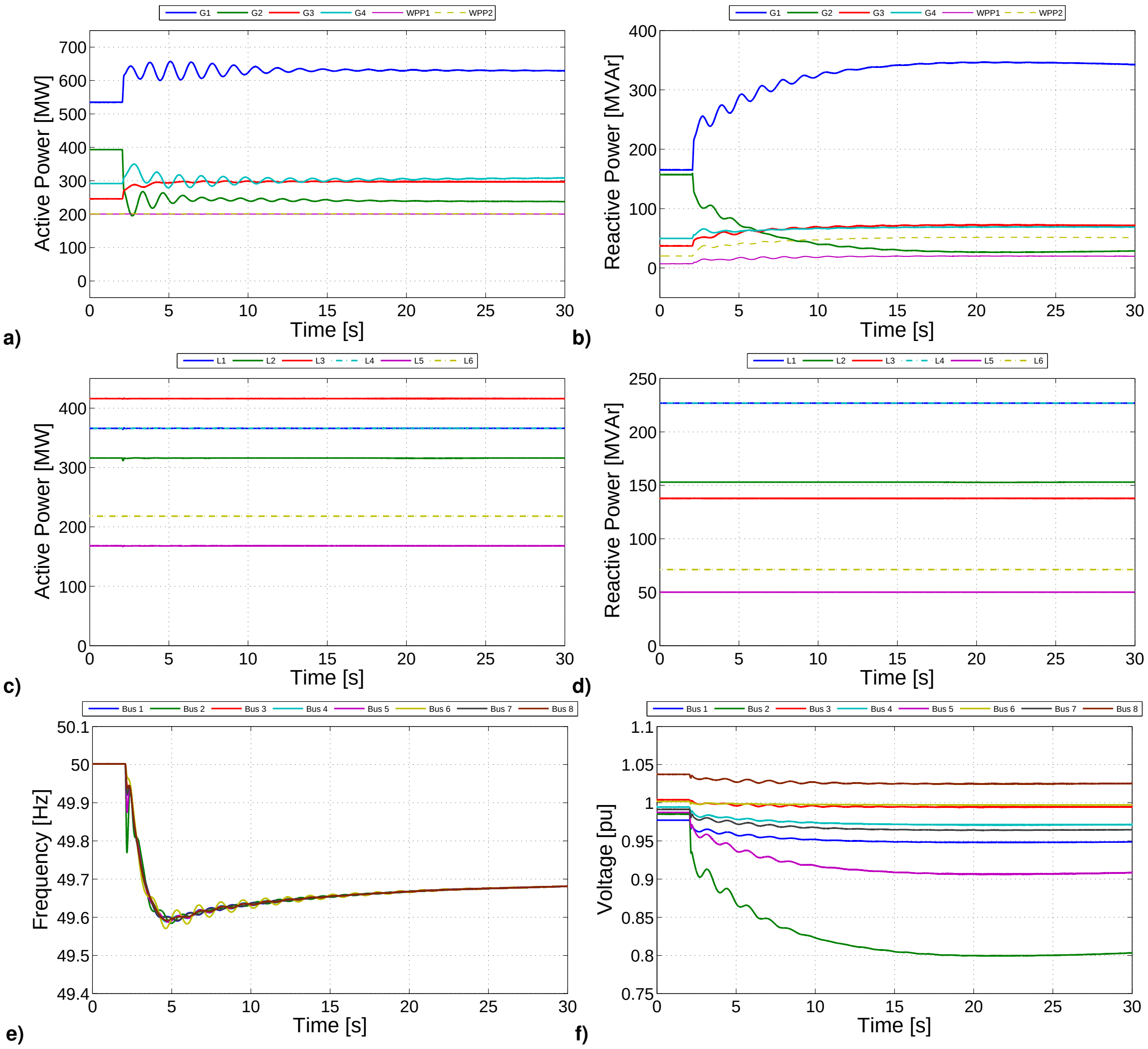

Figure C.3: a) active power from generation units, b) reactive power from generation units, c) active power consumption of loads, d) reactive power consumption of loads, e) frequency at buses, f) voltage at buses.

C.1.4 BSC4

Table C.11: Generation settings.

Generation units	Power rating [MVA]	Active power* [MW]	Reactive power* [MVAr]	Inertia constant* [MWs/MVA]
G1	750	518	160	10.01
G2	640	394	154	8.32
G3	200	123	23	6.93
G4	474	231	46	6.67
WPP1	220	200	13	0
WPP2	220	200	22	0
WPP3	220	200	13	0
WPP4	-	-	-	-
Total	2724	1865	430	6.38

*initial steady state value

Table C.12: Load, inductors and capacitors settings.

Load	Active power [MW]	Reactive power [MVAr]	Power factor [-]	Note
L1	366	227	0.85	
L2	316	153	0.90	
L3	416	138	0.95	
L4	366	227	0.85	
L5	168	50	0.96	
L6	218	71	0.95	
L7	0	144	-	Shunt inductor
C4	0	200	-	Shunt capacitor
C5	0	40	-	Shunt capacitor
C6	-	-	-	Shunt capacitor

Table C.13: BSC4: results for all buses.

	f_{min} [Hz]	df/dt [Hz/s]	t_{min} [s]
Bus 1	49.5280	0.3092	5.3024
Bus 2	49.5162	0.2297	4.9120
Bus 3	49.5269	0.3122	4.6816
Bus 4	49.5254	0.3074	4.6808
Bus 5	49.5235	0.2801	4.7664
Bus 6	49.5143	0.3201	4.5176
Bus 7	49.5289	0.3090	5.3024
Bus 8	49.5278	0.3100	4.7088

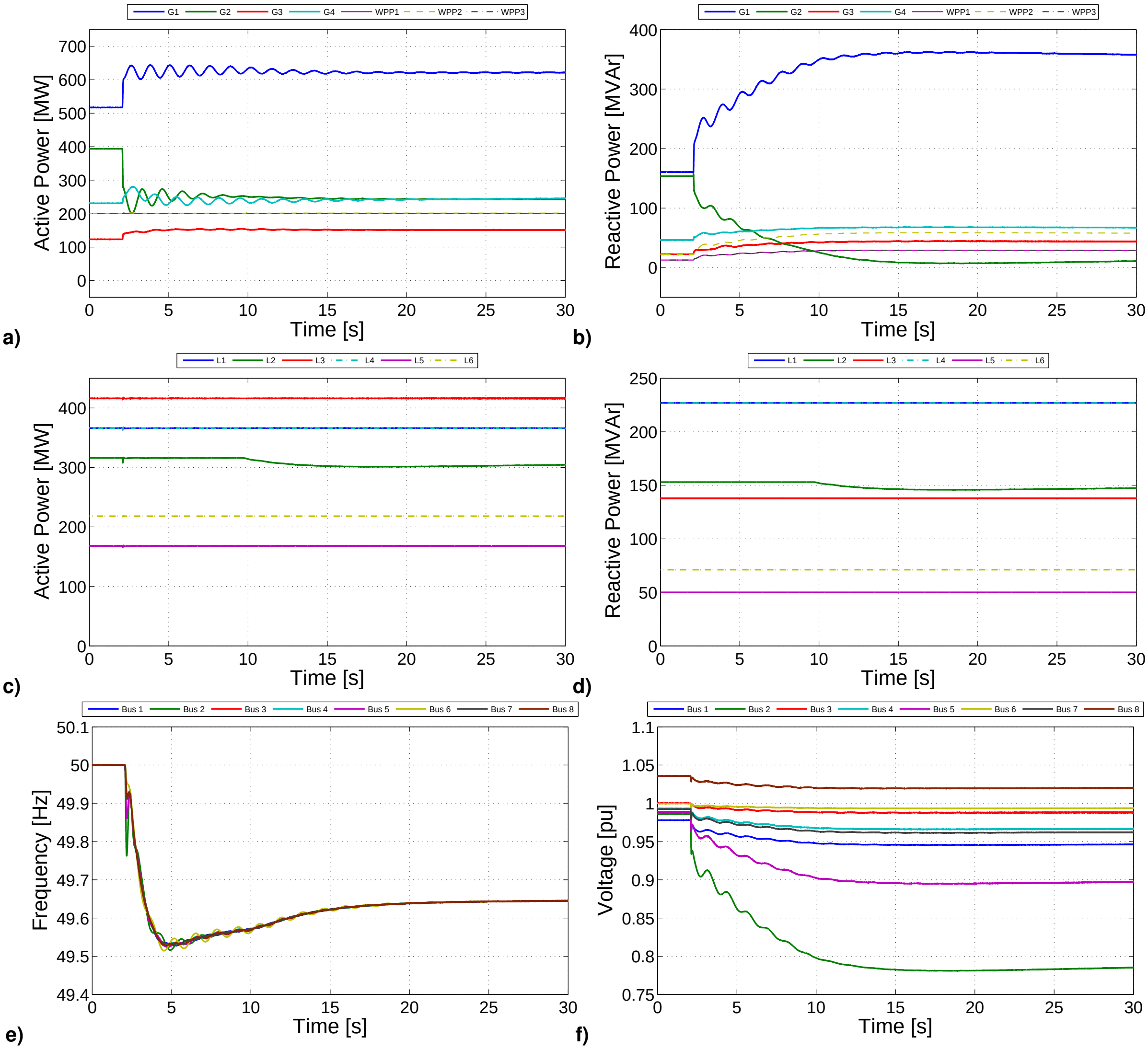

Figure C.4: a) active power from generation units, b) reactive power from generation units, c) active power consumption of loads, d) reactive power consumption of loads, e) frequency at buses, f) voltage at buses.

C.1.5 BSC5

Table C.14: Generation settings.

Generation units	Power rating [MVA]	Active power* [MW]	Reactive power* [MVAr]	Inertia constant* [MWs/MVA]
G1	750	435	153	10.01
G2	640	396	136	8.32
G3	-	-	-	-
G4	374	230	42	6.67
WPP1	220	200	15	0
WPP2	220	200	15	0
WPP3	220	200	15	0
WPP4	220	200	1	0
Total	2644	1860	378	5.80

*initial steady state value

Table C.15: Load, inductors and capacitors settings.

Load	Active power [MW]	Reactive power [MVAr]	Power factor [-]	Note
L1	366	227	0.85	
L2	316	153	0.90	
L3	416	138	0.95	
L4	366	227	0.85	
L5	168	50	0.96	
L6	218	71	0.95	
L7	0	144	-	Shunt inductor
C4	0	200	-	Shunt capacitor
C5	0	40	-	Shunt capacitor
C6	-	-	-	Shunt capacitor

Table C.16: BSC5: results for all buses.

	f_{min} [Hz]	df/dt [Hz/s]	t_{min} [s]
Bus 1	49.4602	0.3413	5.3512
Bus 2	49.4478	0.2652	4.9096
Bus 3	49.4610	0.3422	5.8368
Bus 4	49.4603	0.3395	5.8360
Bus 5	49.4582	0.3183	4.9056
Bus 6	49.4530	0.3593	5.6960
Bus 7	49.4604	0.3407	5.3504
Bus 8	49.4614	0.3390	5.5784

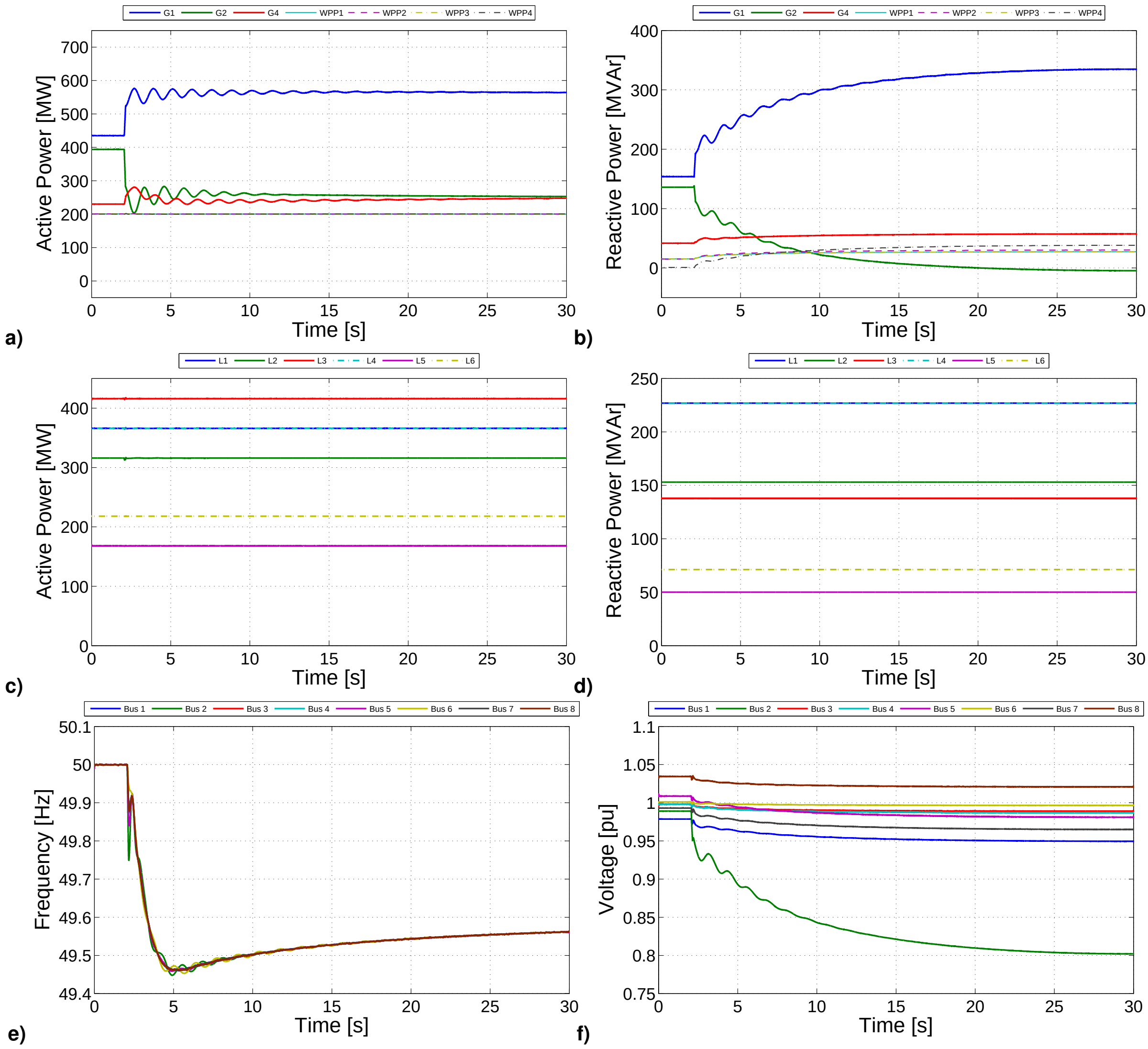

Figure C.5: a) active power from generation units, b) reactive power from generation units, c) active power consumption of loads, d) reactive power consumption of loads, e) frequency at buses, f) voltage at buses.

C.1.6 BSC6

Table C.17: Generation settings.

Generation units	Power rating [MVA]	Active power* [MW]	Reactive power* [MVAr]	Inertia constant* [MWs/MVA]
G1	750	436	124	10.01
G2	640	394	-39	8.32
G3	-	-	-	-
G4	374	229	39	6.67
WPP1	220	200	14	0
WPP2	220	200	13	0
WPP3	220	200	14	0
WPP4	220	200	-6	0
Total	2644	1860	159	5.80

*initial steady state value

Table C.18: Load, inductors and capacitors settings.

Load	Active power [MW]	Reactive power [MVAr]	Power factor [-]	Note
L1	366	227	0.85	
L2	316	153	0.90	
L3	416	138	0.95	
L4	366	227	0.85	
L5	168	50	0.96	
L6	218	71	0.95	
L7	0	144	-	Shunt inductor
C4	0	200	-	Shunt capacitor
C5	0	40	-	Shunt capacitor
C6	-	200	-	Shunt capacitor

Table C.19: BSC6: results for all buses.

	f_{min} [Hz]	df/dt [Hz/s]	t_{min} [s]
Bus 1	49.4625	0.3317	5.1816
Bus 2	49.4570	0.1958	5.4712
Bus 3	49.4588	0.3238	5.4624
Bus 4	49.4583	0.3208	5.4640
Bus 5	49.4573	0.2863	5.4680
Bus 6	49.4578	0.3690	5.4680
Bus 7	49.4623	0.3297	5.4640
Bus 8	49.4592	0.3217	5.4632

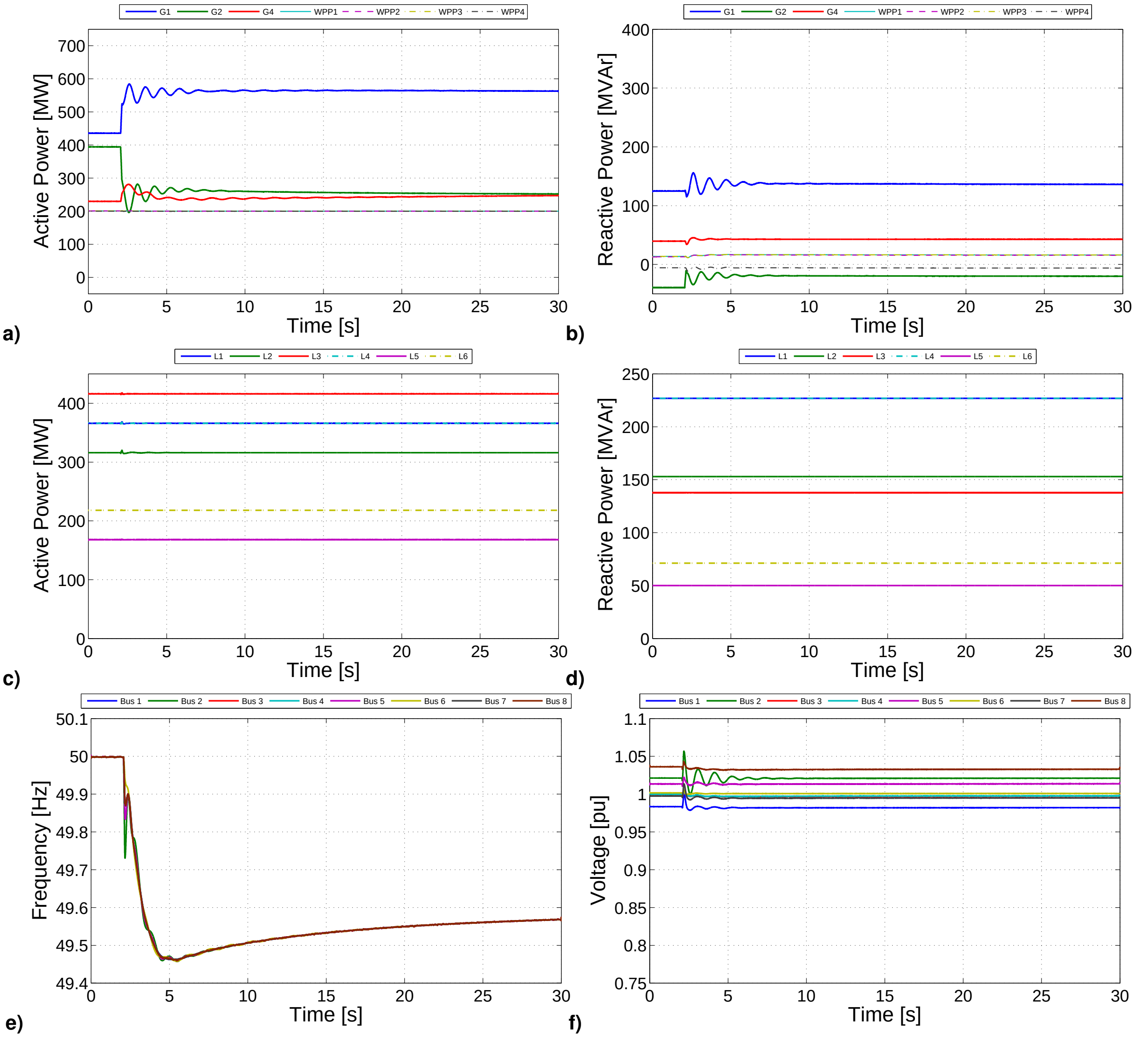

Figure C.6: a) active power from generation units, b) reactive power from generation units, c) active power consumption of loads, d) reactive power consumption of loads, e) frequency at buses, f) voltage at buses.

C.2 Study case 1 - results

C.2.1 SC13

Table C.20: Generation settings.

Generation units	Power rating [MVA]	Active power* [MW]	Reactive power* [MVAr]	Inertia constant* [MWs/MVA]
G1	750	436	154	10.01
G2	640	394	136	8.32
G3	-	-	-	-
G4	374	230	41	6.67
WPP1	220	200	15	0
WPP2	220	200	15	0
WPP3	220	200	15	0
WPP4	220	200	1	0
Total**	2644	1860	378	5.80

*initial steady state value
**excluding the ESS

Table C.21: Load, inductors and capacitors settings.

Load	Active power [MW]	Reactive power [MVAr]	Power factor [-]	Note
L1	366	226.92	0.85	
L2	316	152.94	0.90	
L3	416	137.87	0.95	
L4	366	226.92	0.85	
L5	168	50.00	0.96	
L6	218	71.21	0.95	
L7	0	144	-	Shunt inductor
C4	0	200	-	Shunt capacitor
C5	0	40	-	Shunt capacitor
C6	-	-	-	Shunt capacitor

Table C.22: SC13: results for all buses.

	f_{min} [Hz]	df/dt [Hz/s]	t_{min} [s]
Bus 1	49.4762	0.3234	6.3600
Bus 2	49.4662	0.2461	6.1656
Bus 3	49.4728	0.3201	5.9496
Bus 4	49.4723	0.3185	5.9480
Bus 5	49.4715	0.2979	5.9992
Bus 6	49.4654	0.3413	5.7264
Bus 7	49.4763	0.3222	6.3592
Bus 8	49.4733	0.3177	5.9496

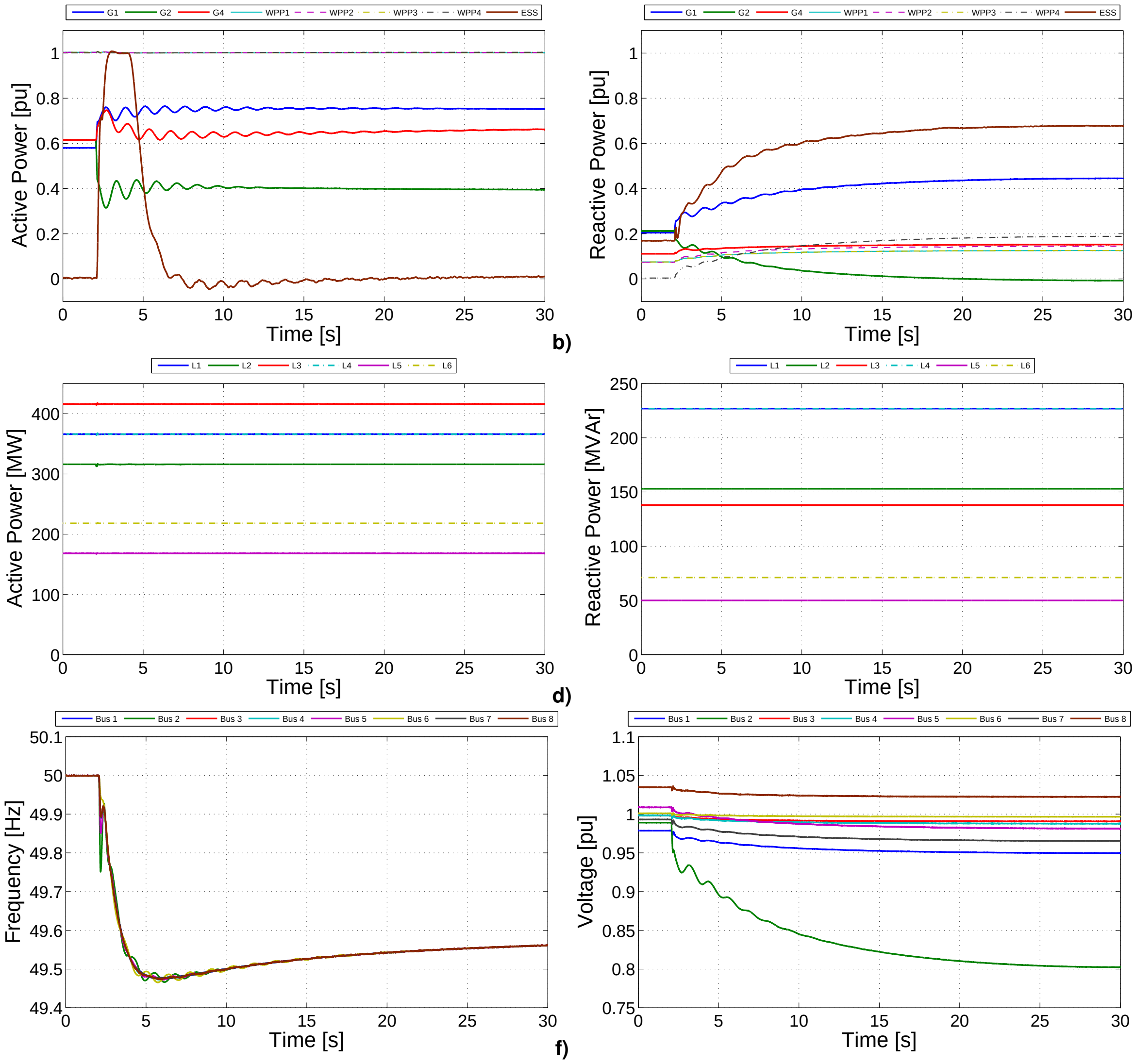

Figure C.7: a) active power from generation units, b) reactive power from generation units, c) active power consumption of loads, d) reactive power consumption of loads, e) frequency at buses, f) voltage at buses.

Table C.23: ESS parameters.

Nominal power [MW]	T_{ESS} [-]	K_{ESS} [-]	Control ratio [-]
10	0.5	7	1

C.2.2 SC13C

Table C.24: Generation settings.

Generation units	Power rating [MVA]	Active power* [MW]	Reactive power* [MVAr]	Inertia constant* [MWs/MVA]
G1	750	435	124	10.01
G2	640	394	-40	8.32
G3	-	-	-	-
G4	374	230	39	6.67
WPP1	220	200	14	0
WPP2	220	200	13	0
WPP3	220	200	14	0
WPP4	220	200	-6	0
Total**	2644	1859	158	5.80

*initial steady state value
**excluding the ESS

Table C.25: Load, inductors and capacitors settings.

Load	Active power [MW]	Reactive power [MVAr]	Power factor [-]	Note
L1	366	226.92	0.85	
L2	316	152.94	0.90	
L3	416	137.87	0.95	
L4	366	226.92	0.85	
L5	168	50.00	0.96	
L6	218	71.21	0.95	
L7	0	144	-	Shunt inductor
C4	0	200	-	Shunt capacitor
C5	0	40	-	Shunt capacitor
C6	-	200	-	Shunt capacitor

Table C.26: SC13C: results for all buses.

	f_{min} [Hz]	df/dt [Hz/s]	t_{min} [s]
Bus 1	49.4792	0.3160	5.9936
Bus 2	49.4744	0.1826	5.5296
Bus 3	49.4764	0.3086	5.4640
Bus 4	49.4759	0.3053	5.4624
Bus 5	49.4753	0.2709	5.4624
Bus 6	49.4752	0.3520	5.5952
Bus 7	49.4791	0.3141	5.7944
Bus 8	49.4768	0.3067	5.4632

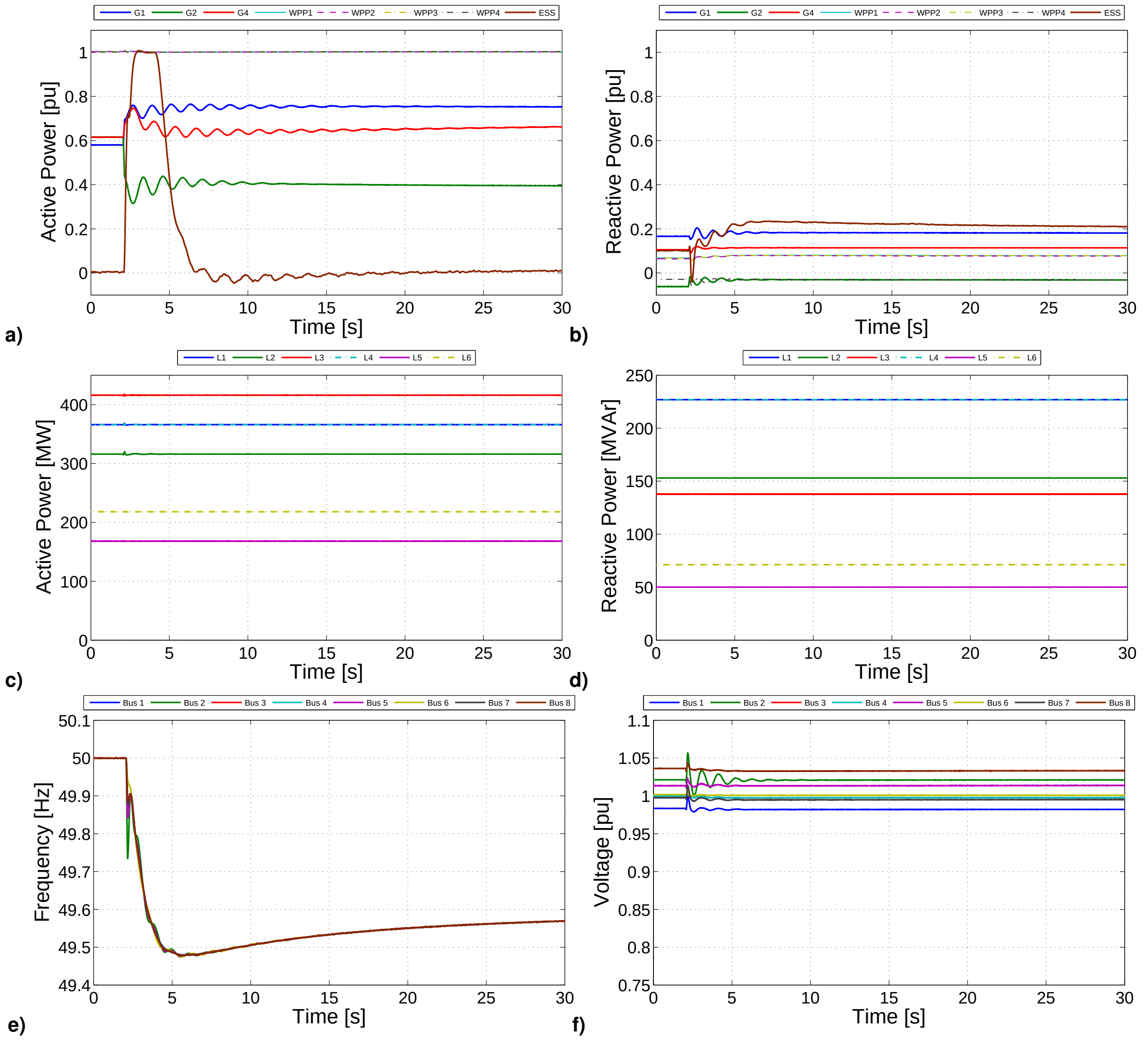

Figure C.8: a) active power from generation units, b) reactive power from generation units, c) active power consumption of loads, d) reactive power consumption of loads, e) frequency at buses, f) voltage at buses.

Table C.27: ESS parameters.

Nominal power [MW]	T_{ESS} [-]	K_{ESS} [-]	Control ratio [-]
10	0.5	7	1

C.3 Study case 2 - results

C.3.1 SC2_6

Table C.28: Generation settings.

Generation units	Power rating [MVA]	Active power* [MW]	Reactive power* [MVAr]	Inertia constant* [MWs/MVA]
G1	750	435	154	10.01
G2	640	395	136	8.32
G3	-	-	-	-
G4	374	228	41	6.67
WPP1	220	200	15	0
WPP2	220	200	15	0
WPP3	220	200	15	0
WPP4	220	200	1	0
Total**	2644	1858	377	5.80

*initial steady state value
**excluding the ESS

Table C.29: Load, inductors and capacitors settings.

Load	Active power [MW]	Reactive power [MVAr]	Power factor [-]	Note
L1	366	226.92	0.85	
L2	316	152.94	0.90	
L3	416	137.87	0.95	
L4	366	226.92	0.85	
L5	168	50.00	0.96	
L6	218	71.21	0.95	
L7	0	144	-	Shunt inductor
C4	0	200	-	Shunt capacitor
C5	0	40	-	Shunt capacitor
C6	-	-	-	Shunt capacitor

Table C.30: SC2_6: results for all buses.

	f_{min} [Hz]	df/dt [Hz/s]	t_{min} [s]
Bus 1	49.4763	0.3160	6.6840
Bus 2	49.4678	0.2415	6.1608
Bus 3	49.4753	0.3090	7.1832
Bus 4	49.4746	0.3070	5.8744
Bus 5	49.4737	0.2880	6.1176
Bus 6	49.4687	0.3314	5.7368
Bus 7	49.4765	0.3142	6.6840
Bus 8	49.4758	0.3071	7.1824

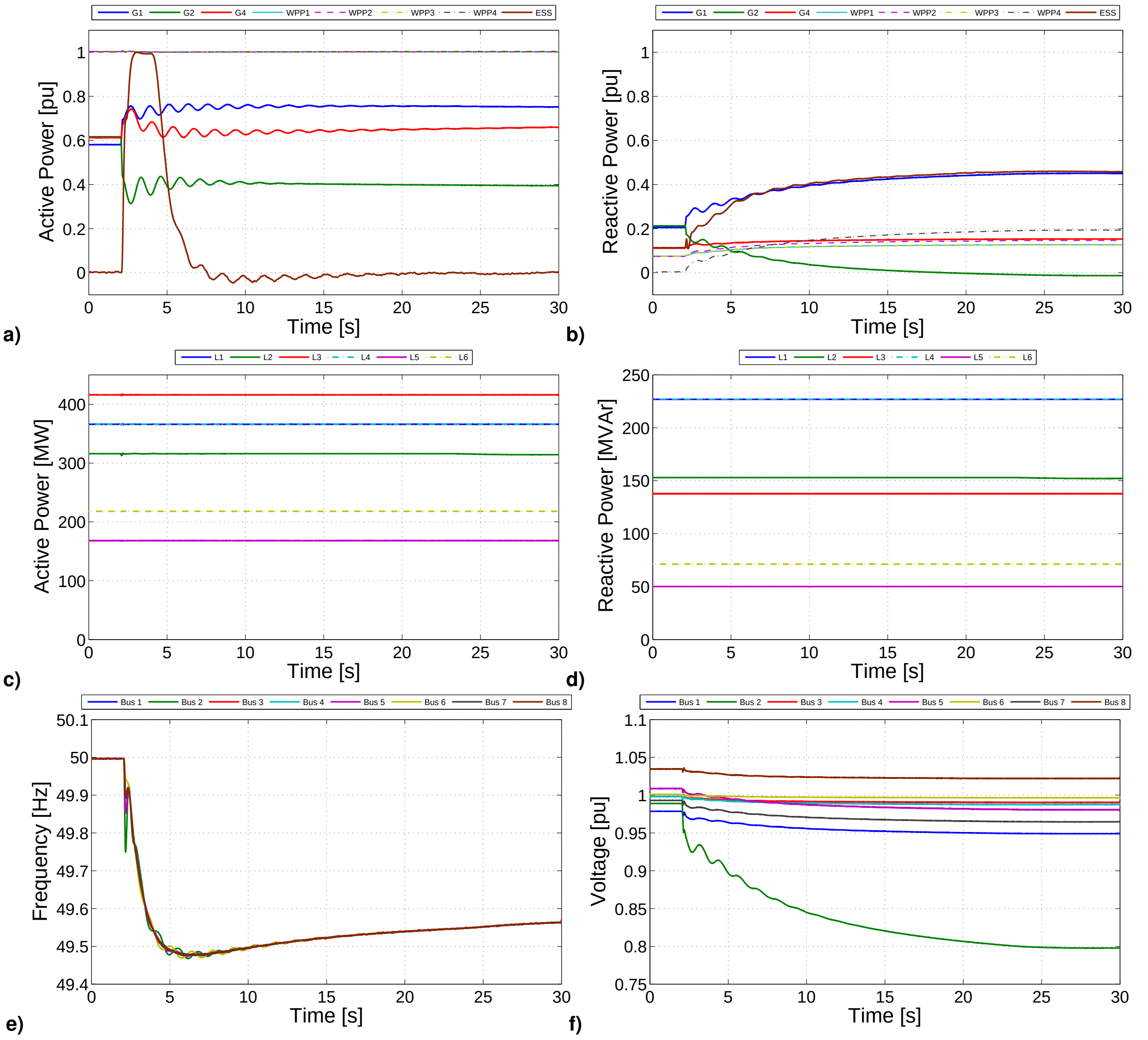

Figure C.9: a) active power from generation units, b) reactive power from generation units, c) active power consumption of loads, d) reactive power consumption of loads, e) frequency at buses, f) voltage at buses.

Table C.31: ESS parameters.

Nominal power [MW]	T_{ESS} [-]	K_{ESS} [-]	Control ratio [-]
15	0.5	7	1

C.3.2 SC2_6C

Table C.32: Generation settings.

Generation units	Power rating [MVA]	Active power* [MW]	Reactive power* [MVAr]	Inertia constant* [MWs/MVA]
G1	750	438	125	10.01
G2	640	394	-40	8.32
G3	-	-	-	-
G4	374	232	40	6.67
WPP1	220	200	14	0
WPP2	220	200	13	0
WPP3	220	200	14	0
WPP4	220	200	-6	0
Total**	2644	1864	160	5.80

*initial steady state value
**excluding the ESS

Table C.33: Load, inductors and capacitors settings.

Load	Active power [MW]	Reactive power [MVAr]	Power factor [-]	Note
L1	366	226.92	0.85	
L2	316	152.94	0.90	
L3	416	137.87	0.95	
L4	366	226.92	0.85	
L5	168	50.00	0.96	
L6	218	71.21	0.95	
L7	0	144	-	Shunt inductor
C4	0	200	-	Shunt capacitor
C5	0	40	-	Shunt capacitor
C6	-	200	-	Shunt capacitor

Table C.34: SC2_6C: results for all buses.

	f_{min} [Hz]	df/dt [Hz/s]	t_{min} [s]
Bus 1	49.4836	0.3115	6.3840
Bus 2	49.4809	0.1876	6.5680
Bus 3	49.4826	0.3043	6.6768
Bus 4	49.4824	0.3017	6.6760
Bus 5	49.4816	0.2698	6.6736
Bus 6	49.4815	0.3442	6.8616
Bus 7	49.4836	0.3098	6.3832
Bus 8	49.4828	0.3028	6.6768

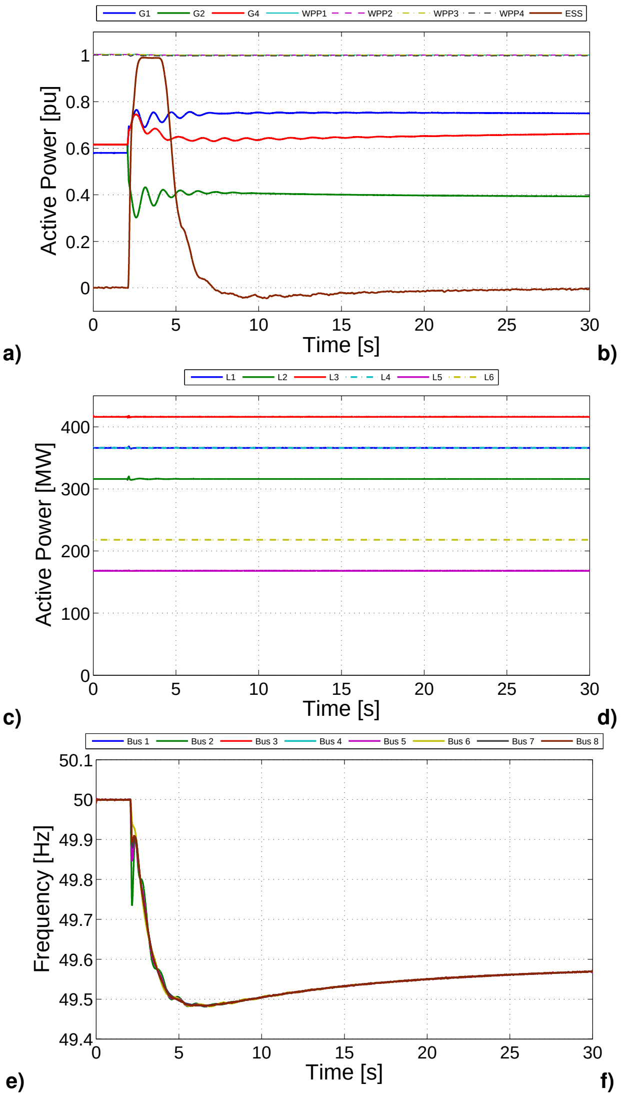

Figure C.10: a) active power from generation units, b) reactive power from generation units, c) active power consumption of loads, d) reactive power consumption of loads, e) frequency at buses, f) voltage at buses.

Table C.35: ESS parameters.

Nominal power [MW]	T_{ESS} [-]	K_{ESS} [-]	Control ratio [-]
15	0.5	7	1

C.4 Study case 3 - results

C.4.1 SC3_4

Table C.36: Generation settings.

Generation units	Power rating [MVA]	Active power* [MW]	Reactive power* [MVAr]	Inertia constant* [MWs/MVA]
G1	750	437	154	10.01
G2	640	395	134	8.32
G3	-	-	-	-
G4	374	231	42	6.67
WPP1	220	200	15	0
WPP2	220	200	15	0
WPP3	220	200	15	0
WPP4	220	200	1	0
Total**	2644	1863	376	5.80

*initial steady state value
**excluding the ESS

Table C.37: Load, inductors and capacitors settings.

Load	Active power [MW]	Reactive power [MVAr]	Power factor [-]	Note
L1	366	226.92	0.85	
L2	316	152.94	0.90	
L3	416	137.87	0.95	
L4	366	226.92	0.85	
L5	168	50.00	0.96	
L6	218	71.21	0.95	
L7	0	144	-	Shunt inductor
C4	0	200	-	Shunt capacitor
C5	0	40	-	Shunt capacitor
C6	-	-	-	Shunt capacitor

Table C.38: SC3_4: results for all buses.

	f_{min} [Hz]	df/dt [Hz/s]	t_{min} [s]
Bus 1	49.4949	0.3309	5.3528
Bus 2	49.4827	0.2604	4.9016
Bus 3	49.4952	0.3252	5.7288
Bus 4	49.4946	0.3239	5.8312
Bus 5	49.4926	0.3054	4.8960
Bus 6	49.4869	0.3462	5.6768
Bus 7	49.4952	0.3295	5.3528
Bus 8	49.4955	0.3230	5.7272

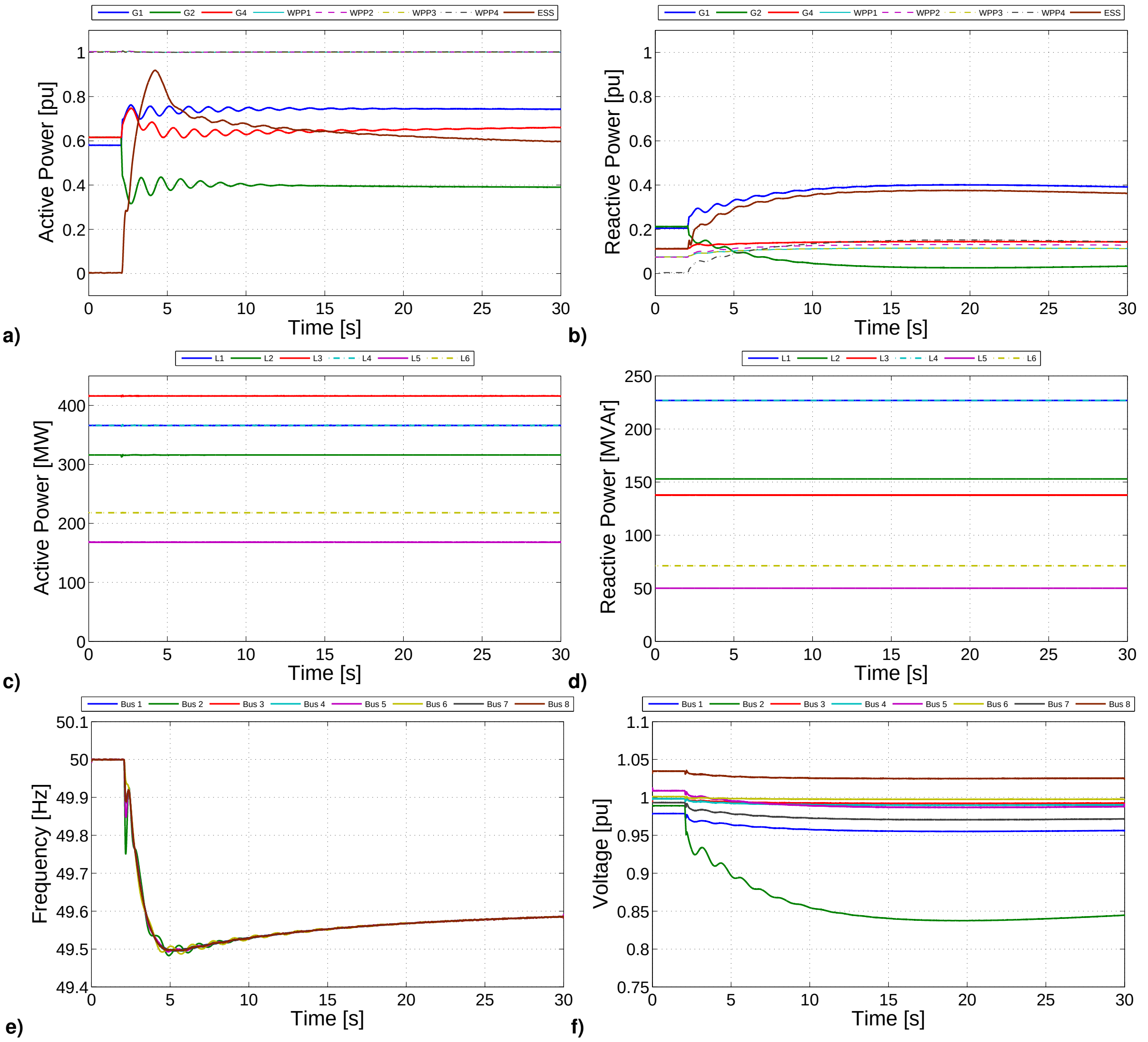

Figure C.11: a) active power from generation units, b) reactive power from generation units, c) active power consumption of loads, d) reactive power consumption of loads, e) frequency at buses, f) voltage at buses.

Table C.39: ESS parameters.

Nominal power [MW]	T_{ESS} [-]	K_{ESS} [-]	Control ratio [-]
15	0.5	7	0.25

C.4.2 SC3_4C

Table C.40: Generation settings.

Generation units	Power rating [MVA]	Active power* [MW]	Reactive power* [MVAr]	Inertia constant* [MWs/MVA]
G1	750	437	125	10.01
G2	640	394	-39	8.32
G3	-	-	-	-
G4	374	231	39	6.67
WPP1	220	200	14	0
WPP2	220	200	14	0
WPP3	220	200	13	0
WPP4	220	200	-6	0
Total**	2644	1862	160	5.80

*initial steady state value
**excluding the ESS

Table C.41: Load, inductors and capacitors settings.

Load	Active power [MW]	Reactive power [MVAr]	Power factor [-]	Note
L1	366	226.92	0.85	
L2	316	152.94	0.90	
L3	416	137.87	0.95	
L4	366	226.92	0.85	
L5	168	50.00	0.96	
L6	218	71.21	0.95	
L7	0	144	-	Shunt inductor
C4	0	200	-	Shunt capacitor
C5	0	40	-	Shunt capacitor
C6	-	200	-	Shunt capacitor

Table C.42: SC3_4C: results for all buses.

	f_{min} [Hz]	df/dt [Hz/s]	t_{min} [s]
Bus 1	49.4982	0.3215	5.1968
Bus 2	49.4927	0.1913	5.4800
Bus 3	49.4950	0.3108	5.4744
Bus 4	49.4945	0.3090	5.4744
Bus 5	49.4937	0.2775	5.4760
Bus 6	49.4939	0.3568	5.4768
Bus 7	49.4980	0.3192	5.4760
Bus 8	49.4954	0.3092	5.4744

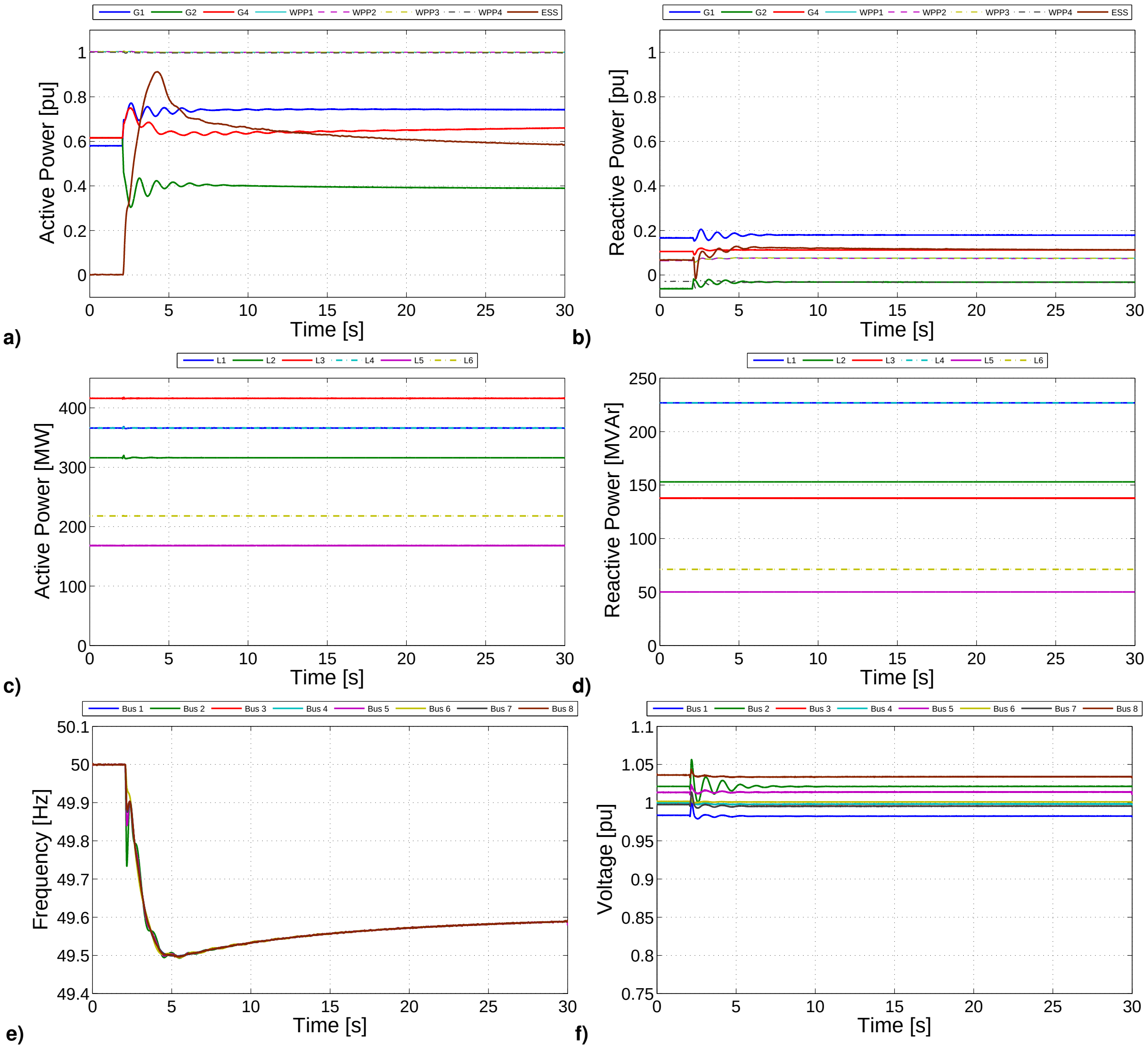

Figure C.12: a) active power from generation units, b) reactive power from generation units, c) active power consumption of loads, d) reactive power consumption of loads, e) frequency at buses, f) voltage at buses.

Table C.43: ESS parameters.

Nominal power [MW]	T_{ESS} [-]	K_{ESS} [-]	Control ratio [-]
15	0.5	7	0.25